Fakultät für Physik
der
Technischen Universität München
Walter Schottky Institut

Towards Carbon Nanotube-based

Molecular Electronics

Po-Wen Chiu

Contents

Symbols

$a = \sqrt{3}a_{c-c}$	lattice constant of carbon nanotubes.
a_{c-c}	nearest neighbor C$-$C distance.
$\mathbf{C}$	chiral vector of carbon nanotubes.
C_t	nanotube capacitance.
d_t	nanotube diameter.
D	diffusion constant.
$\Delta\Phi$	Schottky barrier lowering.
E_C	conduction band edge.
E_F	Fermi energy.
E_g	energy gap.
E_V	valence band edge.
ϵ_0	dielectric constant of vacuum.
ϵ_r	average dielectric constant of device.
f	doping fraction.
g	energy gain.
g_m	transconductance.
γ	strain along tube circumferential direction.
γ_0	energy overlap integral.
$\hbar$	reduced Planck's constant.
$\mathbf{k}$	electronic wave vector.
$\mathbf{k}_F$	Fermi wave vector.
k_s	spring constant of cantilever.
$\mathbf{k}_v$	vertices of hexagonal Brillouin zone of graphite.
l_m	mean free path.
l_ϕ	phase coherence length.
n_e	electron density.
Q	quality factor of cantilever.
σ	electrical conductivity.
σ_t	elastic strain along tube axis.
θ	chiral angle of carbon nanotubes.
θ_p	pyramidalization angle.
ϕ_π	π-orbital misalignment angle.
Φ_b	Schottky barrier.

Φ_{b0}	zero-bias Schottky barrier.
μ_h	hole mobility.
ν	Poisson's ratio.
ν_s	single-particle states per unit volume.
τ	relaxation time.
$\mathbf{T}$	translational vector of carbon nanotubes.
$\overline{v}$	average velocity of electron.
v_F	Fermi velocity.
V_a	output voltage from voltage adder.
V_{cg}	carbon-gate voltage.
V_{ds}	drain-source voltage.
V_{bg}	back-gate voltage.

Outline

In 1956 the Nobel Prize was awarded to Shockley, Bardeen and Brattain for their discovery of the transistor effect in 1947. The transistor is one of the most important inventions of the past century and often cited as the example of how scientific research can lead to useful commercial products. The integration of transistors in modern semiconductor electronics led to another revolution in human history. The Nobel Prize was again awarded to this great contribution in 2000. Half a century after the first transistor, the point-contact transistor, scientists have demonstrated that semiconducting carbon nanotubes can also have transistor-like behavior. The transistor size has been shrunk by a factor of 10^6. This thesis outlines the process of making nanotube-based electronic devices, as well as the study of their electrical transport. Particular emphasis is placed on electrical transport and modification of electronic structure promoted via structural changes to the tube.

In chapter 1 we will present an introductory overview to carbon nanotubes and their band structures. Several review papers [4, 106] are recommended for detailed description in the electronic structure and consequent transport properties of carbon nanotubes. Chapter 2 will discuss the experimental methods involved in device preparation and electrical studies. It is a challenge to exploit the transport properties of specific molecules by applying selective metal contacts to them. This chapter, therefore, includes how we separate the tangled carbon nanotubes isolating them in suspension and then selectively making contact on desired nanotubes. The measurement setup for electrical transport is shown at the end of this chapter.

Chapter 3 gives a brief description of the electrical transport in mesoscopic conductors. At appropriate temperatures the charge quantization can be observed via single electron tunneling in junction/island/junction arrangement, which is used for interpreting the transport behavior of carbon nanotubes at low temperatures.

Chapter 4 discusses very interesting hierarchal nanotube peapod structures, i.e., metallofullerenes are peas and confined in the interior hollow of nanotubes. The encapsulation of metallofullerenes is inspected by means of a high resolution transmission electron microscope. We will discuss the role of metallofullerenes inside a nanotube and how this varies the electrical properties of the host nanotube as a function of temperature.

In conventional metal-oxide-semiconductor field-effect transistors (FETs), a top gate is often used to control the conduction of the inversion layer underneath the gate insulator. The carbon nanotube FETs in the published literature to date are constructed either in back gate or in top gate configurations. This allows the carbon nanotube FETs to be operated in macroscopic scale. In chapter 5, we will show a novel method of making carbon nanotube FETs operated in *real nanoscale*. The conventional metal gate is replaced by an in-plane carbon gate which is actually made by another carbon nanotube and insulated by the single molecular linker to an active channel. To form these T-shape junctions, chemical functionalization has been done to incorporate diaminal functionality into carbon nanotubes. The presence of a molecular linker is evidenced by X-ray photoelectron spectroscopy and Raman spectroscopy. How a one-dimensional carbon nanotube gate works in modulating another one-dimensional carbon nanotube active channel will be discussed in chapter 6.

Chapter 1

Introduction

1.1   Carbon family and nanotubes

Prior to the discovery of fullerenes, graphite and diamond were the only known crystalline forms of carbon. The diamond is sp^3-hybridized, forming a three-dimensional (3D) network by binding the tetrahedral unit structures together, whereas the sp^2 hybridization in graphite links carbon atoms in a two-dimensional (2D) layer of hexagons (Figure 1.1 (a) and (b)). In the latter case, the p_z orbitals which are perpendicular to the plane of graphene build a delocalized π-electronic system and allow the fourth valence electron in carbon atoms to move freely on the plane. On the other hand, all valence electrons in diamond are localized around the carbon atoms. These structural differences bring about profound affects in the electrical properties of graphite and diamond: graphite is a semimetal, and diamond is an insulator with a band gap of $\sim$6 eV.

In 1985 a new form of carbon, C_{60} fullerenes, was discovered by Kroto *et al.* [89]. The 0-dimensional (0D) molecules have a particular shape like a "soccer ball" (so-called "buckyball" as shown in Figure 1.1 (c)). These fullerenes are made up of 60 carbon atoms arranged in pentagonal and hexagonal rings. The discovery and subsequent synthesis in macroscopic quantities of fullerenes has initiated a new field in the chemistry and physics of carbon. The 0D structure of fullerenes shows many intriguing features and potential for practical applications including investigations into superconductivity, quantum dots, molecular electronics, and fundamental solid-state physics.

In 1991 Iijima discovered a cylindrical form of the "buckyball", known as a carbon nanotube [73] (Figure 1.1 (d)). Nanotubes fall into two broad classes: multiwall and single wall. The earliest observations by Iijima were of micrometer

long multiwall nanotubes found in characterizing fullerenes grown via the carbon arc method. An ideal single wall carbon nanotube (SWNT) is a hexagonal network of carbon atoms that has been rolled up to make a seamless hollow cylinder (Figure 1.2 (a) and (b)), while a multiwall carbon nanotube (MWNT) is a coaxial arrangement of numbers of SWNTs (Figure 1.2 (c) and (d)). Nanotubes belong to the family of fullerenes and can be thought of as elongated buckyballs. Both sorts of tubes have sp^2-hybridized structure, like graphite, and in the ideal case are terminated at the ends by perfectly fitting fullerene caps.

(a)   (c)   (d)

diamond C_{60} fullerene

(b)

graphite   (10, 10) nanotube
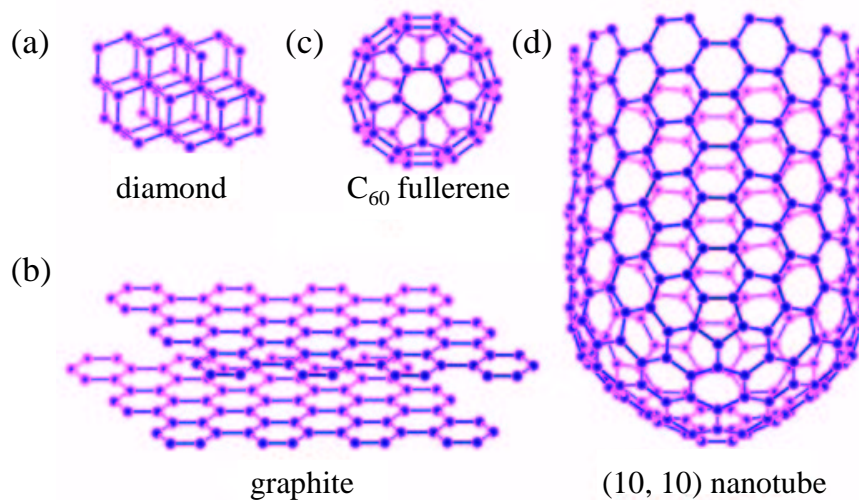
Figure 1.1: Three different forms of carbon materials: (a) diamond structure of carbon; (b) graphite structure of carbon; (c) C_{60} fullerene; (d) tubular structure of carbon, which is regarded as an elongated fullerene.

Carbon nanotubes can be synthesized by various methods, including arc-discharge, laser ablation and chemical vapor deposition [42]. In the arc-discharge method, carbon atoms are evaporated by a plasma of helium gas ignited by high currents passing through opposing carbon anode and cathode. The carbon atoms nucleate on a metal catalyst and grow up to several micrometers in length. A similar principle is adopted in the laser ablation method where intense laser pulses are used to ablate a carbon target containing metal catalysts. During laser ablation, a flow of inert gas is passed through the growth chamber to carry the grown
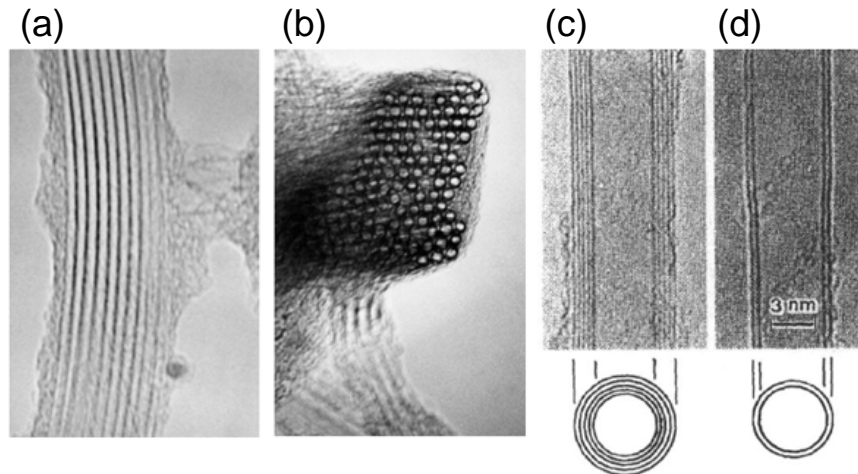
Figure 1.2: High resolution transmission electron microscope (HRTEM) micrographs of carbon nanotubes. (a) A thin bundle of single wall carbon nanotubes. The parallel lines are the walls of individual tubes. The outermost boundary of the nanotube bundle is covered by amorphous carbon. (b) Cross sectional view of a nanotube bundle. (c) $\sim$ (d) Multiwall nanotubes with five and two shells, respectively. Below the images the cross sectional structure of the two tubes is shown. [73, 74]

nanotube downstream to a cold collection finger. The produced SWNTs mostly crystallize in the form of ropes having tens of individual nanotubes close-packed into hexagons via van der Waals interactions. In chemical vapor deposition, a flowing hydrocarbon gas is decomposed by metal catalysts. The precipitation of carbon from the saturated phase in metal particles leads to the formation of a tubular carbon solid.

Since the discovery and high-yield synthesis of carbon nanotubes, they have attracted great interest among the research community due to their remarkable mechanical and electronic properties. This stems not only from the fact that carbon nanotubes are heir to the unique features of graphite, but also from their one-dimensional (1D) aspect. For instance, the Young's modulus Y in carbon nanotubes can be as high as $\sim$1 TPa. This makes the nanotube an excellent candidate for strengthening the matrix in composite materials. On the other hand, carbon nanotubes are ideal examples of molecular wires for studying elec-
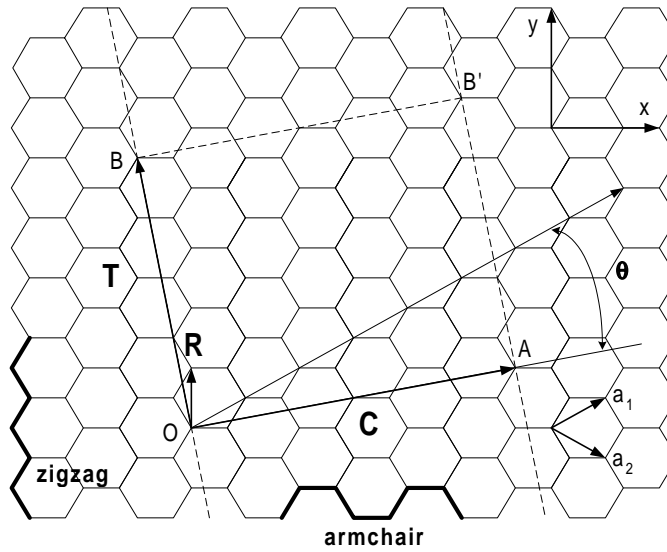
Figure 1.3: Hexagonal network of a graphite sheet. The tube with index $(n, m) = (4, 2)$ is constructed when the dotted strip is rolled up in such a way that point O matches point A, and point B matches point B'. θ describes the chiral angle of a specific tube and varies between $0 \leq \theta \leq \pi/6$. **C** is the chiral vector and perpendicular to the translational vector **T** which defines the Brillouin zone boundary of nanotubes by $k = \pm\pi/T$.

trical transport through a single molecule. They are excellent too as the building blocks in nanoelectronic devices, something which shows their superiority to conventional silicon-based microelectronics [6, 7].

1.2   Electrical properties of nanotubes

1.2.1   Geometrical structure

As described above, carbon nanotubes can be considered as seamless cylindrical forms of graphene sheets rolled up into a specific orientation. To understand the electronic properties of nanotubes, we begin with the geometrical structure of graphene, which decisively determines the band structure of the nanotubes [153]. Figure 1.3 depicts a hexagonal lattice of a graphite layer that can be cut out along the dashed lines and rolled up along a vector **C** to construct a tube. This **C** vector is called a chiral vector and expressed as $n\mathbf{a}_1 + m\mathbf{a}_2$, where $\mathbf{a}_1$ and $\mathbf{a}_2$

are the unit vectors of the hexagonal lattice. In general, an infinite number of nanotube geometries can exist. They are characterized by (n, m) with a defined chiral angle θ and diameter d_t:

$$\theta = \tan^{-1}[\sqrt{3}m/(m + 2n)] \tag{1.1}$$

$$d_t = \mathbf{C}/\pi = \sqrt{3}a_{c-c}(m^2 + mn + n^2)^{1/2}/\pi \tag{1.2}$$

where a_{c-c} is the nearest neighbor C−C distance (1.42 Å in graphite). Vector $\mathbf{T}$ is perpendicular to $\mathbf{C}$ and parallel to the nanotube axis. By choosing a starting and a final point with translational symmetry on the honeycomb lattice, a specific set of vectors $\mathbf{C}$ and $\mathbf{T}$ is determined. The lattice edges cut by the two sets of parallel dashed lines shown in Figure 1.3 can be perfectly mapped onto each other when forming the tube.

There are two special symmetry directions which are "non-chiral". They are termed "armchair" and "zigzag", having indices (n, n) and $(n, 0)$, respectively. The names armchair and zigzag refer to the pattern of carbon bonds along the circumference, which are shown bold in Figure 1.3. These two configurations differ by an angle of 30 degrees. The angles in between belong to the "chiral" tubes, and they have axial chiral symmetry, as can be seen in the lowest panel in Figure 1.4.

1.2.2 Energy dispersion and density of states

To determine the band structure of nanotubes, it is convenient to start by calculating the band structure of a graphite sheet by the tight-binding approximation [114, 131] and then to superimpose the periodic boundary conditions of nanotubes along the circumferential direction. Figure 1.5 (a) shows the hexagonal lattice of a graphite sheet in real space, with lattice vectors $\mathbf{a}_1 = (\sqrt{3}a/2, a/2)$ and $\mathbf{a}_2 = (\sqrt{3}a/2, -a/2)$. The grey area defines the unit cell which consists of two carbon atoms. Figure 1.5 (b) shows the reciprocal space and the corresponding reciprocal lattice vectors $\mathbf{b}_1 = (2\pi/\sqrt{3}a, 2\pi/a)$ and $\mathbf{b}_2 = (2\pi/\sqrt{3}a, -2\pi/a)$. The first Brillouin zone is indicted by a grey hexagon.

Carbon atoms have four valence electrons, three of which are used to form sp^2 bonds with neighboring atoms in σ orbitals. They lie far below the Fermi level and do not contribute to the electrical conduction. The transport properties are determined by the fourth electron which occupies a π orbital resulting from a $2p_z$
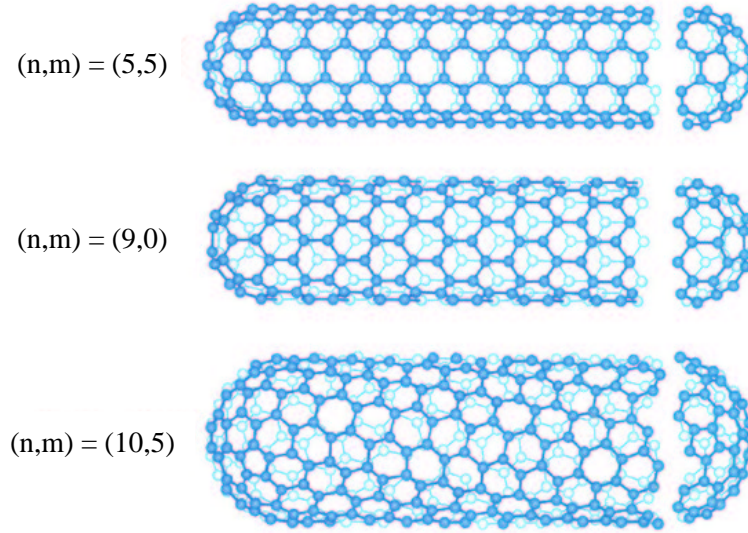
Figure 1.4: Three examples of nanotubes. From top to bottom: armchair (5,5), zigzag (9,0) and chiral (10,5) [74].
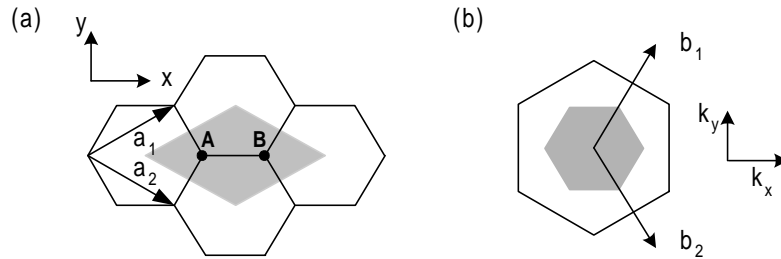
Figure 1.5: (a) The unit cell in real space and (b) the Brillouin zone of two-dimensional graphene are shown as the shaded rhombus and hexagon, respectively. a_i, and b_i, $(i = 1, 2)$ are the basis vectors and reciprocal lattice vectors, respectively.

bond. In a tight binding approximation, the energy dispersion for the π electrons in a graphite sheet is obtained [131]:

$$E(k_x, k_y) = \pm\gamma_0[1 + 4\cos(\frac{\sqrt{3}k_x a}{2})\cos(\frac{k_y a}{2}) + 4\cos^2(\frac{k_y a}{2})]^{1/2} \qquad (1.3)$$

where γ_0 is the energy overlap integral between nearest neighbors. This equation yields two bands resulting from bonding and anti-bonding states between the

two atoms in the unit cell. Figure 1.6 shows a three-dimensional plot of the energy dispersion $E(k_x, k_y)$. The conduction and valence bands touch and are degenerate at six **K** points; these six points define the vertices of the first Brillouin zone, as shown in Figure 1.7. In the simplest scheme, the antibonding band is symmetric. We note that there are two inequivalent Fermi points, **K** and **K'**, where the conduction and valence bands meet. At 0 K, the lower bonding bands are completely filled and the upper bands are empty, so graphite is classified as a zero-gap semiconductor.
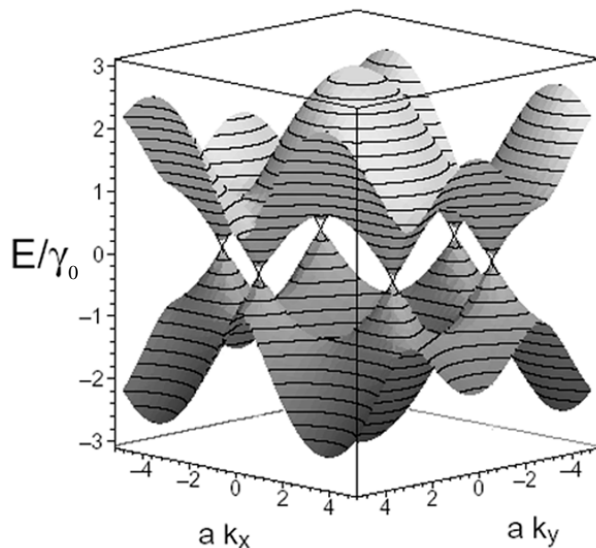
Figure 1.6: Graphene band structure. The π and π^* bands touch at the **K** points. Because there are two electrons in the unit cell, the π band is completely filled and π^* band is empty.

We can now obtain the band structure of nanotubes by imposing the periodic boundary condition along the circumferential direction. The energy is thus quantized: $\mathbf{k} \cdot \mathbf{C} = 2\pi q$ (q = 0, 1, 2...). The electrons are only free to move in an axial direction. This quantization along the circumferential direction gives rise to discrete numbers of parallel equidistant lines, representing the allowed **k** modes in the reciprocal space of the graphene. Each line corresponds to a 1D channel for conduction along the nanotube. The distance between adjacent lines, $2/d_t$, is inversely proportional to the nanotube diameter d_t, and the orientation of the lines are given by the chiral angle θ. Figure 1.7 shows the energy contours for the bonding band in the first Brilloiun zone. The quantization condition for
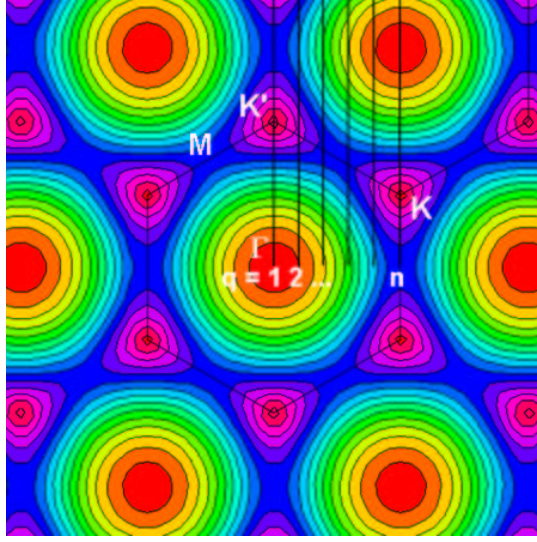
Figure 1.7: Energy contour plots of graphene for bonding band and the hexagonal Brillouin zone defined by the six **K** points. The Fermi level is at the vertices of the hexagonal Brillouin zone. The period boundary conditions along the circumference lead to the allowed **k** values indicated by the parallel lines from q = 0 to q = n.

armchair nanotubes is $\sqrt{3}nak_x = 2\pi$q (q = 0, 1, 2..., n), whereas $nak_y = 2\pi$q (q = 0, 1, 2..., n) applies for zigzag nanotubes. The parallel lines shown in Figure 1.7 are examples of allowed **k** modes in armchair nanotubes. The Fermi energy at the vertices of the Brillouin zone is sitting exactly on the allowed **k** modes, giving the metallic nature for armchair nanotubes. The dispersion relations for armchair and zigzag nanotubes can be obtained by inserting these quantization conditions in Equation (1.3) to yield:

$$E_{armchair}(k_y) = \pm\gamma_0[1 + 4\cos(\frac{\pi q}{n})\cos(\frac{k_y a}{2}) + 4\cos^2(\frac{k_y a}{2})]^{1/2} \qquad (1.4)$$

$$E_{zigzag}(k_x) = \pm\gamma_0[1 + 4\cos(\frac{\sqrt{3}k_x a}{2})\cos(\frac{\pi q}{n}) + 4\cos^2(\frac{\pi q}{n})]^{1/2} \qquad (1.5)$$

where $a = \sqrt{3}a_{c-c}$ is the lattice constant. Figure 1.8 shows two normalized dispersion diagrams plotted as E/γ_o vs **k** and the density of states corresponding to metallic and semiconducting nanotubes, respectively. For armchair nanotubes, there are two subbands which cross the Fermi energy at $E_F = 0$ since the 2D graphite energy bands cross at the **K** point of the 2D Brillouin zone. The density

of states is zero at the **K** point in the 2D case, but there is non-vanishing density of states at the **K** point in the 1D case. Away from the Fermi level, the onset of the next subbands leads to van Hove singularities. These unique spikes in the 1D density of states can also be understood from Figure 1.7. The van Hove singularities appear at points $\mathbf{k}_i$ in the 2D Brillouin zone where the allowed **k** lines are tangential to the equienergy contours. In semiconducting nanotubes, there are no allowed **k** lines passing through the **K** or **K'** points. The allowed **k** line closest to **K** contributes to the first band edge which forms the van Hove singularities in the density of states. In this case, there is an energy gap E_g defined by the separation of van Hove singularities. This energy gap is inversely proportional to the nanotube diameter and expressed as $E_g = 2a\gamma_0/\sqrt{3}d_t$. The right-hand panel in Figure 1.8 (a) and (b) shows the density of states derived from the corresponding energy dispersion relationship shown in the left panel. The spatial resolved atomic structure of carbon nanotubes and the corresponding electronic density of states are already confirmed by the investigations of scanning tunneling microscope [113, 116, 155].
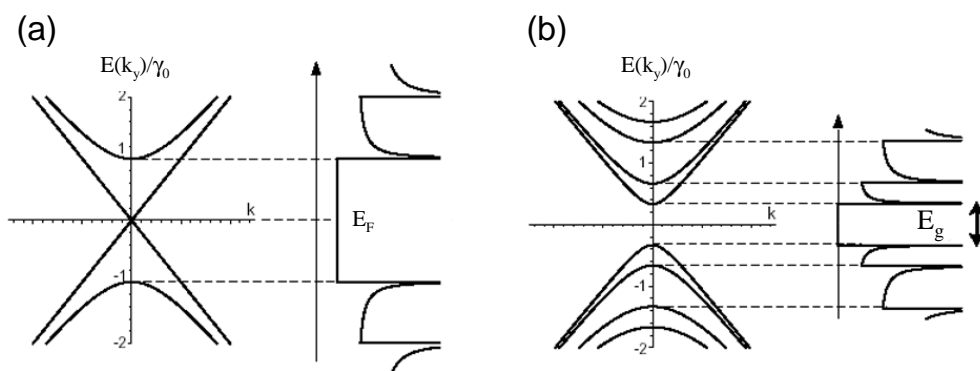
Figure 1.8: Approximate one-dimensional energy dispersion relations and corresponding density of states for (a) metallic carbon nanotubes and (b) semiconducting carbon nanotubes, respectively. The number of subbands depends on the **C** vector. The energy at the Fermi level is zero.

1.3   Nanoscale science and molecular electronics

Nanoscale science is concerned with the investigation of matter on the nanometer regime, which is generally taken as the 1 to 100 nm range. The explosion in both academic and industrial interest in these nanoscale materials over the past decade has arisen because of the remarkable variations in fundamental solid-state properties. Carbon nanotubes which have been demonstrated to show many intriguing electrical, optical and mechanical properties provide just one example of these materials. Carbon nanotubes are not only interesting from the prospective of fundamental scientific research due to their one-dimensional nature, they are also attractive for industry. Many potential applications have been proposed: They can be used e.g. as electronic devices and field emission sources [7, 65]; as chemical or biological sensors [157]; as sharp and well-defined atomic force microscope (AFM)/scanning tunneling microscope (STM) tips [36, 90]; as fillers in conductive and high-strength composites [94]; as a balance for weighing small particles in the fg regime [118]. Most of these uses are based on their unique electronic properties and geometrical structure.

Figure 1.9 (a) shows a field emission display made from SWNTs as electron emitting source [16]. Figure 1.9 (b) demonstrates a nanotube tip used in scanning probe microscopy, which is capable of imaging molecular structures [14, 60, 90]. The nanotube is grown by chemical vapor deposition directly on a standard Si cantilever. Other potential applications based on their mechanical properties are shown in Figure 1.10. A nanotube buckypaper is made of carbon nanotubes which form a tangled 2D network similar to the fiber structure in a normal paper. The nanotube buckypaper can stretch upon doping. The buckypaper elongates when charged with electrons, while it contracts upon hole injection. If we stick two buckypaper onto either side of double-stick tape and inject different sign of charges, the whole device can function as an actuator and moves back and forth by changing the sign of injected charges (Figure 1.10 (a)∼(b)). A similar actuating response is shown in Figure 1.10 (c)∼(e). Two individual multiwall nanotubes are attached to two separate electrodes. By applying different potential to the electrodes, the two tubes come closer or repulse each other by the electrostatic force, thus resembling mechanical tweezers. They can pick up submicron particles, as exemplified in Figure 1.10 (e).

Despite structural similarity to a graphite sheet, SWNTs can be either metallic or semiconducting, depending on the direction in which the graphite sheet is rolled
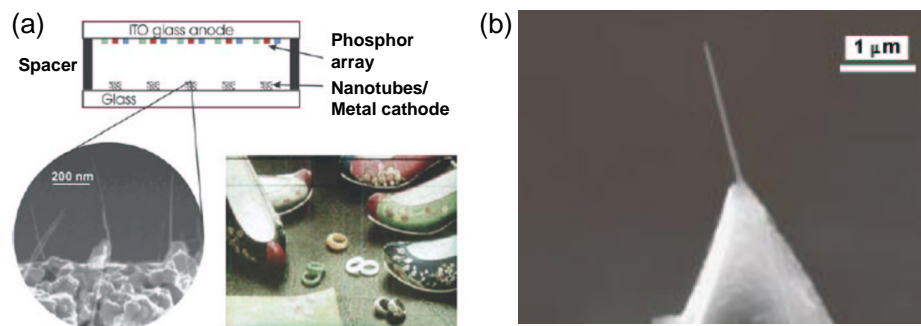
Figure 1.9: Application of SWNTs in (a) field emission display, and
(b) tips for scanning probe microscopy. Upper panel of (a) schemat-
ically illustrates the layout of a flat panel display based on carbon
nanotubes. ITO, indium tin oxide, is used as anode, whereas carbon
nanotubes are used as cathode. The carbon nanotubes are grown by
chemical vapor deposition and shown in the scanning electron mi-
croscope (SEM) image in lower left panel. Lower right panel of (a)
is a photograph of a 5-inch field emission display made of carbon
nanotubes ((a) is from [16]). (b) Field-mission SEM image of a
multiwall carbon nanotube growing on an AFM tip end by chemical
vapor deposition ((b) is from [90]).

to form a tubular cylinder. Typical nanotubes have diameters of $1 \sim 2$ nm and are
several micrometers long. The high aspect ratio makes them ideal for exploiting
their electrical properties. By contacting the two ends of the nanotube with metal
leads, electrical transport through an individual nanotube can be performed. A
semiconducting nanotube is found to act as a field-effect transistor (FET) [148]
which is one of the most important inventions of the past century and play a
crucial role in current electronic circuits.

The evolution of electronic devices from the earliest form of point-contact tran-
sistor in 1947 to the first commercial Integrated Circuits has taken less than 20
years [127]. However, these solid-state electronic devices have nowadays become
the virtual nerve cell of the Information Age. They are what we used in global
wireless telephone communication and what have put computers on our desktop.
With the advanced manufacturing technologies in the semiconductor industry,
the devices keep miniaturizing down to the submicronmeter regime to date, and
this is likely to reach its limit in the next $10-15$ years when the length shrinks
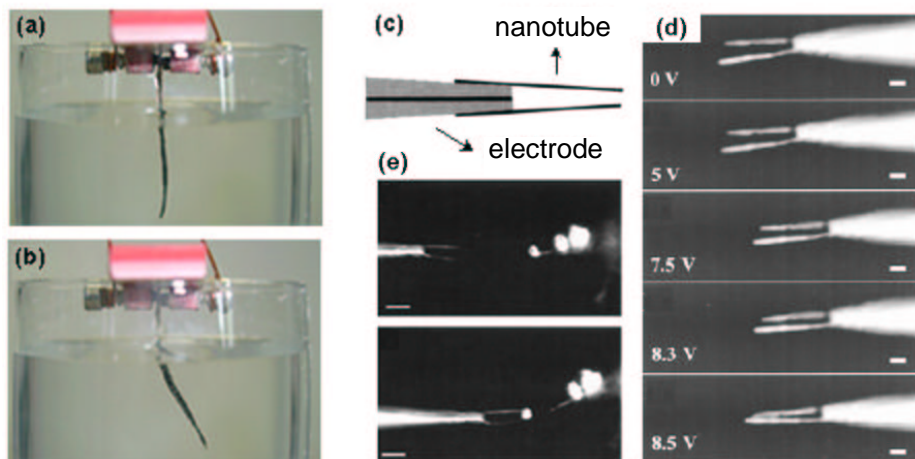
Figure 1.10: Application of CNTs in (a)−(b) artificial muscle (actuator, from our lab) and (c)−(e) nanotweezers. (a) Actuators are made up of two slices of carbon nanotube buckypapers each of which is stuck on a double-stick Scotch tape. The device is operated in aqueous NaCl. The actuator can be bent to the right or left by applying voltages to both sides of the Scotch tape, as shown in (b). (c) Schematic illustration of nanotweezers. Two multiwall nanotubes are mounted on separated electrodes. (d) The nanotweezers are operated by applying a voltage to the two electrodes for either attraction or repulsion. A small particle can be grabbed by the tweezers as shown in (e) [83].

below 100 nm. The main problem with further miniaturization is the onset of quantum phenomena, e.g., tunneling, that would make scaled-down conventional devices inoperable. At this nanoscale, new problems are created, but also new opportunities. Some new developments, such as tunneling field-effect transistors and single-electron transistors, are in fact based on quantum phenomena.

Besides inorganic silicon and gallium arsenide semiconductors, there has been a growing research effort in the field of organic molecule-based transistors [40] which are mainly conjugated polymers, oligomers or other molecules such as polyacetylene [25], pentacene [97] and C_{60} [59]. Recently, great progress has been made in devices fabricated by single molecules. Reed *et al.* [125] reported $I-V_{ds}$ characteristics of single benzene-1,4-dithiolate molecules. Alivisatos and co-workers [85] reported similar transport measurements in semiconduct-

ing and metallic clusters between gold electrodes. Improved carbon nanotube FETs by the IBM group or more complicated complementary logic circuits have been demonstrated recently [7]. Compared with the conventional metal-oxide-semiconductor FETs, the carbon nanotube FETs have shown even better performance in device operation, such as carrier mobility, transconductance and on/off ratio [75, 156]. This has opened up a new opportunity in the substitution of Si-based microelectronics.

In Table 1 we summarize the performance of various FETs in different materials. In the early development stage of organic thin-film transistors, the mobility of charge carriers is typically limited to below 10^{-3} cm^{2}V^{-1}s^{-1}. The weak intermolecular interaction forces in the organic active layer, most usually van der Waals force, may be responsible for this limit. At present, we can observe a remarkable increase of mobility in organic semiconductors, which has been achieved either by improving the processes used for the fabrication of the transistors or by synthesizing new organic materials. Compared with the Si, the mobility in these organic materials is still two orders of magnitude smaller, but comparable to the amorphous Si. This could therefore be competitive for existing or novel thin-film transistor applications requiring large-area coverage, structural flexibility, low-temperature processing and low cost. If we further compare the organic semiconductors with carbon nanotubes, we can see a very impressive improvement in the carrier mobility by three orders of magnitude. In addition, the active channel is shrunk to a 1D single molecule scale. In Si the charge carriers move as highly delocalized plane waves in wide bands and hence have a very high mobility. The mobility is only limited by scattering with impurities or lattice. In organic thin-film semiconductors the band transport breaks down and carrier transport takes place by hopping between localized states. In the case of carbon nanotubes, the charge carriers go ballistically up to micrometers in metallic nanotubes [8], whereas the transport in semiconducting nanotubes is diffusive-like possibly due to phonon excitation or interband scattering [3, 158]. This limits the charge transport through the carbon nanotube active channel mainly because of the contact properties. By enhancing the coupling between the nanotube and the electrodes [102], the carbon nanotube can have enhanced mobility and function as an ambipolar transistor, i.e., n-channel conduction at positive gate voltage and p-channel conduction at negative gate voltage in the same tube. This is the main reason why the device performance of carbon nanotubes could be exponentially improved within a few years from the first proposal for the carbon nanotube FETs

Table 1.1: Comparison of operation performance in various FET devices.

Year	Material	Structure	Mobility* (cm^{2}V^{-1}s^{-1})		I$_{on}$/I$_{off}$	Reference
			(electron)	(hole)		
1997	Si	bulk	1500	450	$10^3 \sim 10^5$	[104]
1997	GaAs	bulk	8500	400	10^8	[104]
1988	Polyacetylene	thin film		10^{-4}	10^5	[25]
1995	C$_{60}$	thin film		0.3	--	[59]
1996	Pentacene	thin film		0.04	10^2	[39]
1997	Pentacene	thin film		1.5	10^8	[97]
1998	Carbon nanotube	single molecule		20	10^6	[101]
2002	Carbon nanotube	single molecule	1000	3000	10^6	[75]

*The mobility depends on the doping state and the dielectrics used in the gate insulator.

by *Tans* [148].

It is known that the electrical properties of semiconductors can be controlled via impurity doping. Different junction structures or complicated logic circuits can be fabricated by varying the doping level in the different active regions. This also applies in the case of the 1D carbon nanotubes [9, 38, 76]. Interestingly, the electrical properties of carbon nanotubes can be simply varied by changing the uptake of adsorbed oxygen molecules on the exterior wall, which modifies the band bending at the contacts and the charge transport accordingly [38]. Many such similarly interesting 1D solid-state properties have been found and verified in carbon nanotubes. This seems to promise of useful commercial products in the field of molecular electronics. However, there are still many challenges in the route towards application in electronics. One major challenge in particular lies in assembling and integrating multiple active components into circuits. To reach this goal, formidable technical hurdles still have to be overcome. Additionally, the chirality selective growth of carbon nanotubes is also a crucial step on the way to realizing carbon nanotube-based molecular electronics.

Chapter 2

Experimental techniques

2.1 Introduction

Carbon nanotubes provide a remarkable model in the 1D system: one atom in thickness, $1 \sim 2$ nm in diameter and several microns in length. The ultrahigh strength in their structure and their extended length make possible their use in device processing. Nevertheless, the fabrication of nanotube devices still presents the main practical challenge in probing the electrical properties of such a tiny object.

In this chapter we will describe how we apply leads to individual nanotubes or nanotube bundles and carry out the electrical measurements. To do this, raw materials have first to be purified. To make this easier to follow, discussion of this chemical treatment is held over till chapter 4 and combined with the nanotube opening and insertion of metallofullerenes. With the purified carbon nanotubes it is important to separate the tangled nanotubes in the form of buckypaper after purification. We show the suspension of nanotubes in subsection 2.2.1, followed by nanotube deposition on Si substrate in subsection 2.2.2. The conventional electron-beam lithography technique has been employed for patterning electrode contacts. Two different contact methods, "tube-on-top" and "metal-on-top", are introduced. The experimental setup for low-temperature transport measurements is described in section 2.3. At the end of this chapter, we introduce the technique for probing the magnetic force in nanoscale objects by means of magnetic force microscopy. This technique is used to see the magnetic properties of nanotubes encapsulated with Dy@C$_{82}$ molecules.

2.2   Device fabrication

2.2.1   Nanotube suspension

SWNTs used in this thesis were made either by the arc-discharge method or by the laser-ablation method. The raw materials consist of very long, tangled strands and small amounts of Co and Ni nanoparticles which act as catalysts in the synthesis process. These strands are bundles of SWNTs. They consist of 2D hexagonally packed SWNTs of a nearly monodisperse diameter ~ 1 nm. To study the electrical properties of individual SWNTs or of small bundles, it is necessary to separate the tangled materials well and then contact these individual or small bundles of nanotubes to external wires. To do this, nanotubes were added to an aqueous solution containing 1 wt% sodium dodecyl sulfate (SDS; from Fluka) which is an excellent surfactant in this regard. The SDS surfactant molecules can be adsorbed around the exterior tube wall and form a shell called *micelle*. The SDS molecules in the micelle shell are in dynamic equilibrium with nanotubes in the aqueous phase. The negatively charged surfactant molecule has a hydrophobic tail which modifies the surface chemistry of the nanotube and enhances the suspension in the aqueous solution. By exposing the liquid to ultrasonic agitation (KLN Ultraschall Generator 281/101), the tangled nanotubes can be well separated into individual nanotubes or nanotube bundles with a spectrum of lengths ranging from ~ 1 μm to ~ 10 μm, and diameters in the 1 ~ 10 nm range. The suspension of nanotubes in the aqueous solution with SDS surfactant will remain stable for months and will not coalesce again. It should be noted that although the ultrasonic agitation can effectively isolate and suspend the tubes in SDS, it may also create some defects on the tube wall or even reduce them in length. The typical treatment of sonication in our experimental condition is thus limited to 90 watts for less than 2 minutes.

2.2.2   Surface modification on Si chip

Various attempts have been made to deposit the isolated nanotubes onto the Si substrate. One uncontrollable way is shown by simply using sedimentation or spin coating in which a small amount of nanotube suspension was dropped onto the spinning substrate. In this case, an organic solvent, such as dimethyl formamide (DMF) , is used for dispersing nanotubes. The advantage of this approach may be the cleaner nanotube surface which enhances the electrical cou-

pling with electrode leads discussed in following section. However, without the aid of the surfactant most of the individual tubes are not well separated and exist in the form of bundles. This inhibits the exploration of electrical transport through individual nanotubes. Though where transport in a nanotube bundle is concerned, a single tube within the bundle investigated often predominated. The probability of finding one all-semiconducting nanotube bundle for making transistors is much too low. Another more effective way is to use chemically modified Si substrate and adsorb well-isolated nanotubes from SDS suspension. Even a site-specific adsorption can be readily achieved by this approach [24].

Here we use heavily doped Si as substrate, which has 100 nm thermally grown SiO_2 on top. The SiO_2 surface contains native OH-groups which are modified by reacting with 3-aminopropyltriethoxysilane or N-[3-(trimethoxysilyl)propyl]-ethylenediamine (both are from Aldrich). The Si chips were dipped in a 10 mL aqueous solution containing 6 μL, one of the above-mentioned silane, for 2 minutes at room temperature. Subsequently, the Si chip was rinsed with pure water and blown dry by nitrogen gas. Through this silanization, the SiO_2 surface is terminated by long chain molecules with ammonium groups. The adsorption of nanotubes from the micellar dispersion can be easily achieved by Coulomb attractive force between the negatively charged SDS surfactant and the oppositely charged SiO_2 surface. A droplet of supernatant is placed on the silanized SiO_2 for 10 to 20 minutes, depending on the concentration of the nanotube suspension. Finally, the substrate was intensively rinsed with pure water which can easily remove the surfactant molecules. Figure 2.1 shows the representative AFM (Nanoscope IIIa, Digital Instruments) image of nanotube deposition on Si substrate in this approach.

It should be noted that this adsorption approach is rather important in making all-carbon transistors which will be discussed in chapter 5 and chapter 6. In this transistor configuration, a nanotube which acts as an in-plane gate is attached by a single molecular linker to an active nanotube. The chemically modified adsorption process provides a non-destructive method for transferring linked nanotubes from the suspension solution to the substrate. It also prevents the coupled nanotube junctions from being severely distorted.
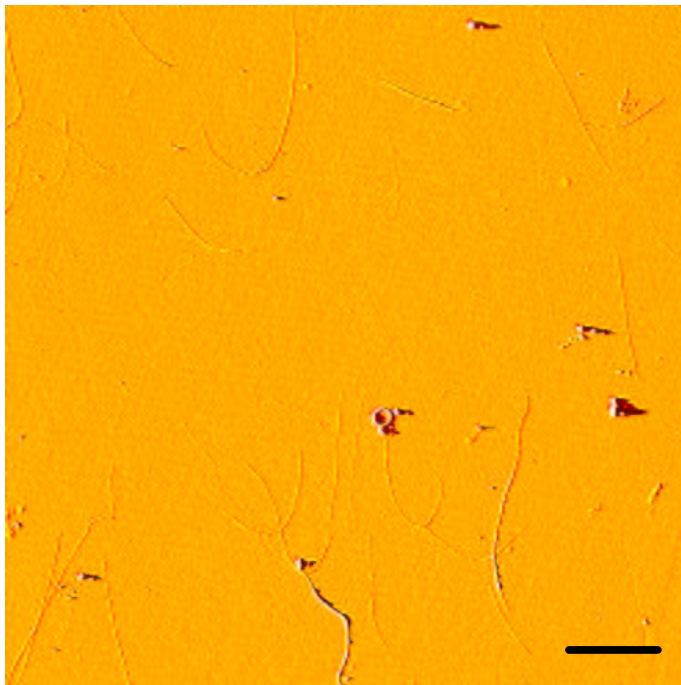
Figure 2.1: AFM image of dispersed nanotubes on silicon substrate taken in tapping mode. Due to the tip-sample convolution, the apparent tube width is much larger than the actual tube height. The visible nanotubes in this image scale are in the form of bundles. The scale bar is 2 μm.

2.2.3   Lithographical patterning

Electron-beam lithography is an extensively used technique in the field of mesoscopic physics, which has provided the finest nanostructuring method to date. It enables the reaching of tens of nanometers and offers a flexible and exact way to contact complicated nanostructures. The electron beam is generated in a SEM which was originally set up for imaging an object by scanning with a well-focused electron beam. Controlling the beam position and dwell time by a computer the designed pattern can be selectively exposed. The resolution is determined by the spot size of the electron beam, as well as by electron backscattering from the substrate. This backscattering acts as a secondary exposure that plays an important role for structuring elements lying close to each other.

In our lab a Hitachi S2300 SEM equipped with a motorized stage, a custom-made beam blanker, an external compensation of environmental magnetic fields

and *Elphy* software is used to write a pattern onto an organic electron resist layer, poly(methylmethacrylate) (PMMA), spun on a substrate. PMMA is a chain-scission resist operated on the basis of a radiation-induced reduction in the molecular weight of the comprising polymer. This reduced molecular weight results in a different solubility in the appropriate developing solution. The illuminated region is then selectively removed by chemical developer and the created structure serves as a mask for subsequent metal deposition. This processing is schematically shown in Figure 2.2.
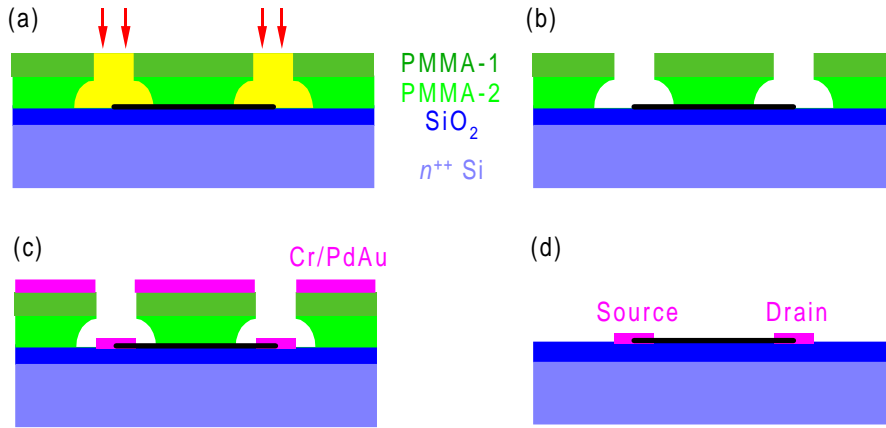
Figure 2.2: The steps for applying metal contacts to a nanotube by electron-beam lithography: (a) exposure (b) development (c) metallization (d) lift-off. The first layer (PMMA-1) is 3.5% 200 K and the second layer (PMMA-2) is 1.5% 950 K.

Here we use PMMA with different concentrations and molecular weights as resist, i.e., 3.5% 200 K for the first layer and 1.5% 950 K for the second layer. The first layer PMMA has higher sensitivity to the electron beam and creates a wider undercut in the writing area, which facilitates the diffusion of chemical developer into the undercut for complete lift-off. To remove the decomposed molecular chain by electron beam we use Isobutylmethylketone as chemical developer. The 1-methyl-2-pyrrolidon is chosen as standard remover in the lift-off process.

Figure 2.3 shows the SEM images of electrode structure made by the electron-beam lithography process discussed above. In Figure 2.3 (a), the 16 large electrode pads are used for wire bonding, connecting to the external circuit. In the central region shown in Figure 2.3 (b), several fine electrode arrays intended to
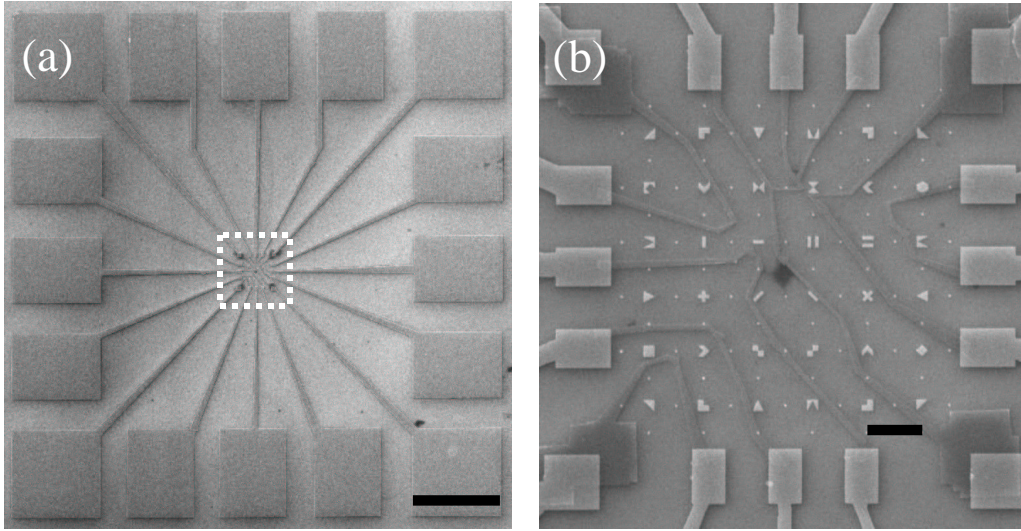
Figure 2.3: SEM images of electrode pattern for contacting nanotubes. (a) Large-scale view of pattern with 16 bonding pads. (scale bar: 200 μm) (b) Zoom-in of pattern in the central region. The scale bar is 10 μm and indicates the distance between two coordinate markers.

contact nanotubes are shown. Thin Ti or Cr layer (typically $1 \sim 2$ nm) are used to enhance the reliable contact and the adhesion between SiO_2 and the contact metal. In transport measurements, we did not find significant differences in contact resistance between using Ti or Cr as adhesion layer. In Figure 2.3 (b) there are four squares in the corners, which are used as alignment markers. Additionally, there are 6×6 coordinate markers spread within the central region.

For transport measurements two different device configurations have been made. Figure 2.4 shows the device layout in the tube-on-top arrangement. The Si substrate consists of three distinct layers: The bulk Si is 1 mm thick with 100 nm thermally grown SiO_2 on top and metallized by AlSiCu on the back side. The bulk Si is heavily doped by As to have resistivity $\rho < 5$ mΩ·cm and used as back gate. This doping level ensures that the back gate is still conductive till submili Kelvin regime. The parallel electrode arrays are predefined on top of the Si substrate. To enhance contact between the nanotube and electrodes AuPd alloy is used, in which the work function of Au (5.20 eV) is very close to that of Pd (5.17 eV) [126]. Following the above-mentioned adsorption procedure

appropriate density of nanotubes can be dispersed randomly on the substrate. As can be seen in the AFM image shown in Figure 2.4, a long nanotube bundle ($\sim 10~\mu$m) is crossing the predefined electrode arrays.
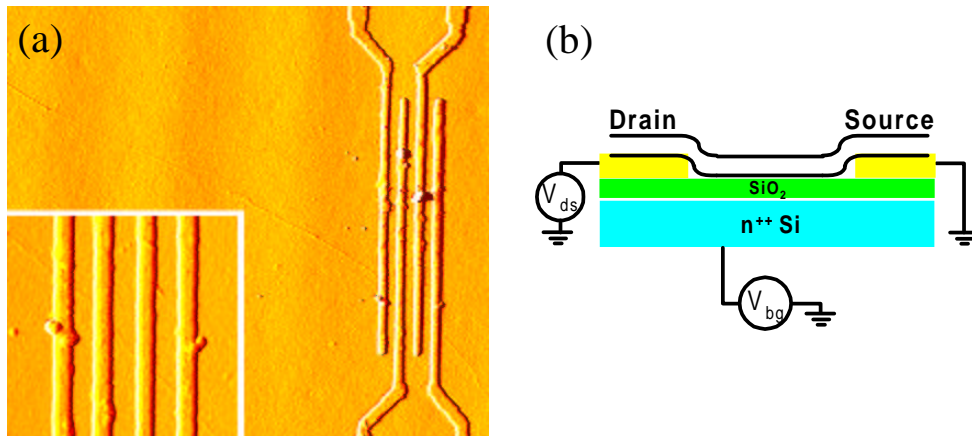
Figure 2.4: (a) AFM image of a 10 μm-long nanotube on top of four arrays of predefined electrodes. The electrodes are separated from each other by a 150 nm gap. The lower left panel shows the zoomed AFM image where the tube bridges the electrodes. (b) Schematic illustration of the three-terminal tube-on-metal geometry used in the transport studies.

An alternative contact method which is extensively used in our transport studies on nanotubes is shown in Figure 2.5. The nanotube is embedded in metal electrodes (also AuPd alloy) to enhance the electrical coupling between electrode and nanotube. To do this, predefined coordinate markers are needed to calculate the exact position of selected nanotubes relative to the neighboring coordinate markers. Additionally, four alignment markers at the corner of the writing field are also predefined for tracing back the origin of the coordinate system. The interconnection patterns between the nanotube and the outer bonding pads are designed with *Elphy* software. Following the standard electron-beam lithography process, the electrodes can be applied exactly on top of the selected nanotubes. The tolerance shift in our alignment technique is well controlled within around 50 nm. The main advantages of this contact method are to decrease the contact resistance and make possible contact patterns on complicated nanotube structures such as T-shaped intermolecular nanotube junctions (discussed in chapter 5 and

6).
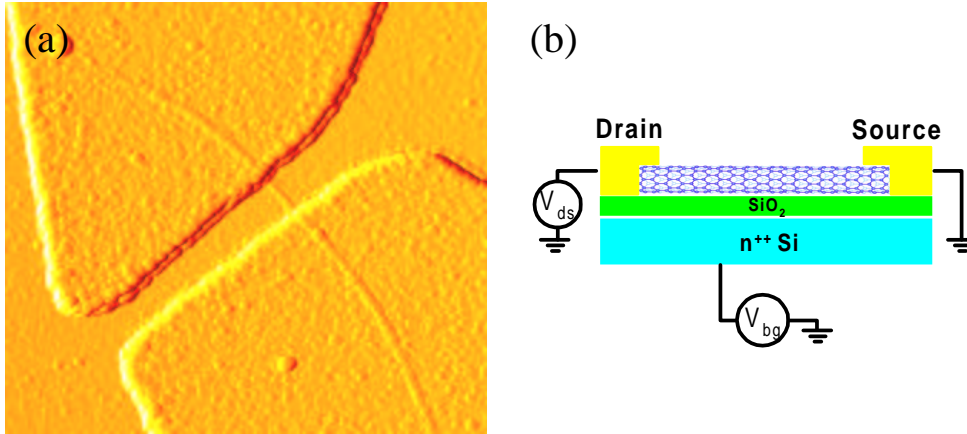
Figure 2.5: (a) AFM image of a nanotube embedded in drain and source electrodes. (b) Schematic illustration of the three-terminal metal-on-tube geometry used in the transport studies.

2.3 Electrical transport

We focus our electrical measurements mainly on the transistor configuration by means of standard three-terminal measurements: biasing one electrode (the drain) with a voltage V_{ds} and measuring the current passing through the device by connecting the second electrode (the source) to ground; modulating the electrostatic potential of the active channel by a third electrode (the back gate) which is 100 nm below the active channel of the device. In the case of all-carbon transistors, an additional gate which is made by another carbon nanotube is capacitively coupled to the nanotube conducting channel on the same plane. A schematic drawing is shown in Figure 2.6.

The main components of our setup are a desktop computer equipped with a GPIB data acquisition card (National Instrument) and controlled by Labview software, three voltage sources (two Keithley 2400 and one Keithley 230), a voltage adder (home-built) and a pre-amplifier (Ithaco 1211). The current is measured using the high sensitivity, low noise current pre-amplifier which outputs a voltage proportional to the current. The output voltage is amplified by a conversion factor μ (typically 10^{-7} A/V) and then read by a voltage meter (Keithley
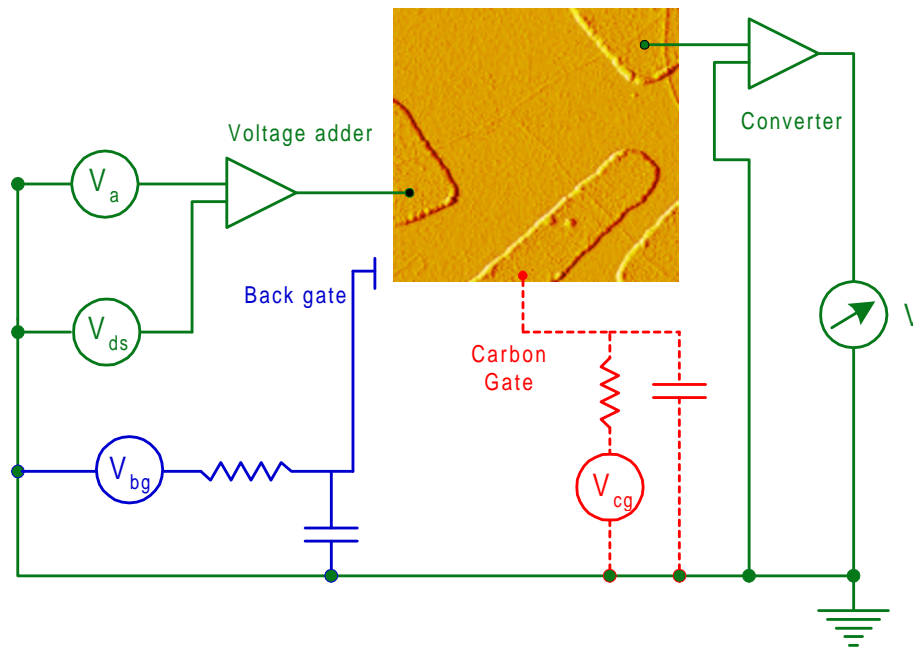
Figure 2.6: Schematic diagram of the setup used for electrical transport measurements. The device consists of four electrode contacts, two of which are used as drain and source, one of which is used as carbon in-plane gate. A common gate (back gate) is applied for whole device. The carbon gate is only used in all-carbon transistors, and for clarity the circuit of carbon gate is plotted by dashed lines. The gate voltage is applied through the low-pass filter formed by a resistor and a capacitor. The resistor serves to protect the device in the case of gate dielectric breakdown.

2000). A RC low-pass filter with a time constant around 0.5 sec is added between gate and voltage source to prevent abrupt potential changes and allow consecutive potential modulation on the nanotube. The voltage adder is designed to adjust the offset voltage from the pre-amplifier.

To enable low-temperature measurements of nanotube devices, one simple method has been employed. The sample is mounted into a stick with a Si diode as temperature sensor close to the back side of the sample. A small amount of ^{4}He gas is filled in the closed stick volume for heat exchange. To reach low temperature the stick is dipped into the ^{4}He dewar. By raising the sample above the liquid level, the sample can be brought to equilibrium at different temperatures. This allows measurements over a temperature range from 4.2 K to room temperature.

2.4 Scanning force microscopy

Scanning Probe Microscopy (SPM) is a powerful and intensively used tool for investigating objects in nanoscale science and technology. It has been successfully employed to explore mechanical properties [45, 134], electrical transport [8, 48], and even the atomic structures of individual SWNTs [64]. In this thesis, we use Atomic Force Microscopy (AFM) for structural characterization and Magnetic Force Microscopy (MFM) to investigate magnetic properties in magnetic metallofullerene doped SWNTs, since MFM is the only technique capable of mapping the magnetic stray field in nanoscale.

In a MFM, a magnetic tip is a standard silicon cantilever coated with ferromagnetic alloys and is used to probe the magnetic stray field above the sample surface. The image obtained by MFM presents the space distribution of some parameter characterizing magnetic probe-sample interaction, i.e., interaction force, amplitude of vibrating magnetic probe etc. When the tip scans over the sample, signals from the surface topography will dominate at close distances to the surface while, at greater distances from the surface (typically beyond 1000 Å), the magnetic signal will dominate. Consequently, depending on the distance between the surface and the tip, normal MFM images may contain a combination of topography and magnetic signals. In principle, there are two operation modes used for extracting the magnetic contrast in MFM.

1. Static Mode: This is usually operated in such a way that the magnetic force on the cantilever is kept constant. The Microscope can sense the deflection of the cantilever which will result in a force image. This method of imaging has the inherent problem of picking up the surface topography, and is only used for samples with large stray fields such as computer hard disk drives.

2. Resonant Mode: This mode can substantially improve the detection sensitivity of the MFM. The cantilever is vibrated at, or close to resonance using a small piezo vibrator, as it is raster scanned. The cantilever resonates and reduces the spring constant of the cantilever through the magnetic force gradient and therefore shifts the resonance of the cantilever. This phase shift can be expressed as

$$\Delta\Phi_m = \frac{Q}{k_s}(q\frac{\partial H_z}{\partial_z} + m_x\frac{\partial^2 H_x}{\partial z^2} + m_y\frac{\partial^2 H_y}{\partial z^2} + m_z\frac{\partial^2 H_z}{\partial z^2}) \qquad (2.1)$$

Where Q is the quality factor of the cantilever, k_s is the spring constant of the cantilever, q is the effective magnetic charge of the MFM tip, m_i ($i = x, y,$ and z)

is the effective moment of the tip, and H_z is the vertical component of the sample stray field. To monitor this change the cantilever vibrating frequency is kept constant and the change in amplitude due to the cantilever's shift in resonance is recorded (amplitude detection). Or, the amplitude of the cantilever is kept constant, and the change in resonant frequency is recorded (frequency or phase detection). This results in the force gradient image. Using these methods the sensitivity can be increased by a possible two orders of magnitude. Resonant mode is by definition more complicated to use than static, however it provides much better results.

The topography and magnetic feature can be separated by a two-steps scan, shown in the Figure 2.7. In the first trace the topography is determined. In the second trace the cantilever is lifted to a pre-set height, and scanned using the stored topographic data. As a result the tip-sample separation during the second pass is kept constant and must be large enough to eliminate the van der Waals force. During the second pass the short-range van der Waals force vanishes and the cantilever is affected only by long-range magnetic force. The cantilever resonance oscillations are used to detect the force derivative. By using this two-step scan both the height-image and the magnetic image are obtained simultaneously with this method.

(a)   (b)
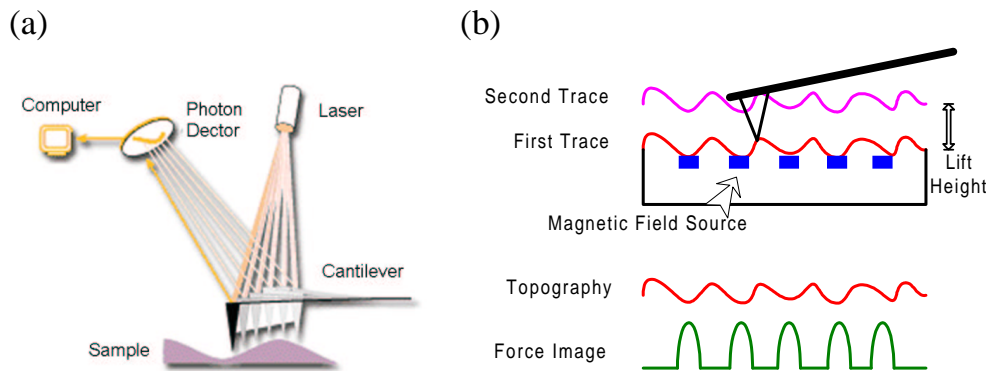
Figure 2.7: Two-pass technique for measurement of magnetic force above sample surface. Each pass has trace and retrace scan lines. The first pass measures the topography and then the tip is lifted to a selected distance for mapping long-range magnetic force.

Chapter 3

Electrical transport in mesoscopic conductors

3.1 Classical conductivity

The electron transport through a crystal with perfect periodic potential is de-scribed by extended Bloch states. However, there is some disordered potential from impurities, defects, dislocations etc. in real samples. In the presence of an electric field, the motion of an electron experiences repeated elastic scattering in the path and is described classically by

$$[\frac{dP}{dt}]_{scattering} = [\frac{dP}{dt}]_{field} \qquad (3.1)$$

The rate at which electrons gain momentum from the external field is balanced by the rate at which they lose momentum by scattering. In the classical picture, the electron is assumed to lose phase coherence after each collision with an impurity, i.e., phase coherence length is the order of the mean free path $l_\phi \sim l_m$. The diffusion equation of the electron motion is given by

$$\frac{\partial n_e}{\partial t} = D\Delta^2 n_e \qquad (3.2)$$

where n_e is the electron density and D is the diffusion constant. The diffusion constant can be related to the elastic mean free path l_m through $D = v_F l_m / d$ with v_F being Fermi velocity and d being dimensions. The electrical conductivity σ is defined by Ohm's law, $J = \sigma E$, describing the linear relation between the electric current density J and the applied electric field, and their average velocity

is assumed to be $\bar{v} = (e/m)\tau E$. Since the current is given by $J = n_e e\bar{v}$, the electric conductivity is deduced as

$$\sigma = \frac{e^2}{m} n_e \tau \tag{3.3}$$

which is known as Drude's formula. Another way to calculate the conductivity is to consider the current as a diffusion of electrons due to the concentration gradient. Replacing $D = v_F^2 \tau/d$ and $dn_e/2E_F = \nu_s$ in Drude's formula, we obtain Einstein's relation

$$\sigma = e^2 \nu_s D \tag{3.4}$$

where ν_s is the density of single-particle states per unit volume at the Fermi energy.

In transport measurement, the directly measurable quantity is only the conductance which is defined as the ratio of current and applied voltage. In a macroscopic conductor the conductivity is an intensive quantity and related to the conductance by $\sigma = G(L/S)$, where L and S are the length and transverse cross-section of the conductor, respectively.

3.2   Quantum conductance

In mesoscopic conductors like carbon nanotubes, the classical description of conductivity breaks down. It is meaningful to use only the measurable quantity − the conductance, which gives appropriate description in various mesoscopic transport phenomena. Let us consider a conductor with characteristic length L smaller than l_ϕ and connected between two electron reservoirs. In the presence of an electric field, the electrons flow through the active region without scattering and move elastically except for a few collisions with the boundaries. This transport is termed *ballistic transport*. There is no voltage drop over the channel but some does occur at the interface of contacts. This originates from the fact that the conductor has less current-carrying modes than both of the reservoirs due to subband formation in the confined structure. This mismatch in the number of modes leads to the redistribution of the current among the different modes, giving rise to the upper limit of conductance. For an ideal 1D system, the current flows through the conductor are given by

$$I = \frac{e}{2\pi\hbar} \int dE[f(E - \mu_1) - f(E - \mu_2)](\sum_i^N T_i) \tag{3.5}$$

$$G = \frac{I}{V_{ds}} = \frac{2e^2}{h} \sum_i^N T_i \tag{3.6}$$

where N is the number of modes at the Fermi energy, T_i is the transmission of each contributing subband, and chemical potential μ_1 and μ_2 on each side of the reservoir with $\mu_1 - \mu_2 = eV_{ds}$. This is the so-called *Landauer formula*. In the case of ideal transmission $T = 1$, the conductance of one mode without spin degeneracy is $G_0 = e^2/h = (25.8 \text{ k}\Omega)^{-1}$, which is called quantum conductance.

Metallic carbon nanotubes have been shown to be ballistic conductors [8, 47], in which the transmission is close to the unity and each conducting channel contributes a G_0 to the total conductance. There are two subbands crossing the Fermi level in metallic nanotubes and this leads to a total conductance of $2G_0$.

3.3   Coulomb blockade effect

3.3.1   Double junction structure

Coulomb blockade effects were first indicated in the finding of non-linear current-voltage characteristics of metal particles embedded in films [13, 51]. The conductance occurs due to tunneling between islands. It was then predicted that the quantization of charge tunneling through a junction would lead current oscillation [1]. This has motivated numbers of studies concerning the transport properties of metal cluster embedded in an insulator and of similar insulator/conductor/insulator arrangements. Figure 3.1 (a) is a schematic drawing of a double junction structure, allowing studies on single charge transport at low temperature. The metal island is separated by two tunneling barriers which weakly couple to two leads. Transferring a single electron from one electrode onto the metal island charges this island negatively by q = −e. Image charges are hence induced on the surrounding electrodes which sum up to +e. It costs

$$E_c = e^2/2C_\Sigma \tag{3.7}$$
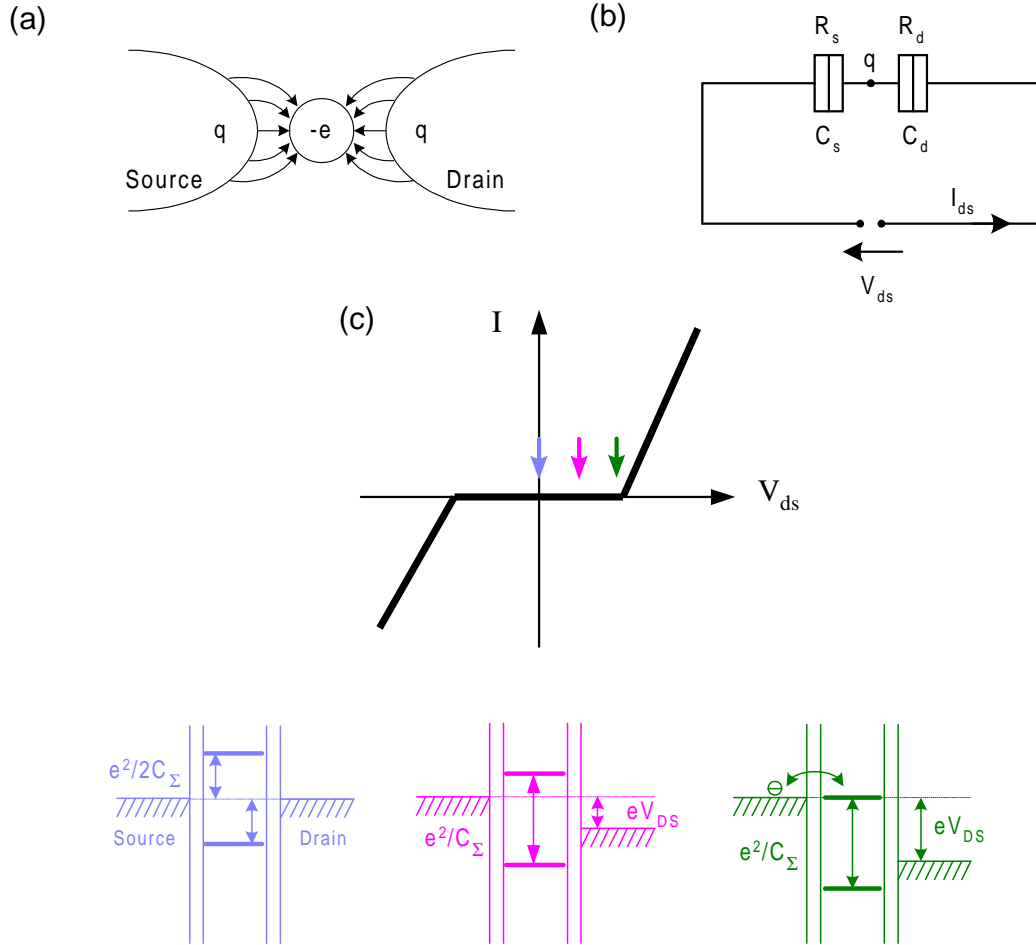
Figure 3.1: (a) Schematic drawing of source/metal/drain junction structure. (b) Corresponding capacitance circuit. (c) Resulting $I - V_{ds}$ characteristics and energy level scheme at different V_{ds}. Bottom panels show the corresponding band diagrams at different V_{ds} as indicated by the colored arrows in $I - V_{ds}$ characteristics.

to charge the island by a single electron, where $C_\Sigma = C_{gs} + C_s + C_d$ is the total island capacitance. This energy is now stored as electrostatic energy in this capacitor configuration and will be released by taking off an electron from the island.

When the size of the metal island is scaled down, the charging energy of a single excess electron on the island increases due to the smaller capacitance.

The single electron charging effect can be observed at a temperature where the characteristic energy $k_B T$ of thermal fluctuations is suppressed until it is lower than $e^2/2C_\Sigma$. Below this critical temperature, the charge transport is blocked within an energy window where no states are energetically accessible for electron tunneling. As shown in Figure 3.1 (c), a conductance gap appears in the $I - V_{ds}$ characteristics since the thermally activated single electron hopping is suppressed. This transport phenomenon is called *Coulomb blockade effect*. Increasing the drain-source voltage V_{ds}, the electrostatic potential of the island is shifted by $C_d/C_\Sigma \cdot V_{ds}$ in reference to the source potential (grounded). It reduces the energy for adding an electron to the island to $E_c - eC_d/C_\Sigma \cdot V_{ds}$, as illustrated in the corresponding energy diagram of Figure 3.1 (c). At the drain-source voltage where $E_c = eC_d/C_\Sigma \cdot V_{ds}$, a single electron can be transferred from the source electrode to the island and then further tunnels through the barrier to the drain electrode, turning on the current in $I - V_{ds}$ characteristics. At this $V_{ds} = e/2C_d$, the N and $N + 1$ states will have the same energy and an electron can tunnel in and out freely, as shown in the green energy level scheme in Figure 3.1 (c). At negative V_{ds}, the electrons tunnel reversely through the source/island/drain arrangement, analogy to charge a hole to the island one by one.

3.3.2 Single electron box

A conventional way to measure the energy required to add or remove electrons is by photoelectron spectrascopy. For instance, the minimum photon energy required to remove an electron is the ionization potential. Nowadays, modern lithography allows for the controlled fabrication of submicron structure, where the single electron effect can be readily observed by introducing appropriate tunneling barriers in the device. The simplest circuit showing charge quantization is the single electron box. Figure 3.2 (a) sketches this two-terminal device, where the island is weakly coupled to the source electrode by a tunneling barrier and only capacitively coupled to the controlling electrode - *gate electrode*. The corresponding circuit diagram is shown in Fig. 3.2 (b). The charge in the island is

$$q = Q_J - Q_G = -Ne \tag{3.8}$$

where Q_J and Q_G are the charge on the junction and gate capacitors, respectively, and N is an integer. The charge q is quantized in units of the elementary charge.

The electrostatic potential of the island can be shifted by applying the gate-source voltage V_{gs}. To transfer an electron onto the island requires an energy change by

$$\Delta E = E_C + \Delta E_G = \frac{q^2}{2(C_s + C_{gs})} - \frac{(q-e)^2}{2(C_s + C_{gs})} + \frac{C_{gs}}{2(C_s + C_{gs})} eV_{gs} = \frac{e(q + C_{gs}V_{gs} - e/2)}{C_s + C_{gs}}.$$
$$(3.9)$$

At $V_{gs} = (N + 1/2)e/C_{gs}$, the ΔE vanishes: an electron feels equal electrostatic energy irrespective of whether it is localized on the island or on the source electrode. The charge q on the island fluctuates between $-Ne$ and $-(N + 1)e$. As a consequence, the electron on the island N can be tuned by changing V_{gs} to a series of specific threshold values, which opens a channel for electrons in the source electrode to tunnel onto the island one by one.
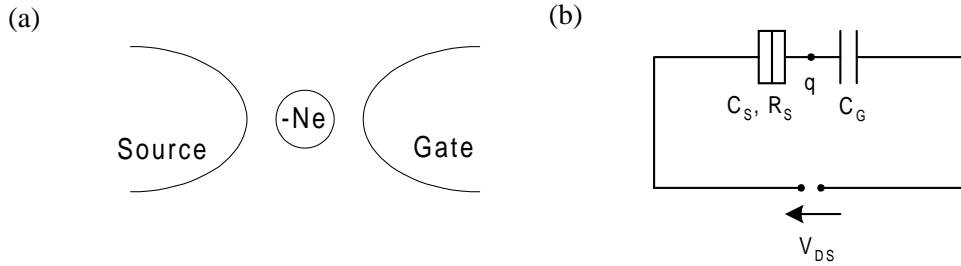
Figure 3.2: (a)(b)Capacitance circuit of source/metal/drain arrangement, as shown in (a).

3.3.3   Single electron transistor

In the previous section we have seen that an electron on the island can be manipulated by applying a voltage V_{gs} between gate and source electrode. No current is measurable in the single electron box arrangement since the island simply functions as a capacitor for accumulating electrons stepwise by $-e$ quanta. By adding a drain electrode to a single box, a three-terminal transistor-like device is formed. As can be seen from the energy diagram, Coulomb blockade of electron transport is present due to the single electron charging energy $e^2/2C_\Sigma$. If we apply a small drain-source voltage which is close to zero, an energy window is opened for driving electron tunneling from the source electrode to the drain electrode. Likewise, sweeping a source-gate voltage V_{gs} allows a series of discrete energy

states to fall within the drain-source energy window one by one. As long as an energy state is available, Coulomb blockade is lifted and current flows through the device, carried by electrons passing the island one by one on their way from source to drain - *single electron transport*. In the current vs. source-gate voltage plot in Figure 3.3 (c), the current is tuned on and off alternatively by sweeping source-gate voltage. This characteristic is termed Coulomb blockade oscillations.

The current flowing through the single-electron transistors can be obtained from the tunneling rate of an electron through the tunneling junctions, which is given by

$$\Gamma(n, n+1) = \frac{1}{e^2 R_{s,d}} \frac{\Delta E(n, n+1)}{1 - exp[-\Delta E(n, n+1)/k_B T]}. \tag{3.10}$$

The probability p_n of finding n electrons in the island may change by leaving the state or by coming into the state from the states $n-1$ or $n+1$ [52].

$$\frac{dp_n}{dt} = \Gamma_t(n+1, n)p_{n+1} + \Gamma_t(n-1, n)p_{n-1} - [\Gamma_t(n, n+1) + \Gamma_t(n, n-1)]p_n \tag{3.11}$$

where

$$\Gamma_t(n, n+1) = \Gamma_s(n, n+1) + \Gamma_d(n, n+1). \tag{3.12}$$

The current I of single-electron transistor is then expressed as

$$I = e \sum p_n [\Gamma_s(n, n+1) - \Gamma_d(n, n+1)]. \tag{3.13}$$

So far, only the charge quantization has been taken into account in transport. The Coulomb blockade model deals with the charge quantization but neglects the energy quantization resulting from the small size of the island. The confinement of the electrons on the island can make the energy spacing of levels discrete. If there are many electrons on the island, they fill up many levels, and the level spacing at the Fermi energy becomes small. In the case of the metallic island, there are so many electrons that the level spectrum is effectively continuous. On the other hand, the energy quantization can be practically resolved in the semiconducting island. One can measure the energy level spectrum directly by seeing the tunneling current at fixed V_{gs} as a function of the drain-source voltage V_{ds}.

The realization of the room temperature single-electron transistor based on quantization is inhibited by some fundamental limitations. The manipulation of

single electron transport depends on the magnitude of the Coulomb gap, e^2/C_Σ, compared to the thermal energy. It is clear that the gap must greatly exceed the thermal energy, $e^2/C_\Sigma \gg k_B T$, to observe the Coulomb blockage effects at a given temperature. Another limit is given by Heisenberg's uncertainty relation: the quantum fluctuations in the particle number, N, must be sufficiently small that the charge is well localized on the island.

$$\Delta E \Delta t > h \tag{3.14}$$

This leads to

$$(e^2/C_\Sigma)(R_{s,d} C_\Sigma) > h \tag{3.15}$$

It restricts the minimum tunneling resistance to $R_{s,d} \gg h/e^2 = 25.8 \text{ k}\Omega$.
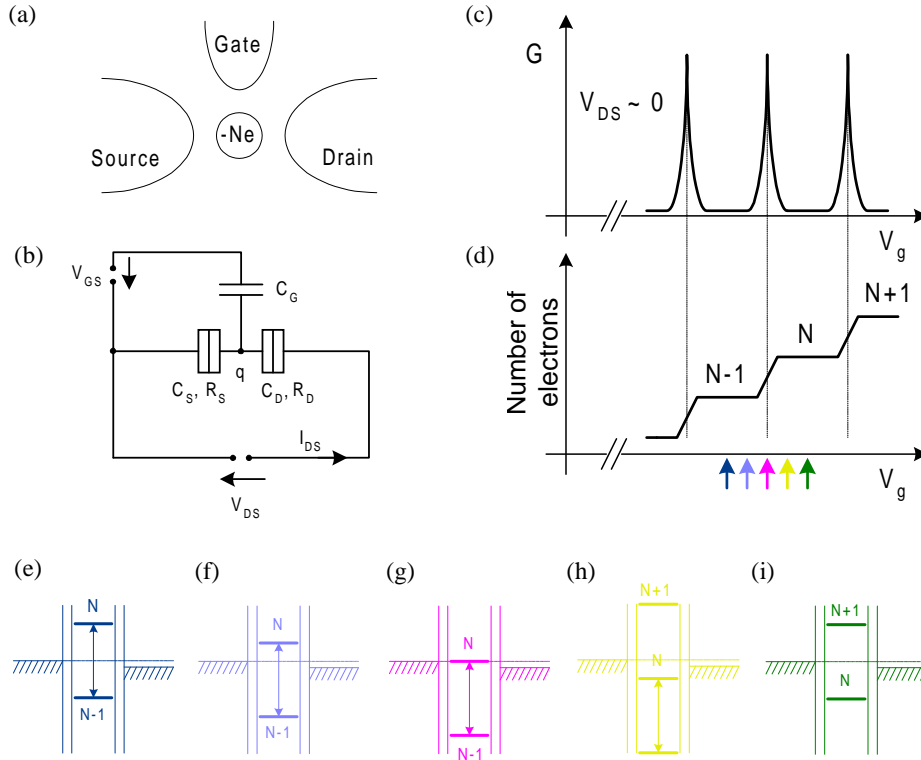
Figure 3.3: (a)The three-terminal geometry of a single electron transistor. (b) Equivalent circuit for a single electron transistor. The tunnel junction is represented by a parallel combination of the tunneling resistance $R_{s,d}$ and the capacitance $C_{s,d}$. (c) Conductance versus gate voltage in the linear response regime of a double junction single electron transistor shown in (a). The conductance of the device oscillates as a function of gate with a period that corresponds to the addition of a single electron to the island. (d) The number of electrons on the island. The number stays constant in Coulomb blockade regime and jumps one charge quantum in single electron tunneling regime. (e) $\sim$ (i) Band diagram of the single electron transistor under different gate voltages. A small V_{ds} is applied across the junction. A gap, e^2/C_Σ, exists in the density of states of the island due to Coulomb charging energy which prohibits tunneling into and out of the island. The electrostatic potential of the island can be modulated by V_{gs} so that a single electron can tunnel through the island. In (e) the system biased off resonance, while in (g) the resonant tunneling is allowed.

Chapter 4

Nanotube peapod transistors

4.1   Introduction

SWNTs are quasi 1D nanostructures with uniform interior space, which provide a natural nanochamber for encapsulating chemical species. As nanotubes, fullerenes are hollow, and various atoms and atom groups can be encaged in their hollow. These materials are called endohedral fullerenes [138]. A new class of material based on the hybridization of both nanotube and fullerene molecules was reported by *Luzzi* [139] in 1998. It is termed nanotube peapod and schematically illustrated in Figure 4.1 for their geometrical structure. The nanotube wall provides a natural confinement to the encapsulated molecules enabling formation of a 1D fullerene chain.

The successful synthesis of nanotubes filled with various fullerene molecules inside the core has initiated an active research field in solid-state physics [68, 70, 140, 143, 144]. As suggested by both experimental [71, 95] and theoretical [46, 115, 129] studies, the entrapped fullerene molecules are capable of modifying the electronic structure of the host tube. It is, therefore, anticipated that the encapsulation of fullerene molecules can play a role in band gap engineering in nanotubes and hence that peapods may generate conceptually novel molecular devices.

In this chapter we will show how we insert metallofullerenes into the open-ended SWNTs and image the encapsulation of metallofullerenes by both HRTEM and MFM techniques. We will show that different packing density in peapods can be assembled by filling metallofullerene molecules in SWNTs with appropriate diameter. In electrical transport measurements, the fully filled $Dy@C_{82}$

peapods show clear temperature-dependent charge transfer between nanotube and encapsulated fullerene molecules, while partially filled Dy@C_{82} peapods can function as ambipolar transistors and offer unique functionalities that go beyond conventional empty SWNT devices. Different functional behaviors are attainable by changing the operating temperature or gate potential.
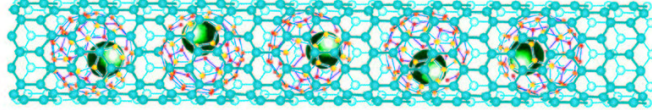
Figure 4.1: Schematic illustration of a nanotube peapod structure. The dysprosium atom is off the center position of the fullerene cadge which are randomly oriented inside the nanotube and form a one-dimensional crystal chain by nanotube confinement.

4.1.1   Band structure modulation by fullerenes

The insertion of fullerene molecules into the interior space of nanotubes can be exothermic or endothermic, depending on the space between constituent units. It is predicted by theories [115, 129] that the tube will sustain its perfect cylindrical shape, and the encapsulation process is exothermic if the distance between the tube wall and the fullerene molecules is substantial. On the other hand, both the nanotube and fullerenes will be distorted if the nanotube-fullerene interspacing is smaller than the van der Waals distance 3.31 Å which is close to the interlayer distance of graphite (3.34 Å). The interaction between the fullerene molecules and the nanotube occurs through a weak orbital mixing between a near-free-electron state on the nanotube and the p orbitals of the fullerenes. In this case, the encapsulation is endothermic and the tube forms a slight undulating shape, giving rise to the severe modification of the electronic structure in both the nanotube and the fullerene molecules. Recent scanning tunneling microscopy studies have shown a drastic modification of the local electronic structure of semiconducting nanotube peapods [71, 95]. As shown schematically in Figure 4.2 (a), the accommodation of metallofullerenes in a small-diameter SWNT causes elastic strains around the site of the peas. In scanning tunnelling spectroscopy measurements

(a)

(b)
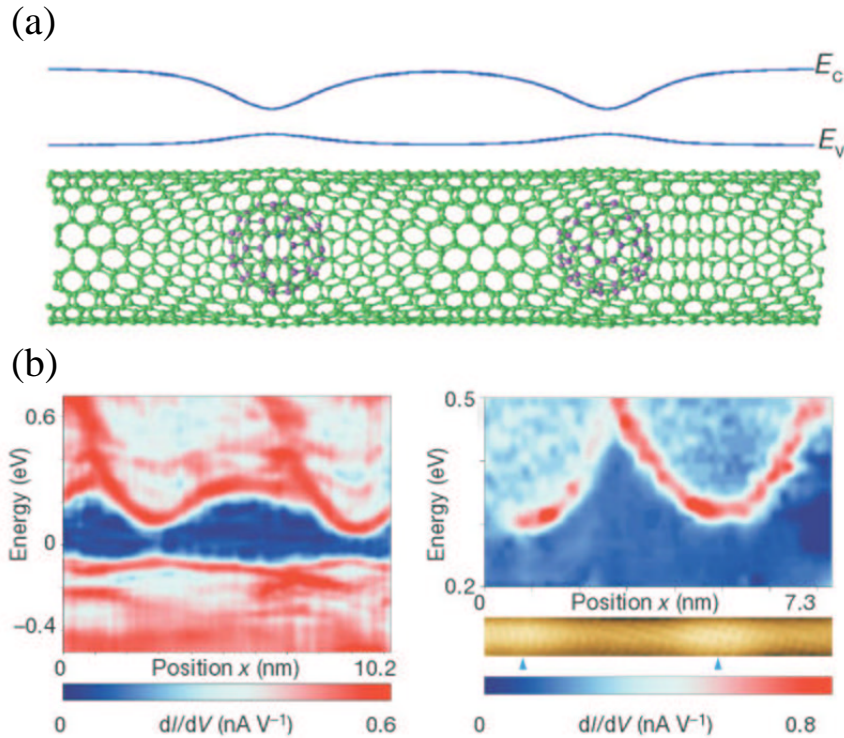
Figure 4.2: (a) Schematic illustration of elastic strain distributed around the site of metallofullerenes in a small-diameter nanotube peapod and the corresponding changes in conduction and valence band edges. (b) Scanning tunnelling spectroscopy of two different nanotube peapods containing $Gd@C_{82}$. The conduction band edge shows a considerable modification induced by $Gd@C_{82}$ molecules [95].

shown in Figure 4.2 (b), the energy band was found to narrow down at the site where the metallofullerenes are expected to be located. The conduction band edge forms an undulating shape, and the band gap has a minimum at the point with greatest circumferential strain.

As discussed in Chapter 1, the electronic properties of carbon nanotubes are decisively dependent on their geometrical structures. Any mechanical perturbations can lead to significant modification of density of states near the Fermi level. This changes can provide a way of band gap engineering in nanotube-based

electronics.

## 4.2   Purification and opening of nanotubes

In SWNTs growth by arc discharge or laser ablation, typical by-products include fullerenes, graphitic polyhedrons with enclosed metal particles, and amorphous carbon overcoating on the sidewall of nanotubes. It is, therefore, necessary to remove these unwanted carbonaceous impurities and metal catalysts before use. By the application of extremely aggressive reagents the aromatic ring system of the SWNTs can be effectively disrupted. This will facilitate the dissolution of the metal catalysts capped at the end of nanotubes or enclosed by carbon polyhedrons.

In our purification process, we first burned the soot materials in the air at 350 °C for 1 hour which was determined from Thermal Gravity measurements. In this process, the curvature-induced high stain in raw carbon materials facilitates the selective oxidation of these carbon by-products and caps of nanotubes, leaving open-ended nanotubes along with catalytic metal particles. Subsequently the resulting metal particles were removed by hydrochloride acid with the aid of low power sonication. The liquid-phase oxidative purification is repeated several times till the HCl solution becomes clear. Figure 4.3 shows the TEM images of SWNTs before and after purification. The nanotubes form a tangled network and are lying on the porous carbon film on a copper grid used in the TEM inspection. We can clearly see that most of the metal particles (dark spots in images) have been effectively removed during purification.

4.3   Insertion of metallofullerenes

The metallofullerenes used in the present studies are synthesized by the arc-discharge method in Prof. Shihe Yang's group in Hong Kong University of Science and Technology. The high purity $Dy@C_{82}$ are extracted by repeated high performance liquid chromatography and monitored by mass spectroscopy.

We have prepared peapods by gas-phase diffusion [68] of $Dy@C_{82}$ molecules into open-ended SWNTs. To ensure the opening of caps the nanotubes were heated in air at 420 °C for 20 minutes. The insertion of $Dy@C_{82}$ was achieved by annealing $Dy@C_{82}$ solid with SWNTs in a sealed quartz tube at 520 °C for 48
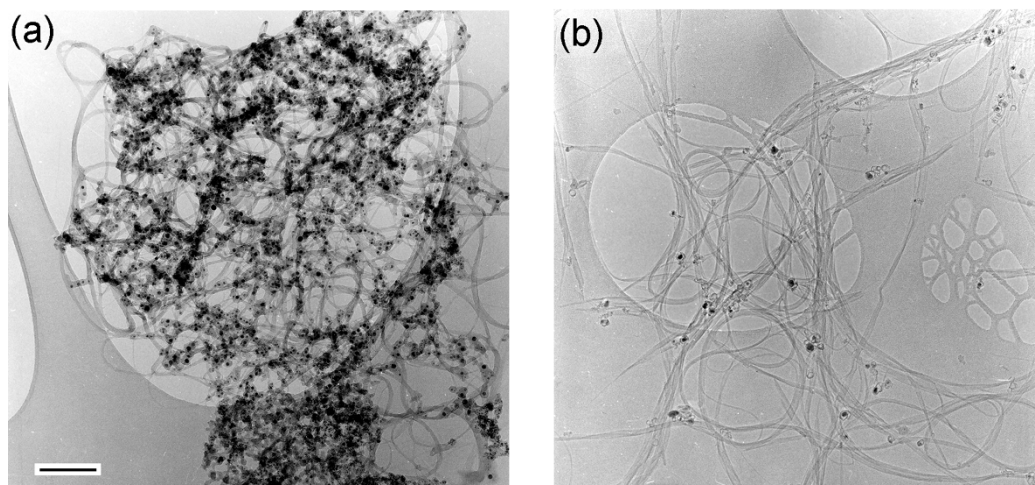
Figure 4.3: TEM images of SWNTs (a) before and (b) after purification. The dark particles in (a) present the metal catalysts decorating around nanotubes. The scale bar is 200 nm.

hours. Subsequently, the resulting SWNTs were rinsed with toluene to remove the residual Dy@C$_{82}$ which may have adsorbed onto the exterior nanotube walls. To confirm the presence and distribution of Dy@C$_{82}$ molecules in the core of SWNTs, HRTEM was employed for imaging. This work is done by cooperating with Dr. Toshiya Okazaki of Nagoya university. Figure 4.4 (a) shows the HRTEM images of the aligned Dy@C$_{82}$ chains encapsulated in SWNTs. The hierarchal structure, metal atoms inside the fullerene cage inside the nanotube, is well illustrated. Figure 4.4 (b) $\sim$ (d) shows the encapsulation of metallofullerenes in individual SWNTs with diameter of 1.55 nm, 1.47 nm and 1.42 nm, respectively. Dark spots seen in some fullerene cages correspond to the encapsulated Dy atoms. This is confirmed by electron energy loss spectroscopy (EELS) spectrum shown in Figure 4.4 (e). Most of the fullerene cages appear empty. This could be due to the spinning of the Dy atom inside the carbon cage. Intuitively, if the tube diameter is small, the creeping of doping molecules will be difficult. Below a critical tube diameter, the total energy calculation [115] shows that the filling takes place endothermally. As can be seen from the HRTEM micrographs, the packing density of metallofullerenes decreases with decreasing tube diameter, and the fullerene molecules are forced to deform due to insufficient interior hollow
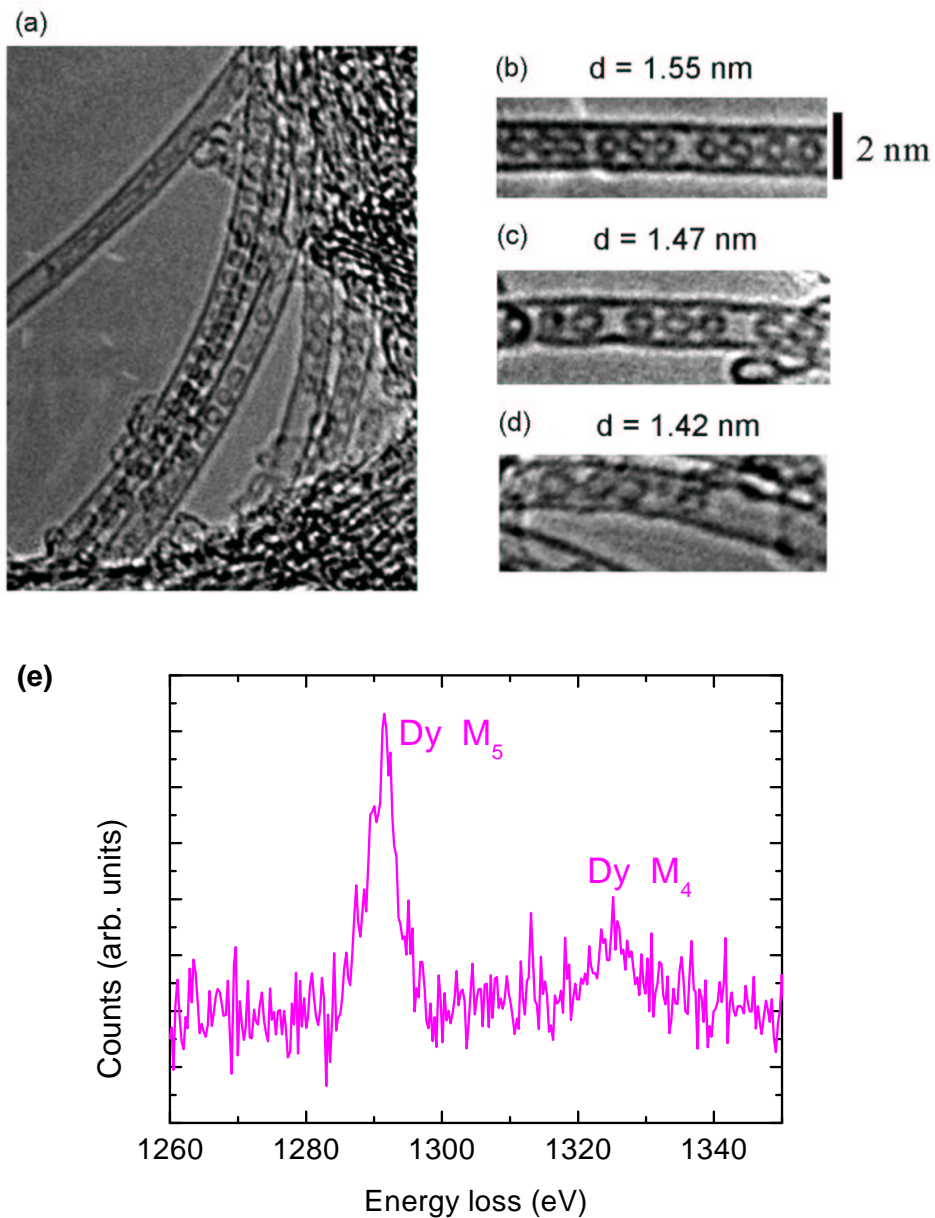
Figure 4.4: Characterization of Dy@C$_{82}$ peapods. (a) HRTEM micrographs of the isolated and bundled SWNTs containing Dy@C$_{82}$ fullerenes. (b)∼(d) Isolated SWNTs with different diameters and packing densities of Dy@C$_{82}$ fullerenes. (e) EELS spectrum of Dy@C$_{82}$ peapods. The two peaks correspond to M4 and M5 adsorption edge of dysprosium.

space in the nanotube. A partial filling can be obtained in the present hybrid structure with nanotube diameter of down to 1.4 nm. In these tubes, $Dy@C_{82}$ molecules become squashed, and the distance between their centers increases.

4.4 Imaging in a magnetic force microscope

An interesting class of endohedral fullerenes are magnetic endohedrals, of which $Dy@C_{82}$ is an example (dysprosium encapsulated in a fullerene cage of 82 carbon atoms). A sophisticated nanostructure is nanotube filled with fullerenes which are filled themselves. In pure dysprosium there is a long range (heli)-magnetic order; $Dy@C_{82}$ is paramagnetic. An interesting question arises as to whether a MFM would be sensitive enough to react to the magnetic force between the magnetic moments of the dysprosium ions and the magnetic coating of an AFM tip. Judging from the literature [86, 111, 119, 142], it should be possible to see an ensemble of about 1000 electron spins. A dysprosium ion in C_{82} is expected to carry about 10 spins at not too low temperatures [72] and if 100 $Dy@C_{82}$ units are in the range of the MFM tip (radius about 50 nm) we should see a signal. And, indeed, we see a magnetic signal if we scan over a thin bundle of dysprosium-fullerene peapods. (The height of the bundle is found to be about 8 nm to judge by the color of the topographic AFM image in Figure 4.5, and from this we estimate the number of tubes in a bundle to be about 50). Figure 4.5 (b) $\sim$ (f) shows a series of such scans using a Dimension 3100 Digital Instrument Oscillating Magnetic Force Microscope in the Tapping mode together with the Lift mode. The microscope sandwiches a magnetic scan between two topographic scans. The interaction between peapods and magnetized tip causes a shift of the resonant frequency of the cantilever. The instrument detects the phase shift which is proportional to the second derivative of the local field. In the MFM images this leads to bright areas for repulsive force and dark areas for attractive interaction. At low lift height (Figure 4.5 (b)) the short range van der Waals forces still dominate over the magnetic forces, or all spins are polarized by the magnetic field emerging from the tip coating, so that we see only a monochromatic contrast due to the attractive force. When the lift height is increased (Figure 4.5 (c)) the magnetic force dominates and magnetic domains seem to appear. These domains apparently change with the scanning direction and with the lift height (The scanning direction is indicated by the arrows at the top of the figures), resembling the domain reversal in soft magnetic structures
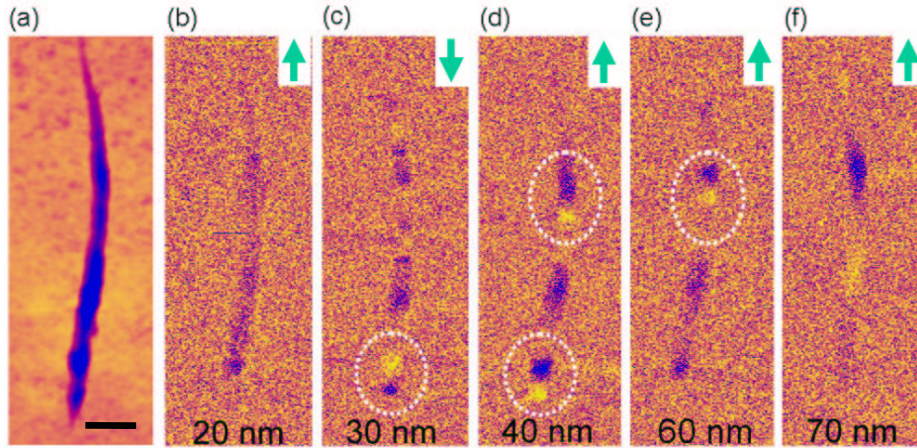
Figure 4.5: Magnetic carbon nanotube peapod. (a) AFM topography of a peapod bundle with height of $\sim$8 nm on average. (Scale bar: 200 nm) (b)$\sim$(f) Corresponding MFM images in (a). The scanning height in Lift mode is shown at the bottom of the images and the scanning direction is indicated at the top. The magnetic reversal is observed by changing scanning direction and marked by dashed ellipse at the bottom of image (c) and (d). Another nanodomain in the bundle is also compared at top of image (d) and (e).

[165]. At the bottom of Figure 4.5 (c) and (d) we see a feature which reverses if the scanning direction is reversed. The origin of these domains is still unclear and further investigations are necessary to show whether they are related to interactions between the dysprosium spins (perhaps mediated by the π electrons of the fullerene cages and of the nanotube walls) or whether they are caused by distortions of the tubes leading to "easy spin directions" or similar phenomena.

4.5 Electrical Transport

4.5.1 In pristine nanotubes

To understand the intrinsic transport properties of Dy@C$_{82}$ peapods we show the electrical transport of pristine semiconducting nanotubes in this section for comparison.

Carbon nanotubes present a micromolecular system with unique electronic properties which vary according to their diameter and chirality. Band structure

calculations have predicted that SWNTs with (n, n) indices are robust metallic having non-vanishing density of states at the Fermi level, whereas SWNTs with (m, n) indices are semiconducting when $m \neq n$. In the case of $m - n = 3p + q$ with non-zero q value, the semiconducting nanotubes have a primary energy gap $E_g \propto 1/d_t$. On the other hand, the energy gap scales as $1/d_t^2$ when $q = 0$. In this section, we discuss the charge transport through pristine individual nanotubes with moderate band gap ($\propto 1/d_t$) or narrow band gap ($1/d_t^2$), both of which have distinct transport properties and are remarkably different from the tubes doped by Dy@C$_{82}$ molecules.
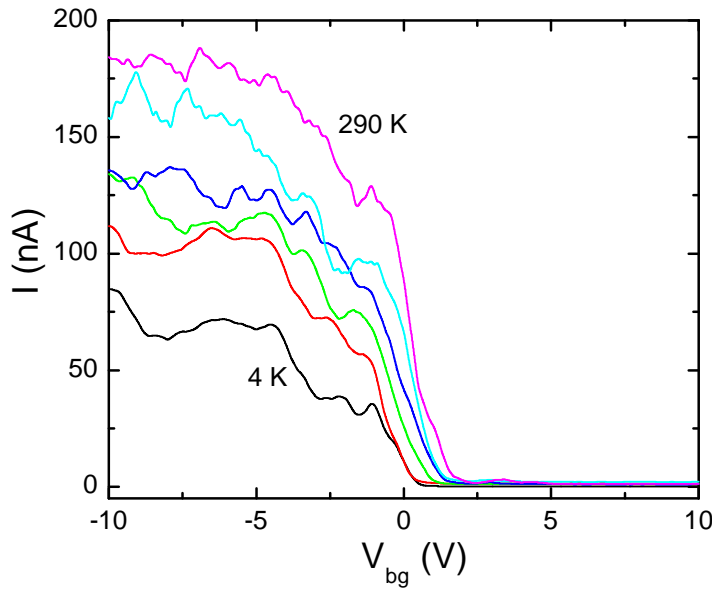
Figure 4.6: The transfer characteristics of an individual pristine nanotube transistor at different temperatures: 4 K, 60 K, 120 K, 180 K, 230 K, and 290 K from bottom to top curves, respectively. The data were taken at $V_{ds} = 60$ mV.

Figure 4.6 shows the transfer characteristics $(I - V_{bg})$ of a device consisting of a pristine individual nanotube with a diameter of 1.6 nm at different temperatures. The nanotube is embedded in two metal contacts designated as "source" and "drain". The nanotube diameter is determined by the AFM height profile. As can be seen in the figure, the current is blocked at positive gate voltage and increases strongly at negative direction. This indicates that a pristine semiconducting nanotube can function as a *field-effect transistor* and the channel current can be modulated by applying a gate voltage, resembling the metal-oxide-

semiconductor FET. The transistor is ON for negative gate voltage, indicating a
p-type conduction. As temperature decreases, the channel current is suppressed,
and the threshold voltage progressively shifts to lower value. The device shows
quite similar transfer characteristics throughout the measured temperature range.
As a result, we only analyze the device performance at room temperature as fol-
lows. At $V_{bg} < -4$ V, the current starts to saturate, i.e., accumulation of holes.
Between -4 V $< V_{bg} < 3$ V, the device is in the hole depletion region and simply
acts like a resistor with a transconductance $g_m \equiv dI/dV_{bg} \approx 3{\times}10^{-8}$ A/V which
is a measure of the switching speed of the device. In a channel-limited FET, we
can deduce the carrier mobility by the following equation:

$$\frac{dI}{dV_{bg}} = \mu_h(\frac{C_t}{L^2})V_{ds} \tag{4.1}$$

where μ_h is the hole mobility, C_t is the nanotube capacitance, L is the channel
length. For nanotubes the gate capacitance can be expressed as:

$$\frac{C_t}{L} \approx \frac{2\pi\epsilon_r\epsilon_0}{\ln(\frac{2h}{r_t})} \tag{4.2}$$

where r_t is the nanotube radius, ϵ_r is the average dielectric constant of device,
and h is the thickness of oxide. Using $L = 150$ nm, $r_t = 0.8$ nm, $h = 100$ nm,
and $\epsilon_r \approx 2.5$, we evaluate a hole mobility of $\mu_h = 30$ cm^2/V·s at $V_{ds} = 60$ mV.
This value is much smaller than the hole mobility of 10^4 cm^2/V·s observed in
graphite [21]. This low mobility could be due to the diffusive transport of holes
through the channel if the device is operated in a channel-limited state [101, 105].
In contrast, if the charge transport through the channel is mainly blocked at the
contacts, then the device functions as a Schottky-barrier transistor [66]. In the
latter case, the equation 4.1 is not valid in extracting the mobility.

The inversion region for electron transport is not observed in the gate range
-10 V $< V_{bg} < 10$ V in present nanotube FET. The band gap of the tube can
be rationally estimated from the tube diameter to be $E_g \simeq 2\gamma_0 a_{c-c}/d_t \approx 500$
meV. In general, fairly high voltages (> 50 V) are required to alter the majority
charge carriers from holes to electrons by back gate electrostatic tuning. This
is the reason why normal semiconducting nanotubes exhibit only unipolar p-
type characteristics under ambient conditions. The p-type behavior of undoped
SWNTs has been studied by several groups and interpreted as contact doping by
metal electrodes, molecular adsorbates, or attachment of chemical groups during
handling [35, 101, 148].
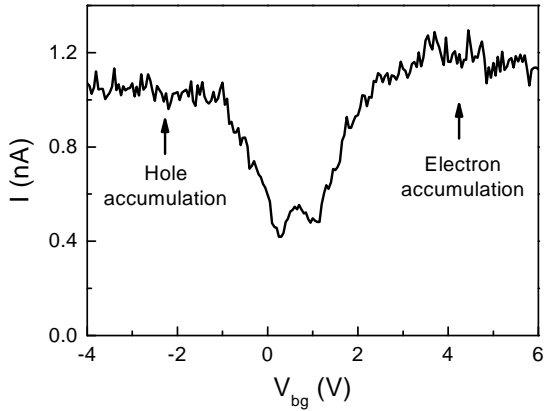
**Figure 4.7:** Transfer characteristics of an individual pristine nanotube with narrow band gap at 200 K.

In Figure 4.7 we show the transfer characteristics of a narrow-gap carbon nanotube FET with diameter of 1.3 nm. The band gap is estimated to be $E_g \simeq 3\gamma_0 a_{c-c}^2/4d_t^2 \approx 25$ meV. Electron and hole accumulation regions are clearly seen in the two saturation regions of the $I - V_{bg}$ curve, respectively. This is due to the shift of Fermi level up to above the conduction band edge or down to below the valence band edge by applying a gate potential. Sitting at the gate voltage of the strong electron/hole accumulation region[1], the energy barrier at the contacts can be evaluated by measuring a set of $I - V_{ds}$ curves at different temperatures. As shown in Figure 4.8 (a), the channel current is symmetric at the positive and negative bias direction due to the two symmetric contact barriers. As expected, the current decreases monotonically with decreasing temperature and depends exponentially on the barrier height presented at the contacts as [146]:

$$I \propto exp(-\Phi_b/k_B T)[exp(qV_{ds}/k_B T) - 1] \qquad (4.3)$$

where Φ_b is the Schottky barrier, k_B is the Boltzmann constant, and T is the absolute temperature. In the charge accumulation region the zero-field asymtotic barrier height Φ_{b0} is the sum of Schottky barrier Φ_b at a specific bias voltage and Schottky barrier lowering $\Delta\Phi(V)$. At small V_{ds}, the current is predominated by the second term in the square brackets in the equation 4.3, i.e., the current flowing from the metal to the semiconductor. The contact barrier can be obtained straightforwardly from the semi-logarithmic plot of the I vs $1/T$. As shown

---

[1]When a gate voltage V_{bg} is applied to the device, part of it appears as a potential drop across the oxide and the rest of it appears as a band bending Ψ_s of the nanotube in question. In the charge accumulation region, the contact resistance R_c starts to dominate the total resistance $R_t = 2R_c + R_{NT}$ of the device. Here the R_{NT} denotes the gate-dependent channel resistance.
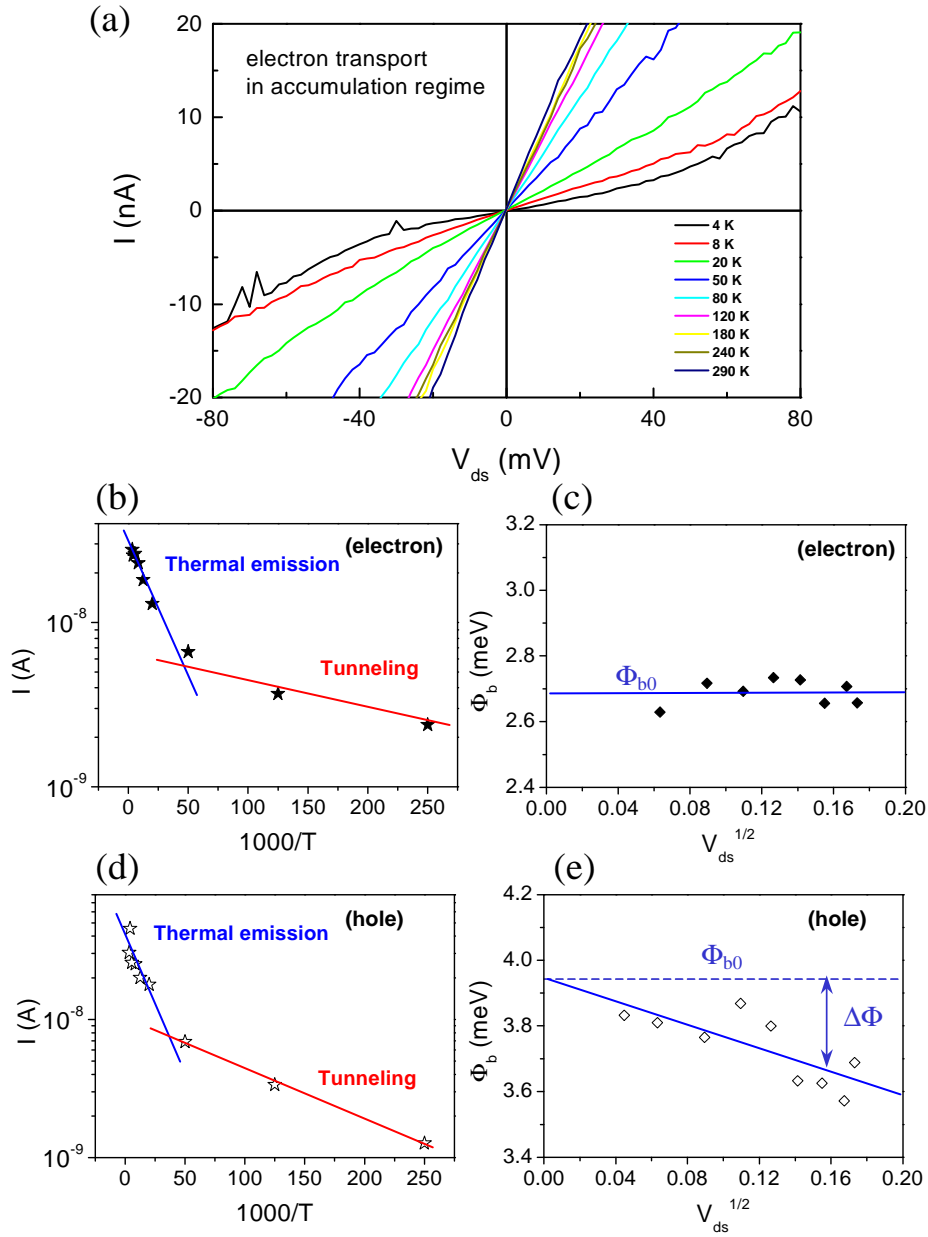
Figure 4.8: Characterization of the barriers for hole (at $V_{bg} = -0.74$ V) and electron (at $V_{bg} = 2.95$ V) injection. (a) Example of $I - V_{ds}$ curves in electron accumulation region for different temperatures. (b) and (d) are the Arrhenius plot for electron transport at $V_{ds} = 30$ mV and for hole transport at $V_{ds} = 30$ mV, respectively. (c) and (e) are the plots of the barrier height as a function of $V_{ds}^{1/2}$. Both zero-field barrier Φ_{b0} and barrier lowering $\Delta\Phi$ are shown.

in Figure 4.8 (b) for electron transport and Figure 4.8 (d) for hole transport, the channel current is mainly attributed to the charge transport via thermionic emission above $\sim$ 30 K and via tunneling below this temperature. The Schottky barrier is caused by the charge transfer at the electrode/nanotube junction and characterized by the work function difference between the contact metal and semiconducting nanotube. The barrier height is reduced by an amount of $\Delta\Phi(v)$ as a result of the image force and the external electric field (bias voltage). As a consequence, the Schottky barrier lowering is proportional to the square root of the electric field. By plotting Φ_b vs $V^{1/2}$, we can extract both the contact barrier at zero bias Φ_b and the bias-dependent Schottky barrier lowering $\Delta\Phi(V)$. Both parameters are obtained for electron transport from Figure 4.8 (b) $\sim$ (c) and hole transport from Figure 4.8 (d) $\sim$ (e), respectively. As can be seen in Figure 4.8(c), the extrapolated intercept shows a barrier of 2.7 meV and there is no apparent image force induced lowering for electron transport. In contrast, a slightly larger barrier, 3.9 meV, is presented in the hole transport and a remarkable $\Delta\Phi(V)$ is observed in the barrier.

4.5.2   In large-diameter peapods

The mono-metallofullerene encapsulating a single lanthanide element, Ln@C$_{82}$ (Ln = Ce, Nd, Gd, Dy, ...), has been confirmed by electron spin resonance and UV-Vis-NIR adsorption spectra to show charge transfer from the encaged atom to the C$_{82}$ cage [117, 138], resulting in the charge state of Ln^{3+}@C$_{82}^{3-}$. The insertion of metallofullerenes into the nanotube is therefore expected to lead to further charge transfer from the C$_{82}$ cage to the tube and the electrical properties of the carbon nanotubes would be substantially modified. This predicted n-type semiconducting behavior may therefore complement the utilization of carbon nanotube-based molecular electronics, since this sort of functionalization is more stable than alkaline metal-doped nanotubes [87] in ambient environments.

Figure 4.9 shows the AFM image of an individual Dy@C$_{82}$ peapod on predefined electrode array. The diameter of the peapod is determined from the AFM height profile to be about 1.6 nm. Judging from our TEM inspections, only nanotubes with an apparent height of $>$ 1.5 nm are rationalized to be fully filled individual peapods. In transport measurements, a back gate voltage is applied to the Si substrate with respect to the source electrode. The current is measured by applying a drain-source bias across the peapod. As in a conventional FET, the
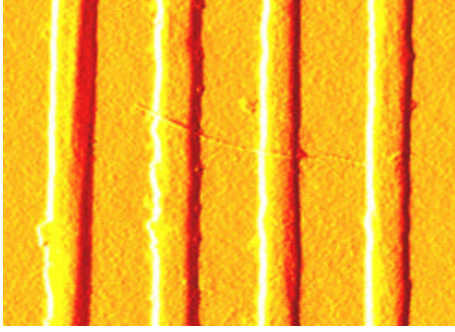
Figure 4.9: AFM image of an individual $Dy@C_{82}$ peapod on predefined electrode array. The electrode gap is 150 nm.

gate voltage modulates the carrier (electron or hole) concentration in the conducting channel (tube) and allows an investigation of the transport mechanism.

Figure 4.10 depicts the gate dependence of the conductance along a fully filled $Dy@C_{82}$ peapod at various temperatures. From the sign of the response to the gate voltage, the n- or p-type character of the conductance can be determined. In Figure 4.10 (a), the p-type semiconducting behavior is clearly seen at room temperature. The conductance increases for negative gate voltage, indicating that the peapod behaves as a p-channel FET similar to undoped semiconducting SWNTs as discussed above. Positive V_{bg} can deplete holes and reduce the conductance to immeasurably small values. As the temperature decreases to 265 K, a *positive* V_{bg} enhances the conductance, implying that now more electrons are accumulated in the nanotube and starting to dominate the transport. Hence, now decreasing V_{bg} inhibits the charge transport. The change from p-type semiconducting character to n-type as a function of temperature has not been observed in pristine nanotubes. It is reasonable to attribute this effect to the transfer of electrons from the $Dy@C_{82}$ molecules to the SWNT, analogous to graphite intercalation compounds.

As the temperature is decreased further, more electrons are transferred to the nanotube, leading to a shift of the Fermi level up into the conduction band. Below the temperature $T \sim 215$ K, no gate voltage dependence, neither p- nor n-type, is observed and metallic behavior is evident.

Figure 4.11 displays the $I - V_{ds}$ curves (at zero gate voltage) for different temperatures. At moderate temperatures (above 100 K), they are linear, suggesting that the metal leads form an ohmic contact to the tube. Down to 215 K, the current decreases steadily upon cooling, consistent with semiconducting behavior. However, as temperature decreases further, the current starts increasing, especially at $V_{ds} < 0$. The increase in current corresponds to the changes
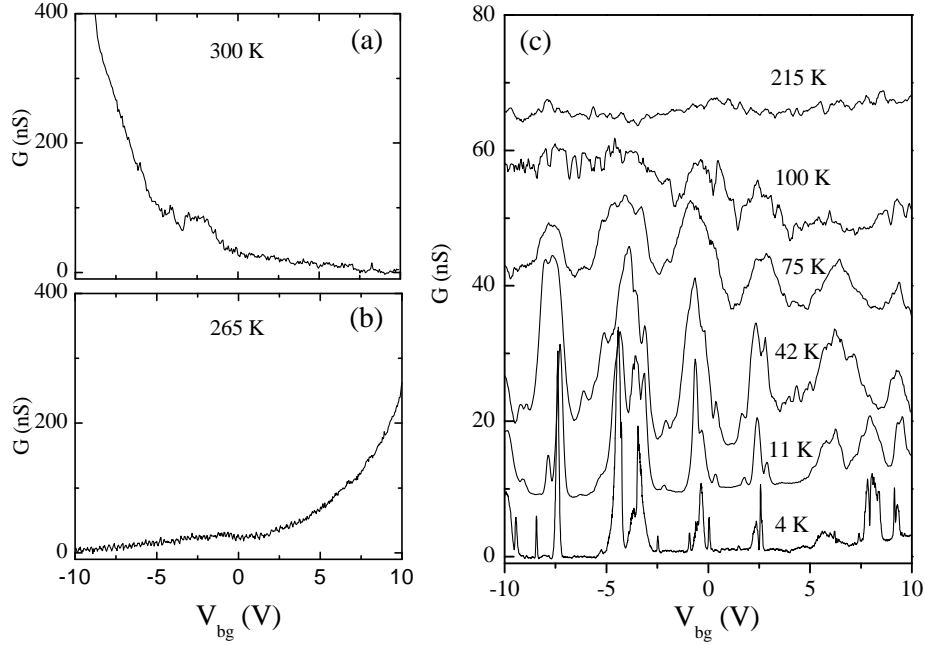
Figure 4.10: (a)∼(c) Gate voltage dependence of conductance measured at $V_{ds} = 4$ mV at various temperatures. The curves in (c) are unequally displaced for clarity.

of carrier concentration in conducting channels and is attributed to the charge transfer from the metallofullerenes to the tube, as discussed above. The observed crossover temperature T^* in $I - V_{ds}$ curves is consistent with that in the gate dependent conductance.

Below $T \sim 75$ K, the $I - V_{ds}$ curves show several wigglers and steps (Figure 4.11 (b)). The contact barriers block the electron wave from penetrating into the electrodes, yielding a Coulomb island well decoupled from the electrodes. The number of electrons in the nanotubes is therefore quantized and Coulomb staircases emerge in the $I - V_{ds}$ characteristics. This behavior is in accordance with the conductance oscillations as a function of the gate voltage in Figure 4.10 (c). They show a periodic spacing of $\Delta V_{bg} \sim 3.5$ V. Such single electron charging effects are well known from other quantum dot systems [52].

The observed Coulomb staircase in $I - V_{ds}$ characteristics is due to asymmetric junction barriers, i.e., either the capacitance or the tunneling resistance are quite different. Assumed that the two capacitances are similar but that the tunneling resistances are rather different, with $R_d \gg R_s$. In this case, the limiting rate
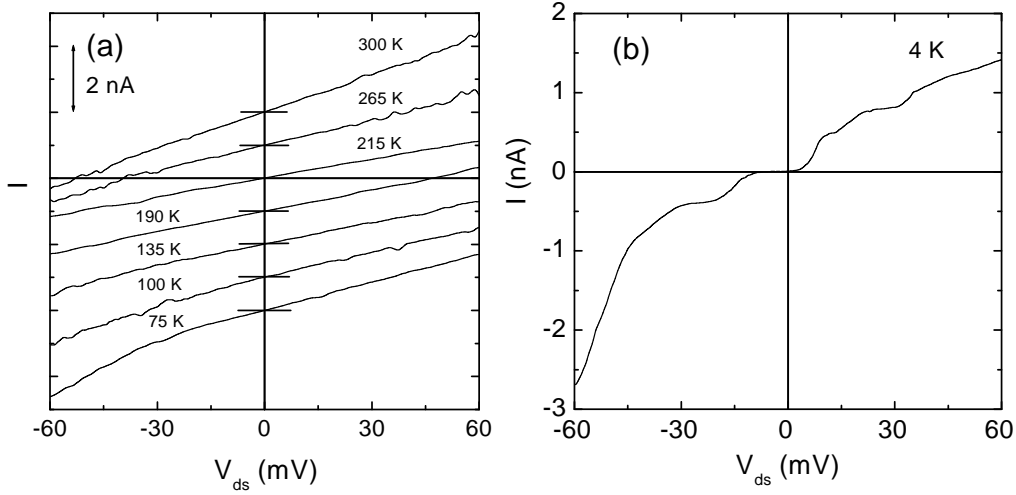
Figure 4.11: (a) $I - V_{ds}$ characteristics of an individual nanotube peapod at different temperatures. They are equally shifted by 1 nA offset for clarity. (b) nonlinear $I - V_{ds}$ curve at 4 K showing single electron charging effect.

is tunneling through the drain barrier. As soon as an electron tunnels out of the island through the drain junction, it is immediately recharged by the source junction. Under these conditions, the current is approximately controlled by the voltage drop across the drain junction, which is given by $V_d = C_s V_{ds}/C_\Sigma + Ne/C_\Sigma$. The voltage across the drain barrier therefore jumps by an amount e/C_Σ whenever the threshold for increasing N is reached for the source junction. The corresponding current jumps are given by $\Delta I \approx \Delta V_d/R_d = e/C_\Sigma R_d$.

The conductance curves at low temperature could reveal information on the dopant distribution and the quantized charging effect of the peapod transistor system. The conductance peaks appear when a new quantized state in the nanotube dot becomes energetically accessible, yielding single electron charging. At 4 K, the conductance peaks split into two or three subpeaks with irregular peak spacing and amplitude. Between $7.5 \text{ V} < V_{bg} < 8.5 \text{ V}$, the conductance peak turns into multiple subpeaks with periodic spacing of $\Delta V_{bg} \sim 0.3$ V. The dot size can be estimated using equation 4.2 in the Coulomb blockade regime, where $C_g = e/\Delta V_{bg}$. This evaluation leads to $L \sim 150$ nm and is consistent with the tube length defined by the distance between the drain and source electrodes. The larger $\Delta V_{bg} \sim 3.5$ V corresponds to a smaller dot size ($L \cong 2$ nm). The system behaves as multiple dots in series inside the nanotubes.

To interpret the experimental findings, we propose a possible mechanism for temperature-dependent charge transfer in nanotube peapods. The Dy@C_{82} inside the nanotube forms a linearly aligned molecular chain with energetically stable van der Waals separation between the tube wall and the C_{82} cage. At low temperature, thermal contraction reduces the diameter of the tube, leading to a reduction in the distance between the tube wall and C_{82} cage. The shrunken Dy@C_{82}-nanotube spacing essentially distorts the lattice structure of the tube, forming an undulant tube shape [115]. The distortion of the nanotube might also make Dy@C_{82} elongate along the tube axis. The changes in shape and curvature can significantly modify the electronic structure of both the nanotube and the encapsulated metallofullerenes (see Appendix A). The reduced separation between the tube wall and the C_{82} cage also make the overlap and hybridization of electronic states more likely, which facilitates the charge transfer.

From the individual peapods examined, we have not found a universal p to n transition temperature. This is reasonable, since different tubes are expected to have different diameters. Therefore, the distance between fullerene and nanotube wall will vary and hence the charge transfer. Moreover, the electronic structure of a nanotube (the density of states and the position of singularities in this density) depends on the diameters and on the helicity of the tube, again affecting the charge transfer differently for different tubes. In addition, the quantity of encapsulated Dy@C_{82} was also found to play an important role in determining transition temperature. In the case of partially filled nanotube peapods, it tends to be the case that the conversion of p- to n-type will be observed at lower temperature. This may be interpreted in terms of concentration-dependent charge transfer.

Since the tube structure is supposed to be distorted by entrapped metallofullerenes at low temperatures, the modification of the nanotube band structure should also be taken into account. Due to local lattice deformation, the Fermi wave vector $\mathbf{k}_F$ in the nanotube can be shifted, leading to changes in the shortest distance between $\mathbf{k}_F$ and allowed subbands. This changes the band gap accordingly. In semiconducting tubes, the band gap can be enlarged or reduced, depending on the relative position of the shifted $\mathbf{k}_F$ to the subbands [161]. The gap opening in robust metallic tubes should also become observable as the temperature changes. This is in good agreement with the experimental findings in doped metallic tubes which start to exhibit semiconducting behavior at low temperatures. The combination of these two effects may be the reason that the electrical

properties of peapods at different temperatures becomes so complicated.

4.5.3   In small-diameter peapods

Individual SWNTs with a diameter of about 1.4 nm were selected for contacting by electron-beam lithography and followed by three-terminal transport measurements. We characterize the transport properties of the partially doped peapod transistors as a function of temperature, drain-source bias, and gate voltage V_{bg} in both "tube-on-top" and "metal-on-top" configurations. Figure 4.12 schematically shows the device in a metal-on-top setup.
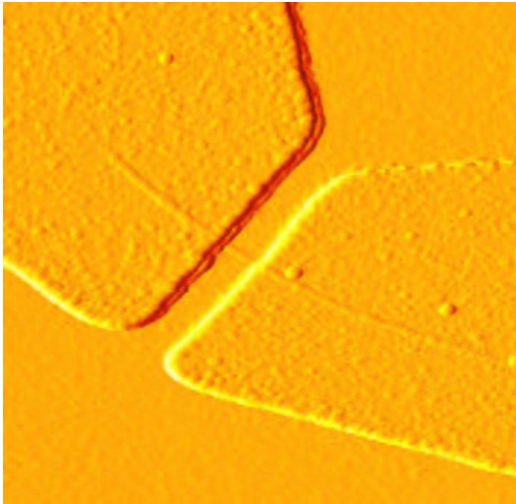
Figure 4.12: AFM image of an individual Dy@C$_{82}$ peapod contacted by two electrodes on top. The electrode gap is 70 nm.

The representative transport characteristics of a partially filled semiconducting Dy@C$_{82}$ peapod in the metal-on-top setup is shown in Figure 4.13 which displays the evolution of the current I vs. gate voltage V_{bg} with temperatures. At room temperature, the semiconducting Dy@C$_{82}$ peapod functions as a p-type unipolar transistor (i.e., The current in $I - V_{bg}$ curve diminishes to an immeasurable state at $V_{bg} > 0$.). From 230 K downward, the clear p-type behavior turns into asymmetric "ambipolar" transport (hole conduction at negative V_{bg} and electron conduction at positive V_{bg}). This is in sharp contrast to the pristine carbon nanotube FETs with moderate band gap (typically 400 meV $\sim$ 800 meV), in which the current flow over the experimentally accessible positive V_{bg} range ($0 \leq V_{bg} \leq 50$) is always blocked due to the persistent p-type character [37, 106]. It is noted that a different, but conceptually similar, ambipolar behavior has recently been observed in large-diameter tubes [77], narrow-gap tubes (as discussed in section 4.5.1) [163], TiC contacted tubes [102], or strongly capacitive-coupled tubes

[9]. In these cases, the conductance changes from p-type to n-type by sweeping the gate voltage. In metallofullerene peapods, however, the "ambipolar" behavior is observed when the temperature is swept.

The ability to operate FETs in an ambipolar state is important for the construction of complementary electronics that are known to be superior in performance to unipolar p- or n-type FETs [75]. Similar ambipolar transport is also seen upon further cooling. Figure 4.13 (b) depicts the transfer characteristic at 4 K in extended gate potential. The regions in hole and electron conduction correspond to the "on" state of the transistor, while the region in the gap is the "off" state. The gate potential can effectively modulate the channel current by about five and four orders of magnitude in hole and electron conduction, respectively. The transistor in the hole conduction stage shows a transconductance $g_m = 2 \times 10^{-8}$ A/V, while g_m reduces to 2×10^{-10} A/V in the electron conduction stage. The transconductance reflects the carrier mobility, and this profound difference in g_m could be an indication of electron hopping transport in the undulating conduction band edge shown in the STM investigation [95]. Figure 4.13 (c) shows the current in both electron conduction (at $V_{bg} = 5.84$ V, single electron tunneling regime at low temperature) and hole conduction (at $V_{bg} = -6$ V) as a function of temperature T. Four distinct regimes are seen. At high T (region I), the device only conducts at $V_{bg} < 0$, while at intermediate T (region II) the current decreases drastically at $V_{bg} < 0$ and increases at $V_{bg} > 0$ upon cooling. The suppression of current transport in the hole conduction stage (Figure 4.13 (c) open circles) is a consequence of freezing out of thermally activated charge carriers when the temperature decreases [146]. In contrast, the increase of current transport in the electron conduction stage (Figure 4.13 (c) solid squares) can be understood by temperature-dependent electron transfer from Dy@C$_{82}$ to the nanotube π^* band [31]. The coupling between C$_{82}$ molecules and the nanotube is speculatively enhanced by thermal contraction of the nanotube, facilitating the charge transfer with decreasing T. In the third transport regime (region III), the current at $V_{bg} > 0$ starts to decrease progressively and then vanishes to zero at a crossover $T^* = 125$ K. In addition, there is another regime (region IV), which has no analog in conventional semiconductor devices. The current at $V_{bg} < 0$ drops to a minimum and the current at $V_{bg} > 0$ increases monotonically again down to 4 K. It is interesting to note that the peak in this $I - T$ curve of electron conduction corresponds to the dip in that of hole conduction and vice versa.

The corresponding output characteristics ($I - V_{ds}$ curves) at different temper-
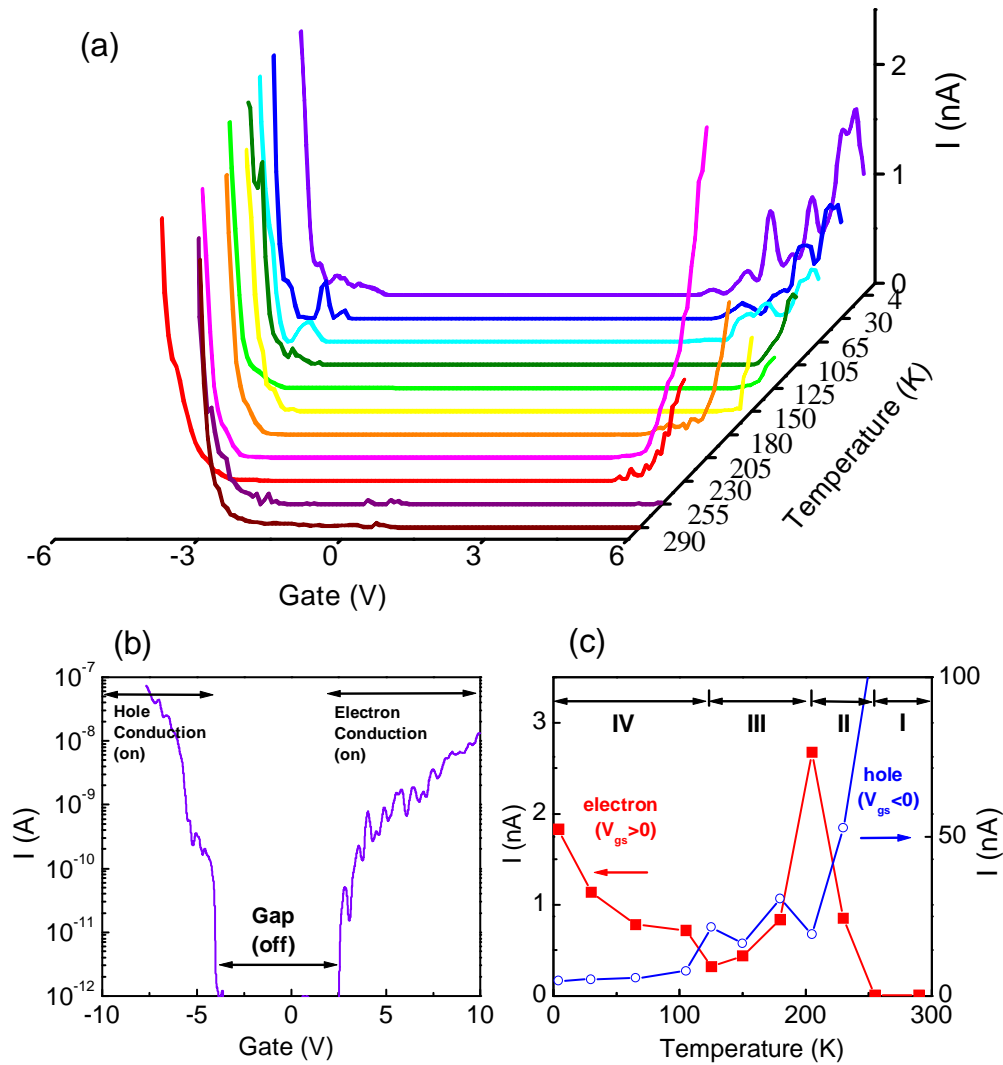
Figure 4.13: Charge transport in a partially filled peapod FET in
"metal-on-top" setup. (a) Transfer characteristics at various temper-
atures. Data were taken at $V_{ds} = 0.3$ V. (b) Transfer characteristics
of the same transistor at 4K in logarithmic scale and extended gate
voltage. (c) Current as a function of the temperature at $V_{bg} = 5.84$ V
(solid square) and $V_{bg} = -6$ V (open circle). Four distinct transport
regimes are marked.
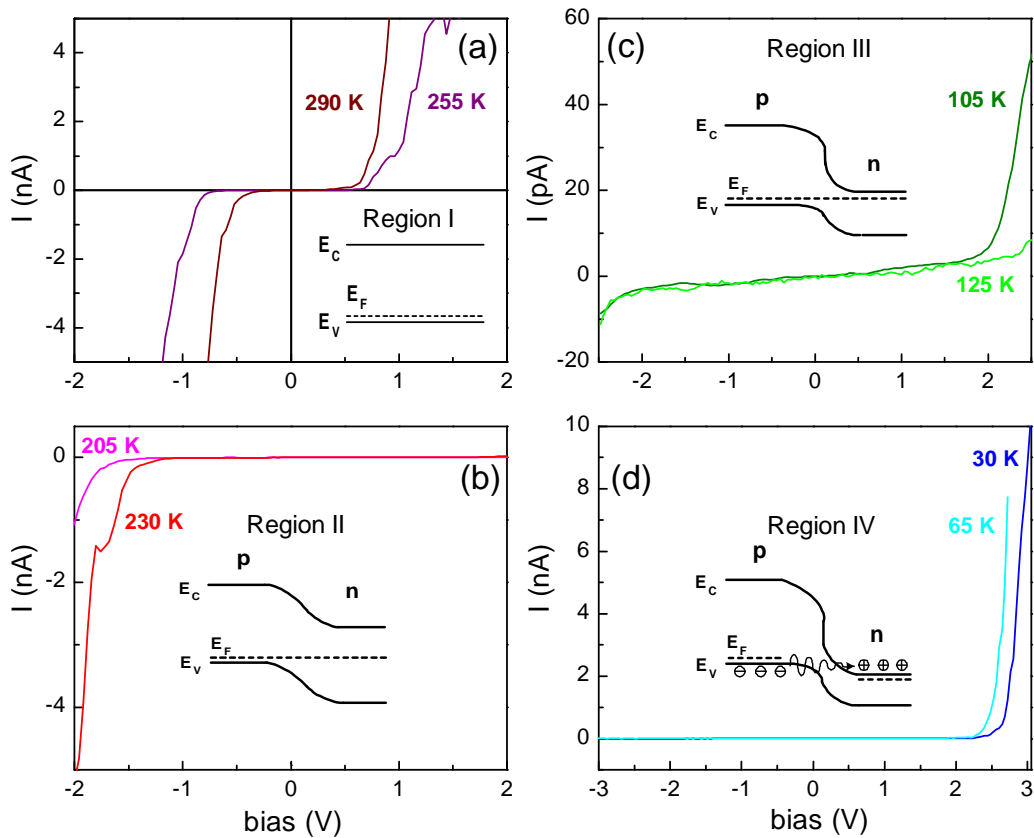
Figure 4.14: Two-probe output characteristics of a partially filled peapod transistor at different temperatures in "metal-on-top" setup, taken at zero gate voltage, and the suggested band diagrams at four corresponding transport regimes. (a) Charge transport before electron doping by metallofullerenes. E_C, E_F, and E_V represent the conduction band, Fermi level, and valence band, respectively. (b) The rectifying behavior appears when it is cooled. The band starts to bend due to the successive upshift of the Fermi level in the filled segment, which functions as n-type. (c) The turn-on voltage at both bias directions becomes progressively equal in this regime. (d) The rectifying direction reverses. The alignment of the valence band edge in the p-side, to the conduction band edge in the n-side, results in band-to-band tunneling. The band diagram shows electron tunneling at bias > 0.

atures provide an excellent insight into the transport mechanism discussed above. In region I (Figure 4.14 (a)), the $I - V_{ds}$ curves are nonlinear and a pronounced gap-like nonlinearity develops upon cooling. In region II (Figure 4.14 (b)), the current at positive V_{ds} is blocked and a diode-like rectifying behavior appears, consistent with the emergence of the asymmetric $I - V_{bg}$ plot in Figure 4.13 (a). From 230 K downward, the charge transfer in the filled tube segment results in the formation of an intra-tube p-n junction. As the temperature approaches T^*, the turn-on bias voltage for reversed current is successively reduced compared to the forward current (Figure 4.14 (c)). Below T^*, the current flow is blocked in the *opposite direction* ($V_{ds} < 0$), showing a reversal of rectifying direction (Figure 4.14 (d)). A possible scenario in terms of semiconductor band structure is indicated in the insets to Figure 4.14. Around room temperature (Figure 4.14 (a) inset), the bands along the nanotube are flat and the Fermi level is close to the valence band. The output characteristics are determined by blocking contact resistance at both interfaces between nanotube and gold electrodes [66]. When the temperature is lowered (Figure 4.14 (b) inset), the reduced nanotube-Dy@C$_{82}$ interspacing intensifies the coupling of π orbitals and makes the hybridization of electronic states more likely, facilitating electron transfer with decreasing temperatures. This leads to a rectifying behavior. In region III (Figure 4.14 (c) inset), the conduction band modulation induced by the "peas" might play an important role at low temperature. The energy gap narrowing [95] of the n-side in combination with temperature-dependent charge transfer initiates the alignment of the conduction band edge of the n-side to the valence band edge of the p-side. The polarity of rectification is reversed since now the bands in the filled region are lowered so much that band-to-band tunneling becomes possible [137]. At a small reversed bias, the valence band electrons can directly tunnel into the empty conduction band state opposite them on the n-side without first being excited into the conduction band on the p-side.

These particular transport features are also reproducible in a partially filled Dy@C$_{82}$ peapod lying on predefined electrodes, which provide higher contact resistance and allow us to examine whether the observed transport phenomena are determined by charge transport along the bulk length of the tube or by contact barriers. We find that the tube consistently shows the p-type behavior at room temperature. The current increases with decreasing gate voltages (Figure 4.15 (a)). At intermediate temperature, rectifying behavior appears (Figure 4.15 (b) at zero gate). Further cooling facilitates the band offset and consequently

the reversal of rectification in $I - V_{ds}$ characteristics (Figure 4.15 (c)). Since the filling of metallofullerenes inside the tube causes the changes of electronic structure, a common gate will shift the Fermi level on the two sides to different energy levels: The rectifying direction should be switchable not only by changing temperature but also by applying a gate potential. Indeed, we observe this effect at a temperature where the conduction band edge in the filled segment is about to align with valence band edge in the unfilled segment (Figure 4.15 (b)). An unequal shift of band edge in the two sides can also lead to the reversal of rectification, as illustrated in the drawing of suggested band structures at the filled/unfilled interface next to Figure 4.15 (b).

Although the above interpretation accounts for the major feature of transport in the data, many interesting aspects of this system remain to be explored. For example, the mechanism responsible for the band gap narrowing in metallofullerene peapods is yet unsettled. Whether the magnetic field originating from the rare earth atoms plays a crucial role in device operation is another unclear question. Despite these, Dy@C_{82} peapods bring about new perspectives in carbon-based electronics and superior device functionalities than conventional electronic materials, especially for the most basic and widely-used device units, field-effect transistors. We believe that the ability to design the electronic devices in molecular scale with multiple functionalities will be important in the emerging technology of nanoelectronics.
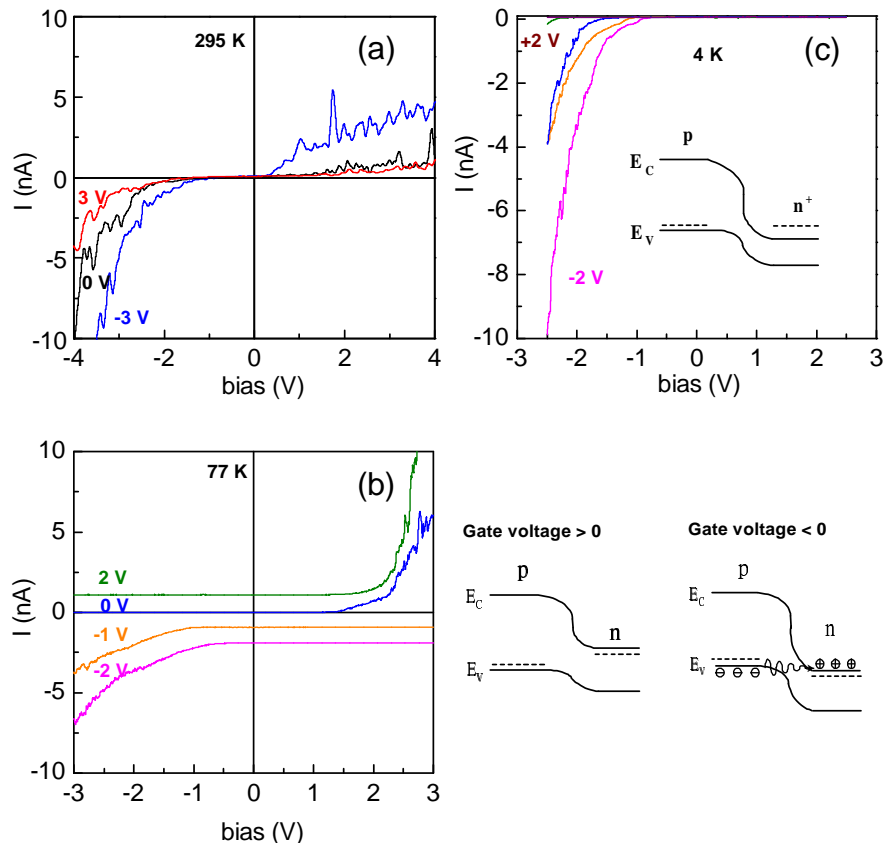
Figure 4.15: Two-probe output characteristics of a partially filled peapod transistor at different temperatures in "tube-on-top" setup, and the suggested band diagrams at different gate voltages. (a) Gate-dependent $I - V_{ds}$ curves at room temperature. Gate voltages are indicated on the corresponding $I - V_{ds}$ curves. (b) Gate-dependent $I - V_{ds}$ curves at 77 K. The data at different gate voltages are equally shifted by 1 nA for clarity. Gate voltages are indicated on the corresponding $I - V_{ds}$ curves. On the right side of (b) two drawings are shown, which illustrate the suggested band offset at positive gate voltage (left drawing) and negative gate voltage (right drawing).(c) Gate-dependent $I - V_{ds}$ curves at 4 K. Inset shows the suggested band structure at the filled/unfilled interface.

Chapter 5

Interconnection of carbon nanotubes

5.1 Introduction

Carbon nanotubes have opened up new possibilities for novel components in miniaturized electronic devices. They are one-dimensional structures that exhibit metallic or semiconducting behavior. Semiconducting nanotubes can function as active channels in field-effect transistors [101, 148], in nanorectifiers [5], or in logic circuits [9, 38, 99]. Metallic counterparts can be used as interconnections in future electronic devices, or as a gate for local modulation of the electronic states in the active channel.

To achieve this goal, a controllable growing technique or chemical functionalization of carbon nanotubes [69] will be the first step toward their possible application. In this chapter a defect chemical functionalization method is introduced. We will show that stable chemical functional groups can be incorporated into the nanotubes without destroying their intrinsic 1D electronic structure. The attached molecules function as linkers for bridging two carbon nanotubes in an end-to-end or end-to-side arrangement. T-shape intermolecular nanotube junctions which are designed for all-carbon transistors can then be formed. The synthesis process of nanotube junctions as well as the characterization by Raman spectroscopy and X-ray photoelectron spectroscopy (XPS) are given in detail in the present chapter. The transport properties of these junctions will be presented in the following chapter.

In addition to link nanotubes, attachment of functional groups is also antic-

ipated to act as dopants or acceptors in nanotubes. Due to the doping effect from adsorbed oxygen molecules [145] and the charge transfer with defined electrodes [148], pristine carbon nanotubes show p-type semiconducting behavior. For complementary logic circuitry, various chemical modifications achieved by doping semiconducting nanotubes have been demonstrated. However, the stability of alkali-metal doped nanotubes [17, 53, 87] is sensitive to the ambient environment, and endohedral metallofullerene doping is strongly dependent on the inner diameter of the host nanotube [33, 139, 143]. Therefore, ambient stable chemical doping by derivatizing negatively charged functional groups on tube wall will also be a good starting point for the use in band gap engineering [43] as well as for the formation of electrically reliable intrajunctions.

5.2   Chemical functionalization

In recent years, several sorts of chemical functionalization on carbon nanotubes have been reported and can be classified as: functionalization on defect groups [27]; covalent sidewall functionalization [10, 20, 109]; non-covalent exohedral functionalization [11, 29]; and endohedral functionalization [140]. During the covalent functionalization the bond structure of the nanotube will be changed because it needs to transform a number of sp^2 carbon atoms to sp^3 [50]. To avoid this unclear perturbation on the electronic structure of nanotubes, we adopt the first approach for chemical modification of SWNTs achieved by mainly attaching functional groups at the sites of defects on the nanotubes.

It is well known that graphite is chemically inert. When a graphite layer is rolled up to form a cylindrical structure, its chemical reactivity is modified. This stems from the curvature-induced pyramidalization and misalignment of the π-orbitals of the carbon atoms, giving rise to a local strain in carbon nanotubes [28, 58, 141, 152]. From the standpoint of chemistry, carbon nanotubes can be divided into two regions: the end caps and the sidewall. The end caps resemble a hemispherical fullerene and hence have a much higher pyramidalization angle than the sidewall, e.g., in (5, 5) SWNT the pyramidalization angle is $\theta_p \sim 11.6^{\circ}$ in the cap and $\theta_p \sim 6.0^{\circ}$ in the sidewall [112]. This ensures that the caps are always more reactive. However, another structural strain arises from the π-orbital misalignment. There are two types of bonds in the hexagonal carbon network, which orient differently in the curved nanotube sidewall: Taking an (10, 10) armchair nanotube as an example, one bond runs perpendicular to the tube axis

and another one is 30° away from the tube axis. This results in a π-orbital misalignment angle $\phi_\pi = 0°$ in the former bond but $\phi_\pi = 10.4°$ in the latter case. The π-orbital alignment of carbon atoms in fullerene is almost perfect, but it is not the case in a nanotube sidewall having the same diameter with the fullerene. It is the relief of these strains which accompanies addition reactions in the caps and sidewall of nanotubes.

Figure 5.1: Sequence of chemical functionalization in carbon nanotubes. In step *1*, the chloride acid groups are attached to the ends or sidewalls of the nanotubes. In step *2*, two different amine functionalities are incorporated into the nanotubes by replacing the chloride acid groups. Step *3* shows that some diamine groups can link two nanotubes by having the same reaction as shown in step *2*. (R = $(CH_2)_3NH(CH_2)_3NH(CH_2)_3$)

Treating nanotubes with aggressive reagents the phenolic and the carboxylic acid groups can be readily derivatized on the end caps or sidewall of nanotubes [30, 61, 98, 103]. The carboxylic acid groups can be converted into acylchloride groups by treating with thionylchloride [27, 98]. The acid chloride-functionalized carbon nanotubes are then susceptible to react with amines. The resulting chemically functionalized nanotubes are shown to be able to form a closed ring shape [136], or be attached to a normal Si AFM tip used for a single molecular sensor or probe [157]. On the other hand, the perfect carbon network lacks for sites where the functional groups can be attached. Although some natural defects such as

pentagon-heptagon pairs can be generated on the sidewalls during the growing process, they are maybe too low to achieve our goal. An alternative way to controllably introduce defects onto the nanotube walls is by acid treatment. For example, HNO_3 is a good oxidative acid which can be used to remove the catalyst particles capped at the ends of nanotubes and introduce defects onto the sidewalls. Defects in SWNTs are important in this process because they can serve as anchor groups for further functionalization.
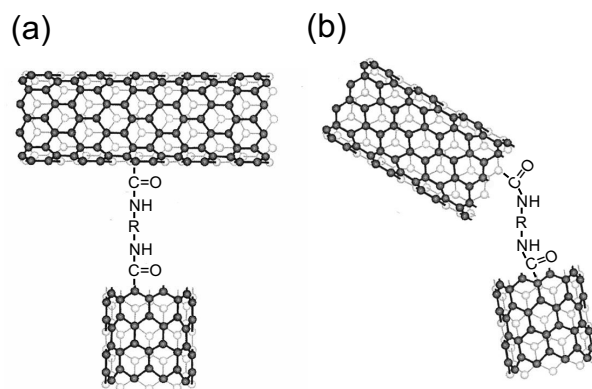
Figure 5.2: Functionalized nanotubes can be connected by single molecular linker in (a) end-to-side configuration and (b) end-to-end configuration. (R = $(CH_2)_3NH(CH_2)_3NH(CH_2)_3$)

Figure 5.1 shows the chemical functionalization of carbon nanotubes in different stages. SWNTs produced by the laser ablation method were obtained from Tube@Rice (Rice University) and Universität Karlsruhe (TH). These nanotubes were filtered and rinsed with pure water to remove the surfactant. The tubes were subsequently sonicated in HNO_3 for 20 minutes. This treatment is known to produce shortened and open-ended nanotubes and also create defects on sidewalls, both of which are capable of being terminated by oxygen-containing groups (mainly carboxyl and hydroxyl) in the presence of an oxidizing acid. Subsequently, we converted these groups to the corresponding acid chloride by reacting with $SOCl_2$ at room temperature for 24 hours. The brown-colored solution was decanted and the resulting solid material was rinsed with toluene followed by immersion in tripropylentetramin (TPTA) or phenylendiamine (PDA). The bifunctionalized amine interconnects two nanotubes via formation of acidic amide bonding [32]. Figure 5.2 shows the schematic representations of the two types of heterojunctions. In this process, SWNTs become gradually soluble in the TPTA

or PDA solution, indicative of the successful functionalization of the SWNTs. After reaction, the SWNTs were intensively rinsed with acetone and pure water, respectively. The amide functionalized SWNTs are insoluble in water and acetone. The suspension in surfactant solution (e.g. sodium dodecyl sulfate) cannot stand for a prolonged period of time and will precipitate in minutes, which is in sharp contrast to the untreated SWNTs.

5.3 Characterization of functionalized nanotubes

5.3.1 Atomic force microscopy

After chemical functionalization, most of the nanotubes form a network and connect side by side. To untangle the network appropriate ultrasonic agitation is applied to nanotube SDS suspension. This is a crucial step since we have to break part of the linkage, but also retain part of it. Figure 5.3 shows an AFM image of carbon nanotubes functionalized with TPTA. From the AFM inspection it is difficult to distinguish whether the crossing of nanotubes are linked by molecules or just form by accident. We can count only on the nanotubes which make end-to-end or end-to-side connections and show the statistic evaluation in the inset to Figure 5.3. In most cases, the nanotubes form end-to-side junctions. End-to-end junctions are rarely found. Under an appropriate ultrasonic agitation, around one third of the nanotubes form end-to-side junctions, whereas less than 2% of the pristine nanotubes show similar junctions, as mainly splitting bundles were observed.

In Figure 5.4 we show these junctions in higher magnification in AFM images. A dendrite-like end-to-side interconnection is shown in Figure 5.4 (a) for a 4 mm-long nanotube host with a diameter of 1.8 nm. The junctions are indicated by arrows. The three interconnected nanotubes have diameters of 1.3 nm, 1.6 nm and 1.2 nm (from top to bottom), respectively. Figure 5.4 (b) shows both the end-to-end and end-to-side interconnections. A ring-shaped nanotube closure can also be observed at the bottom of the image. The interconnected structures can sometimes be observed in the case of splitting bundles (Figure 5.4 (d)), where nanotube divergence occurs at various angles. This angle is generally smaller than that at the junction of two individual tubes/bundles connected by molecular linkers. It is important to note that the host tube often shows a shrunken diameter
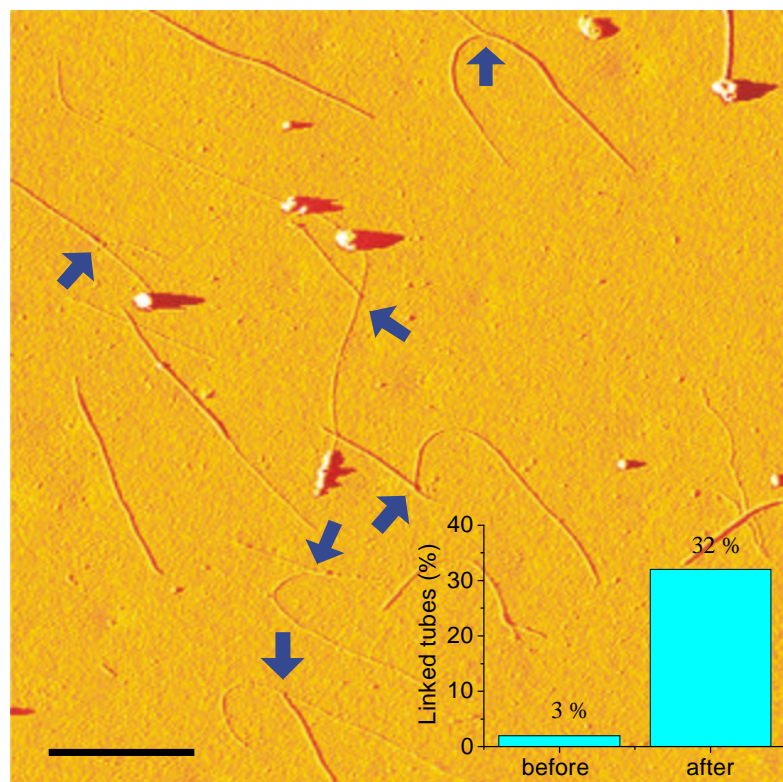
Figure 5.3: AFM images of carbon nanotube interjunctions. The junction position is indicated by arrows. The inset shows the statistical evaluation of linked nanotubes (end-to-end and end-to-side) before and after functionalization. The scale bar is 1 μm.
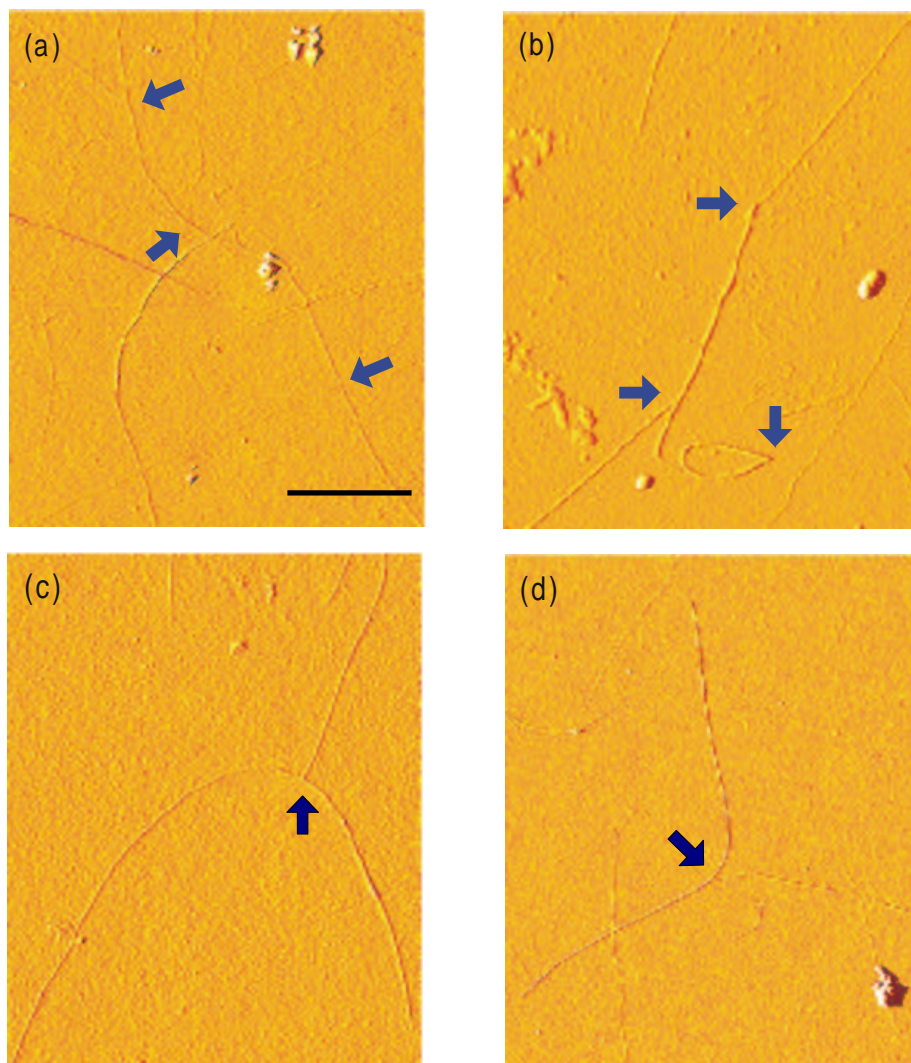
Figure 5.4: AFM images of carbon nanotube interjunctions. (a)The dendrite-like end-to-side junctions formed by three tubes attached on a 4 mm-long host tube (appearing lengthwise on the image). (b) Both end-to-side and end-to-end junctions with attached tubes of three different diameters. Tube closure can also be observed indicated by the bottom arrow. (c) A single carbon nanotube interjunction. (d) A splitting bundle of carbon nanotubes. The scale bar is 400 nm through (a) to (d).

after splitting. As indicated by the arrow in Figure 5.4 (c), the intersection of the two nanotubes via molecular linkage is almost perpendicular. The diameter of the host nanotube also remains unchanged in the AFM height profile.

5.3.2   X-ray photoelectron spectroscopy

X-ray photoelectron spectroscopy has emerged as a powerful tool to provide surface information of solids, on which the core-level electrons are excited by external photons and measured by an electron spectrometer. These energies are well-known for free atoms. In molecular or solid compounds, the energy of a bonded electron in a specific element is subjected to a shift which conveys information about the chemical environment of the atoms under investigation. Therefore, XPS provides not only a way to inspect the chemical reaction on SWNTs but also indicates the changes of electronic structure in SWNTs.

Figure 5.5 (a) shows the N 1s spectra of the various functionalized nanotubes. In pristine nanotubes a weak peak shows at 400.0 eV. This is speculatively due to NO_2 groups which intercalate into the triangular lattice structure of nanotube bundles. This small amount of nitrogen can be introduced by the well-known electrophilic action of HNO_3 on an aromatic system during the purification process. In both CNT-PDA and CNT-TPTA, there are clearly two components in the N 1s core level spectra. These two different binding energies are assigned to the two different nitrogens in PDA and TPTA, respectively. These XPS spectra confirm that the diaminol functionalities have been attached on SWNTs after a set of chemical reactions described above.

If we look into the C 1s core level spectra shown in Figure 5.5 (b), the functionalization induced changes in electronic structure of nanotubes are evident. In pristine nanotubes, the peak at 284.4 eV is assigned to the C 1s binding energy for the SWNTs, representing the elemental sp^2 carbon atom; it has the same shape and position as the C 1s peak in graphite. The small amount of nitrogen shown in Figure 5.5 (a) N 1s spectra for pristine nanotubes has a minor effect on the doping state. However, upon chemical functionalization, the peak position varies. In CNT-Cl a p-type doping effect downshifts the peak from 284.4 eV to 284 eV, while in CNT-PDA and CNT-TPTA the n-type doping effect upshifts it back to 284.4 eV and even up to 284.9 eV, respectively.
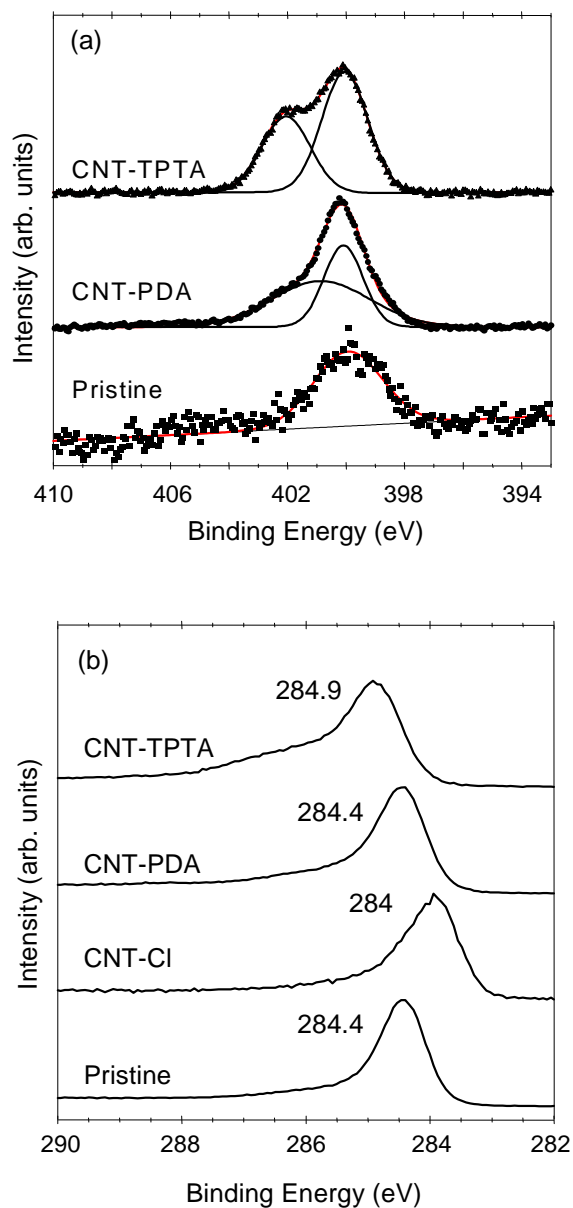
Figure 5.5: (a) N 1s core levels of pristine carbon nanotubes and diamine functionalized carbon nanotubes. (b) C 1s core levels of carbon nanotubes in different functionalization stages.

5.3.3   Raman spectroscopy

Due to the strong coupling between electrons and phonons in the 1D system, Raman spectroscopy provides a valuable tool not only for examining the vibration modes of SWNTs with specific diameter but also structural dependent electronic band structures. It is shown by experiments and theories that Raman scattering by SWNTs exhibits unusual resonant behavior. The scattering intensity is found to be enlarged by several orders of magnitude when the energy of the incident or the scattered photon matches the energy of allowed optical transitions between van Hove singularity pairs in the electronic density of states. The energy of allowed optical transition is dependent on whether the tube is metallic or semiconducting, and scales with the diameter of nanotubes. As a consequence, even though the nanotube sample always contains different (n, m) nanotubes, the Raman spectrum at a given excitation energy mainly shows response to those that are in resonance.

The special symmetry properties of carbon nanotubes lead to only a few Raman-active vibrational modes: $A_1, E_1,$ and E_2. In general, a first order Raman spectrum of carbon nanotubes shows three significant regions: a dominant spectrum between $150-200$ cm^{-1} by radial breathing mode (e.g. A_{1g} symmetry in armchair nanotubes); around 1350 cm^{-1} (D-line), and the G-band between $1550-1600$ cm^{-1} related to the tangential C$-$C stretching modes of graphite (e.g. A_{1g}, E_{1g} and E_{2g} symmetry in armchair nanotubes). In the radial breathing mode (RBM), the carbon atoms undergo a uniform radial in-phase motion which is unique in carbon nanotubes. Both theoretical [79, 92, 133, 135] and experimental [12] studies have confirmed that the mode frequency ω_{RBM} shifts as a function of the carbon nanotube radius and is weakly dependent on the tube chirality. This is consistent with the fact that the energy gap of a semiconducting nanotube and the strain energy is determined primarily by the nanotube radius. Due to the 1D quantum confinement, the resonant Raman enhancement effect takes place when the incident or scattered photon energy matches the electronic transition between the van Hove singularities in the 1D density of states in the valence and conduction bands of the nanotubes [2, 41, 122]. The first transition energy can be expressed as $E_{11}^{sc}(d_t) \simeq 2\gamma_0 a_{c-c}/d_t$ for semiconducting nanotubes and $E_{11}^{m}(d_t) \simeq 6\gamma_0 a_{c-c}/d_t$ for metallic nanotubes. Coupled with this resonant enhancement effect in Raman scattering, the mode frequency ω_{RBM} is very sensitive to the changes in nanotube diameter and tube-tube interaction, which makes

RBM mode a valuable probe for the functionalization-induced structural and electronic changes in carbon nanotubes [12]. The D-line around 1350 cm^{-1} is due to the disordered carbon and usually assigned to defects in carbon nanotubes or to the presence of carbon impurities [23]. It can be therefore used for classifying the purity of carbon nanotube samples. Another feature in the Raman spectra of SWNTs in the range 1550−1600 cm^{-1} is identified with the tangential stretching modes (TM). In contrast to the low frequency RBM mode near 200 cm^{-1}, the vibrational modes in G band are insensitive to the changes of nanotube diameter [122, 132].

Due to these unique features induced by resonant process, Raman spectroscopy has become one of the most efficient tools for investigating the vibrational properties of SWNTs in relation to their structural and electronic properties. Since Raman vibrational features are sensitive to both the intercalation and charge transfer, this spectroscopy allows us to investigate the evolution of the structural and electronic properties of SWNTs under chemical functionalization [34, 91].

Shown in Figure 5.6 is the progressive change of Raman spectra, over a broad frequency range from 50−2000 cm^{-1}, excited by a laser energy of 1.92 eV from a SWNT sample in different functionalization stages. Distinct features can be seen in the Raman spectrum of CNT-Cl. The intensity of RBM bunch and D-line are relatively suppressed compared to that intensity in pristine nanotubes; the TM bunch has become narrower in the spectrum of CNT-Cl, and the center of the band has upshifted by ∼10 cm^{-1}. After reacting CNT-Cl with TPTA and PDA, we can see a tendency towards the relative intensity of RBM and D-line being recovered, and the TM bunch shows a similar peak structure to that of pristine nanotubes.

The changes of RBM bunch between 100−300 cm^{-1} and of TM bunch between 1400−1700 cm^{-1} for laser excitation energy 2.54 eV and 1.92 eV are emphasized in Figure 5.7 and Figure 5.8, respectively. In Figure 5.7 only semiconducting nanotubes with specific $E_{ii}^{sc}(d_t)$ are in resonance with either the incident or scattered photon, showing two dominant peaks in tangential mode. All of the spectra in tangential mode for different functionalization stages can be well described by three characteristic Lorentzian components, as shown in the curve fitting in Figure (e) ∼ (h). The higher two frequency components are associated with vibrations along the circumferential direction, and the lower frequency component is attributed to vibrations along the direction of the nanotube axis. TM is hence sensitive to the charge transfer in carbon nanotubes and provides a valu-
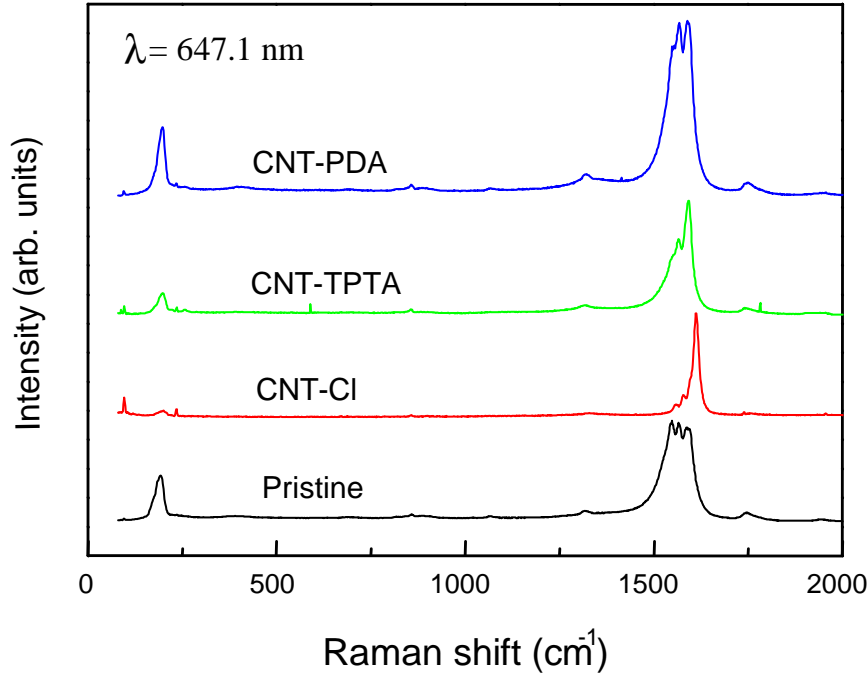
Figure 5.6: Raman spectra of pristine and functionalized SWNTs. The spectra were taken with excitation energy λ = 647.1 nm (E = 1.92 eV).

able probe of the electronic structure through the coupling between electrons and phonons. Compared with the pristine nanotube sample and CNT-Cl, there is a clear peak shift in the high frequency component of TM from 1584 cm^{-1} to 1601 cm^{-1}. In both CNT-TPTA and CNT-PDA, this peak downshifts to 1591 cm^{-1} and 1589 cm^{-1}, respectively. The softening in the TM can be interpreted in terms of valence electron transfer from an electron donor [123, 124], the amine group, into the carbon π* band, resembling graphite intercalation compounds. On the contrary, stiffening of the TM was observed upon doping with electron acceptors. These results are in good agreement with the characterization by XPS.

Likewise, the RBM bunch in CNT-Cl upshifts from 171 cm^{-1} to 180 cm^{-1} and then goes back to 177 cm^{-1} for both CNT-TPTA and CNT-PDA. The RBM is a strong A_1 mode sensitive to the nanotube diameter d_t as:

$$\omega_{RBM} = \Delta\omega_{RBM} + C/d_t \tag{5.1}$$

where $\Delta\omega_{RBM}$ is a frequency shift due to tube-tube interactions, C is a constant and expressed as the radial breathing mode frequency of an isolated nanotube times its diameter [2, 150]. The upshift of RBM suggests a stronger tube-tube interaction in a nanotube bundle due to lattice contraction upon hole doping [151].

Similar evolution of Raman spectra upon functionalization is shown in Figure 5.8. At $E_{laser} = 1.92$ eV the spectra show that both semiconducting and metallic nanotubes are brought into resonant Raman process involving interband transitions between singularities in the 1D electronic density of states. This indicates that we have a broad distribution of nanotube diameters. The nanotubes can be in resonance with the $E_{33}^{sc}(d_t)$ transition for semiconducting nanotubes and with the $E_{11}^{m}(d_t)$ transition for metallic nanotubes [22]. The tangential phonon mode region in pristine nanotubes yields Lorentzian components at 1567 cm^{-1}, 1591 cm^{-1} and 1601 cm^{-1} for semiconducting nanotubes. Three additional characteristic components resulting from metallic nanotubes are present at 1529 cm^{-1}, 1550 cm^{-1} and 1581 cm^{-1}, respectively. Focused on TM bunch, we can observe an evolution upon chemical functionalization. In CNT-Cl, the TM bunch upshifts to a higher frequency due to the p-type doping, consistent with the upshift of TM bunch at 2.54 eV excitation and downshift of carbon binding energy in C 1s core level spectrum. Reacting CNT-Cl with TPTA or PDA recovers the phase and the peak positions of TM bunch. Most interestingly, the TM profile in CNT-Cl loses the low-frequency components and is now dominated by a semiconducting component at 1612 cm^{-1}. In CNT-Cl, the electron acceptors empty the uppermost states of the valance band, therefore, the Fermi level is shifted down below the first 1D van Hove singularities in the density of states. The first few optical transitions between singularities are quenched due to the lack of appropriate electron/hole states. This results in a loss of Raman resonance which manifests as a decrease in the intensity of the corresponding peak in the spectrum [17, 41, 81]. In CNT-TPTA, the electron donors refill the uppermost states of the valance band. The TM bunch then shifts back to the same frequency as the pristine sample. This recovery is more clearly seen in the spectrum of CNT-PDA. The TM spectra of both CNT-TPTA and CNT-PDA can be well fitted by the same Lorentzian oscillators used in the spectrum of the pristine sample. In both cases, the peaks at 1591 cm^{-1} and 1550 cm^{-1} are still the dominant components in semiconducting nanotubes and metallic nanotubes, respectively.

The RBM bunch at $E_{laser} = 1.92$ eV shows a similar evolution and is depicted

in Figure 5.7. The RBM bunch first upshifts from 193 cm^{-1} to 201 cm^{-1} and then shifts back to 198 cm^{-1} in both CNT-TPTA and CNT-PDA. This functionalization induced RBM shift resembles the RBM shift in alkali metal doped nanotubes [17]. Since the frequency of RBM is very sensitive to the intertube interaction, the shift of the RBM is expected upon interaction of doping species inside the bundles [121]. Under this assumption, the upshift of the RBM could be assigned to a stiffening of the intertube interaction due to lattice contraction under hole doping. Additionally, the ratio of TM to RBM integrated intensity also varies with functionalization. In the pristine nanotubes the ratio is about 2.3 and drastically increases to 18.5 upon hole doping in CNT-Cl. It recovers to 5.8 in CNT-TPTA and 2.7 in CNT-PDA, respectively. Therefore, this ratio could be useful in controlling the amount of doping in the sample.
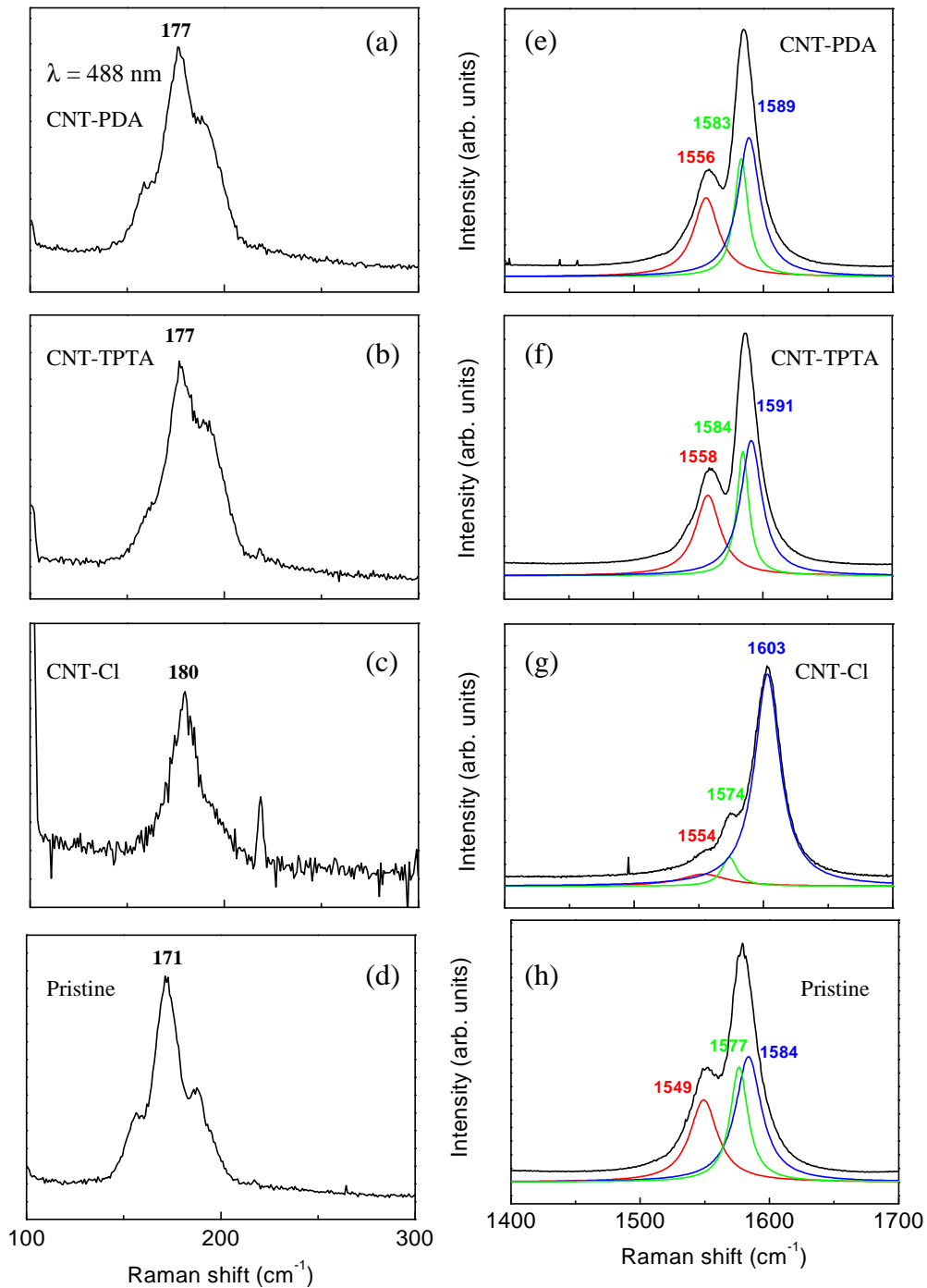
Figure 5.7: Radial breathing mode (RBM)((a)~(d)) and G-band ((e)~(h)) Raman response of pristine and functionalized SWNTs. The spectra were taken with excitation energy $\lambda = 488$ (E = 2.54 eV). Lorentzian fits to G band are shown.
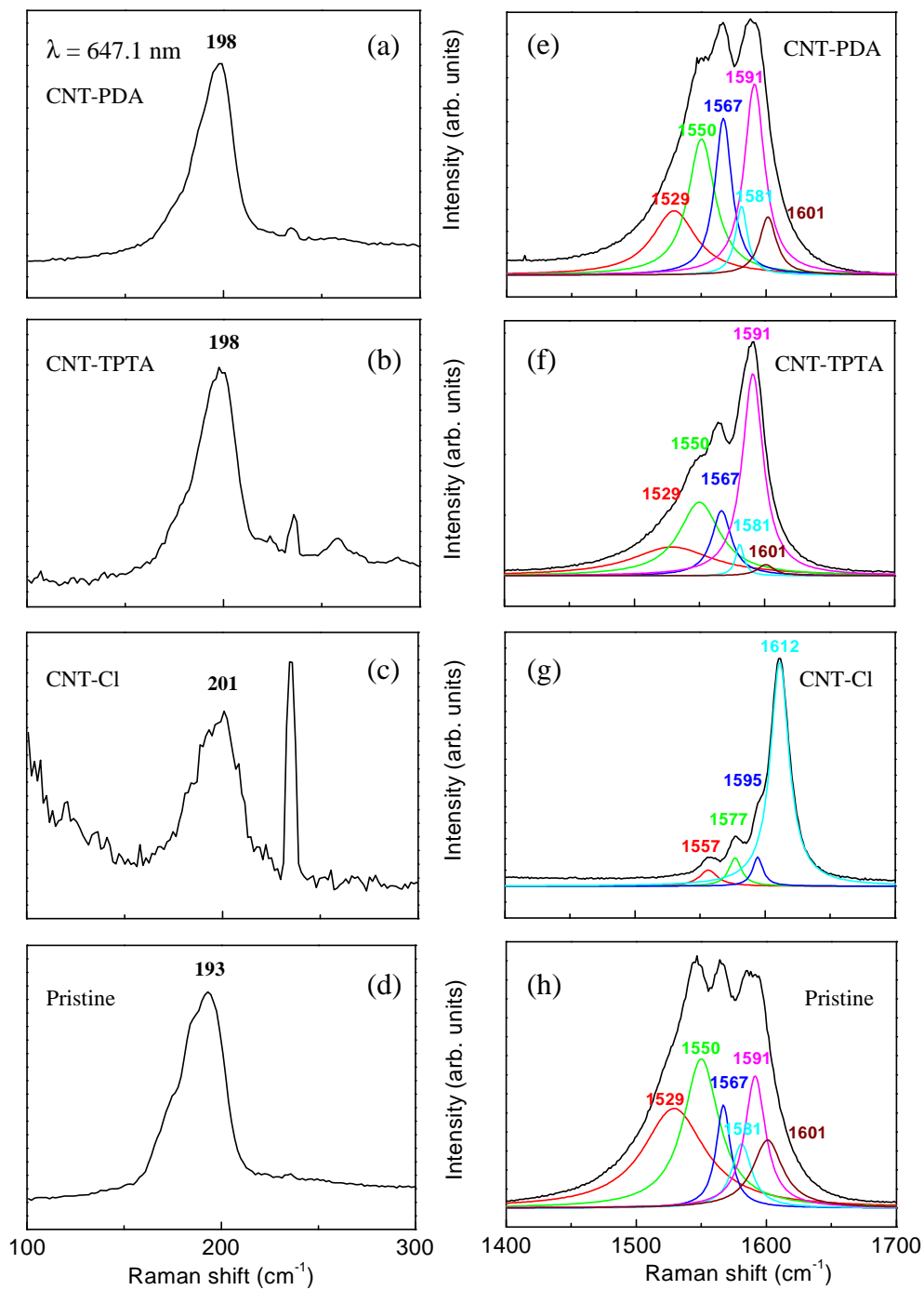
Figure 5.8: Radial breathing mode (RBM)((a)~(d)) and G-band ((e)~(h)) Raman response of pristine and functionalized SWNTs. The spectra were taken with excitation energy $\lambda = 647.1$ nm (E = 1.92 eV). Lorentzian fits to G band are shown.

Chapter 6

All-carbon nanotube transistors

6.1   Introduction

Since Iijima's discovery [73] of carbon nanotubes during his electron microscope studies in 1991 more than 6500 papers on these new materials have appeared so far. Several groups have prepared transistors based on carbon nanotubes (field-effect transistors [101, 102, 148, 164] or single-electron transistors [19, 120, 147]). The first generation of these transistors consisted of nanotubes placed over metal leads on a silicon chip. The leads served as source and drain and the doped silicon substrate acted as a gate. The on/off ratio of these transistors was about 10^5, but the gain was very low ($<<1$), due to the fairly thick oxide layer needed to prevent leakage currents. Recently Bachtold *et al.* presented a new electrode configuration where the gate is an aluminium strip and the thin aluminium oxide layer allows the gate to be so close to the nanotube that the transistor reaches gain values of about 10 [9]. Several papers reported on combining nanotube transistors to logical circuits [9, 38, 76] and Dai *et al.* [76] have presented an array of some hundred nanotube transistors assembled on a silicon chip. The nanotube transistors reported so far are not really "nanoscale" devices. The conducting channel consists of a single nanotube and this is, of course, nanoscale. But source and drain are made by electron beam lithography, and are about 100 nanometers wide and several micrometers long. In the first generation nanotube transistors the gate is even macroscopic (a silicon chip of millimeter size). The aluminium gate of the second generation transistors (Bachtold *et al.*) is lithographic like source and drain and still not nanoscale. In this chapter we report on transistors where not only the conducting channel is a nanotube, but the gate is also a carbon

nanotube. The role of the gate oxide is played by a tripropylentetramin molecule, linking the two tubes to form carbon nanotube T-junctions (CNTJs). Thus the active part of the device is truly confined to a region of a few nanometers in all three dimensions and it is all-carbon, except for four nitrogen and two oxygen atoms!

In addition to the transistor behaviors, we have also explored the band structure modulation in metallic nanotube channels via the carbon gate. For doing this, we have made two distinct junctions: CNTJ-I with bridging linker molecules at the junction; CNTJ-II without bridging linker molecules at the junction. The modulation mechanisms are discussed in terms of the "field effect" along with the "electromechanical effect".

6.2   Device processing

In the previous chapter we dealt with the chemical functionalization of nanotubes, by which two nanotubes can be brought into connection in a T-shape configuration. Following the procedure of nanotube dispersion in SDS solution and adsorption on silanized Si substrate we can contact these delicate structures by electron-beam lithography. During the dispersion of functionalized nanotubes by ultrasonic agitation special care must be taken to maintain the interconnection of nanotubes by single molecules. A rather sparse density of nanotubes is adsorbed on Si substrate with predefined coordinate markers, as shown in the AFM images in Figure 6.1 (a). A well-shaped junction was carefully checked with AFM and selected for metal contacts (Figure 6.1 (b)). The position of the junction is calculated relative to the closest four coordinate markers. Subsequently, Cr/AuPd were applied by the electron-beam lithography process described in Chapter 2. As can be seen in Figure 6.1 (c), the lithographical processing did not ruin the junction structure.

6.3   Electrical transport

Figure 6.2 (a) and (b) show the AFM images of the CNTJ-I samples with semiconducting and metallic nanotubes as conducting channels, respectively. The two nanotubes are bridged by tripropylentetramin to form the junction, which is ∼1.4 nm long and nonconductive. Due to the insufficient resolution of the AFM the
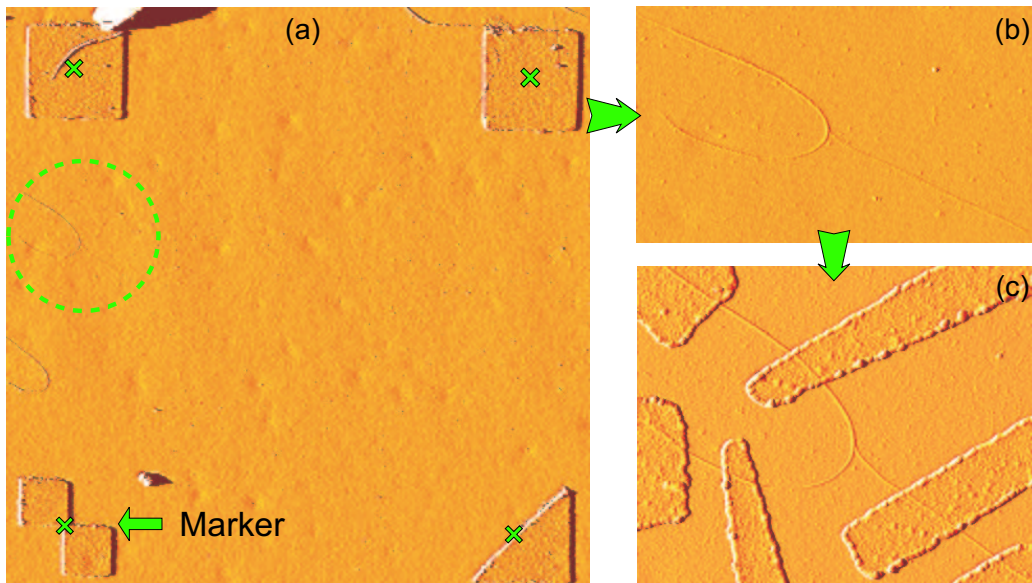
Figure 6.1: Procedure for making contacts on a CNTJ. (a) AFM image of functionalized nanotubes on Si substrate with marker system. (b) Zoomed AFM image in the marked region in (a). (c) Six metal leads are attached on top of the selected CNTJ.

diamide linker molecule at the junction is not resolvable in images. The long molecular chain and perpendicular linkage keep the nanotubes in proximity without allowing contact. In this configuration the molecular linker can function as insulating gate oxide, resembling the SiO_2 in metal-oxide-semiconductor FETs. The nanotubes are embedded in five 20 nm thick Cr/AuPd electrodes. The bar of the "T" is the tube between the leads E1 and E2, and acts as conducting channel, and the leg connected to E4 is the "carbon gate". E3 and E5 are additional contacts to allow for separate inspection of the two nanotubes forming the T-junction. The Si chip is degenerately doped so as to act as a common "back gate" to characterize the electric properties of the various sections of the tubes.

6.3.1 Transistor behavior in semiconducting nanotubes

As is well known, there are semiconducting and metallic carbon nanotubes, and it is not yet possible to synthesize only one type or to separate the types after
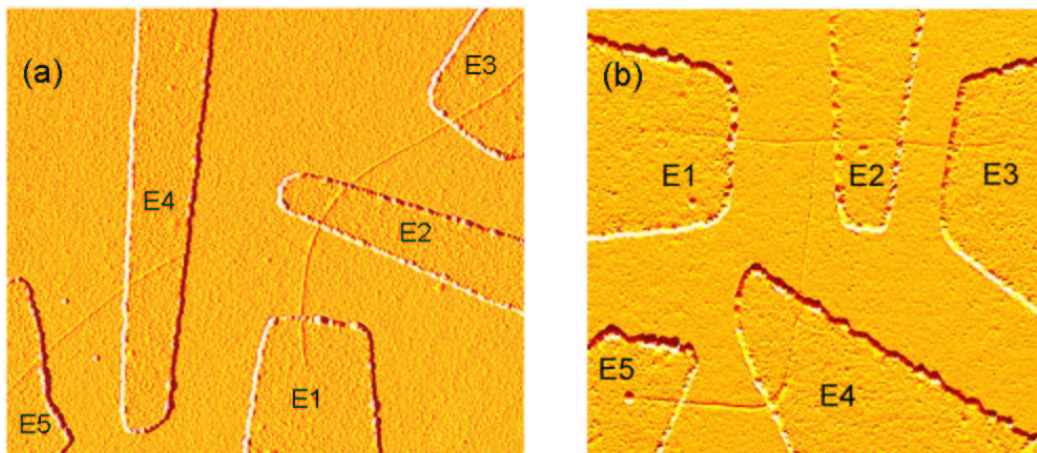
Figure 6.2: AFM images of two CNTJ-I samples with electrodes applied on top. (a) The bar and the leg of the T have diameters of 2.0 nm and 1.4 nm, respectively. For (b) they are 1.0 nm and 2.8 nm, respectively. The shortest distance between the electrode (E2) and the junction point is ∼150 nm in (a) and ∼70 nm in (b), respectively.
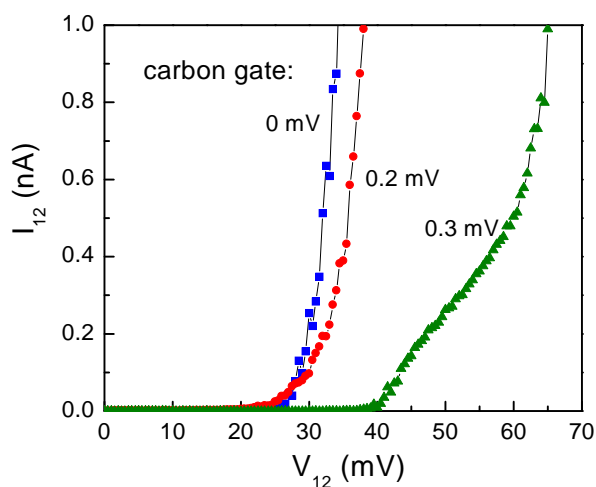
Figure 6.3: Current vs. voltage characteristics of an all-carbon transistor with semiconducting nanotube as channel, with different voltages at the carbon gate. The back gate is kept at 0 V. The measurements were carried out at 4 K.

synthesis. The conduction properties of the nanotubes can be characterized by observing the response to the back gate. If the conductance can be modulated by several orders of magnitude, the tubes are semiconducting, otherwise metallic. The obvious configuration for a "field-effect" transistor would be to choose a semiconducting tube as channel. The device shown in Figure 6.2 (a) is this case, whose output characteristics are depicted in Figure 6.3 (channel current versus bias across channel for different carbon gate voltages V_{cg}). At a bias of 35 mV between source and drain we can pass a current of 1 nA through the channel tube. If we apply a carbon gate voltage of 0.3 mV to the tube forming the leg of the "T", we can effectively suppress this current. Thus we see that gain values (defined as $g = \frac{\Delta V_{ds}}{\Delta V_{cg}}|_I$) of about 100 can easily be obtained in all-carbon transistors.

6.3.2   Band gap modulation in metallic nanotubes

The electronic structure of carbon nanotubes is crucially dependent on their diameter and chirality. The existence of different chiralities gives both metallic and semiconducting nanotubes [113, 155]. Recent predictions have pointed out that mechanical deformation [67, 80, 93, 100, 128, 161] and a high electrostatic field [55, 56, 84] can remarkably affect a tube's electronic properties and could be used for band gap engineering in nanotube-based molecular scale electronics. Previous experiments have focused on strain-induced conductance changes mainly based on scanning probe technique where the loading is applied by an AFM tip on a suspending nanotube [26, 110, 149]. Stress is exerted throughout the tube and causes different deformation modes: bending in the tip-contacted region and stretching along the axial direction in the straight parts. It was found in these experiments that the conductance could drop by a factor of two [26, 110] or even by two orders of magnitude [149] in metallic nanotubes under various strains.

Here we present measurements to demonstrate for the first time that the band structure of metallic nanotubes can also be modulated by a local electrostatic field. Both metallic (on) and insulating (off) states are accessible by changing the field strength, resembling a molecular switch.

To date, CNTJs are only predicted by theories [107, 108] where the leg of the T is attached sidewise to the bar of the T via pentagon and heptagon carbon rings. CNTJs used in the this study are somewhat different and were fabricated by functionalizing nanotubes on the defect sites. The carbon gate is capacitively coupled to the channel via an insulating molecule bridging the two tubes. An

example of such devices is shown in Figure 6.2 (b), where the bar of the T is metallic. The tube between E1 and E2 is defined as the conducting channel and the tube between E2 and E3 is used only for diagnostic purposes. A dual gate configuration is designed in our devices: the Si chip acts as a back gate, and the leg of the T is used as an in-plane carbon gate. To gain insight into the modulation mechanisms, we have investigated the electrical transport along two different kinds of CNTJs. The first type (CNTJ-I) was made as described above, whereas the bridging molecule was destroyed by heat treatment in the second type (CNTJ-II).

Shown in Figure 6.4 is the conductance of a metallic channel in CNTJ-I as a function of the back gate voltage V_{bg} at 4 K. The panels (a), (b), and (c) correspond to different fields applied through the carbon gate. The bias across the channel is kept constant at 6 mV and the channel current I_{12} is measured. At $E_{cg} = 0$ (Figure 6.4 (a)), regular conductance oscillations are seen in the $dI_{12}/dV_{ds} - V_{bg}$ plot. They originate from the quantum confinement on the metallic channel by the two contact barriers. These conductance peaks appear when a new quantized excitation becomes energetically accessible, opening a tunnelling pathway between the confined nanotube and the electrodes. The peak spacing is constant, implying that a single quantum dot is defined between the two confining electrodes.

Applying a field strength of 4×10^3 V/cm on the carbon gate (Figure 6.4 (b)) dramatically distorts the Coulomb blockade (CB) oscillations. A new oscillation pattern, shown in Figure 6.4 (b) and its inset, emerges with average peak spacing broadening from $\Delta V_{bg} = 40$ mV to $\Delta V'_{bg} = 140$ mV. The increasing peak spacing and the irregular amplitude indicate that the electric field acts as a local perturbation to the 1D quantum structure. The channel is energetically split into two islands and connected in series with length . This change can be confirmed from $\Delta V'_{bg}/\Delta V_{bg}$ obtained from the self-capacitance of the split channel. ΔV_{bg} corresponds to a change of one electron in the island and can be expressed as $e\Delta V_{bg} = (E_{n+1} - E_n)C_\Sigma/C_{bg} + e^2/C_{bg}$, where C_{bg} is the gate capacitance and C_Σ is the total capacitance of the defined quantum dot. It is assumed that the energy spectrum for the greater split island can be regarded as continuous at 4 K [130]. In the approximation of vanishing energy splitting in the smaller island $E_{n+1} - E_n \approx 0$, we obtain $\Delta V'_{bg}/\Delta V_{bg} \approx C_{bg}/C'_{bg} = L \ln(2L_r/d_t)/L_r \ln(2L/d_t) = 3.8$ with $d_t = 1.0$ nm being the tube diameter and $L = L_r + L_l$ being the channel length. This is in good agreement with the observed ratio $\Delta V'_{bg}/\Delta V_{bg} = 3.5$ in
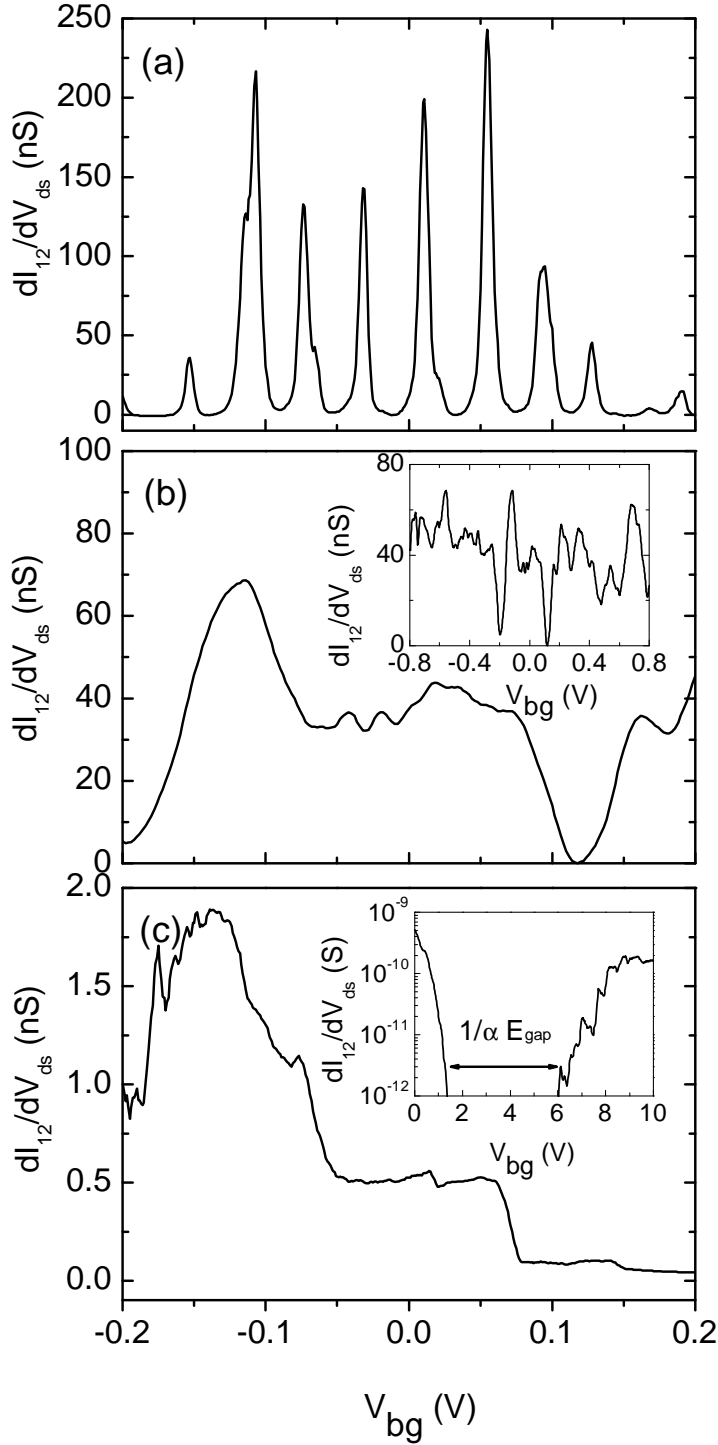
Figure 6.4: Evolution of back-gate dependent conductance in a metallic channel of CNTJ-I at 4K. The data were taken at $V_{ds} = 6$ mV with (a) $E_{cg} = 0$, (b) $E_{cg} = 4 \times 10^3$ V/cm, and (c) $E_{cg} = 10^4$ V/cm. Both insets to (b) and (c) show the conductance in extended voltage scale.

$dI_{12}/dV_{ds} - V_{bg}$ plot shown in Figure 6.4 (b) and its inset.

Interestingly, if we further increase E_{cg} to 10^4 V/cm, the CB oscillations vanish and a step-like conductance shows up in Figure 6.4 (c). The $dI_{12}/dV_{ds} - V_{bg}$ curve now shows ambipolar transport with hole conduction at $V_{bg} < 1.5$ V and electron conduction at $V_{bg} > 6$ V (inset to Figure 6.4 (c)). In contrast to $E_{cg} = 0$, here the channel conductance drops by two orders of magnitude in the conducting state. This change occurs only locally in the channel where the carbon gate is attached. The electrical transport in a diagnostic segment next to the channel is not affected upon application of the E_{cg}. This result shows that the increasing E_{cg} progressively modifies the electronic structure of the metallic tube locally. At $E_{cg} = 10^4$ V/cm, an energy gap E_g is induced in the metallic channel. The energy gap E_g can be estimated by multiplying a gate efficiency factor $\alpha \approx 10$ meV/V to the insulating region spanning $\Delta V_{bg} \sim 4.5$ V, yielding $E_g \sim 45$ meV.

In Figure 6.5 we show the $I - V_{ds}$ curves of CNTJ-I at $E_{cg} = 0$ (panel (a)) and at $E_{cg} = 10^4$ V/cm (panel (b) and (c)). The nonlinear $I_{12} - V_{ds}$ curve in panel (a) is due to the CB effect where the conductance gap corresponds to a charging energy of $E_c = e^2/2C_\Sigma \approx 20$ meV. In striking contrast, the $I_{12} - V_{ds}$ curve under $E_{cg} = 10^4$ V/cm is highly nonlinear and asymmetric, resembling that of a Schottky diode. The rectifying behavior as a signature for metal-semiconductor (M-S) junctions is explicitly associated with the gap opening. Additional transmission barriers develop at the M-S interfaces. This gives rise to a reduction of the turn-on voltage by two orders of magnitude at $V_{ds} > 0$, consistent with the conductance drop in the $dI_{12}/dV_{ds} - V_{bg}$ plot shown in Figure 6.4. These Schottky barriers are also reflected in the $I_{13} - V_{ds}$ curve shown in Figure 6.5 (c). Notably, the $I_{12} - V_{ds}$ curve under $E_{cg} = 10^4$ V/cm is very similar with that in nanotube M-S intrajunctions observed by Yao et al., where an asymmetric barrier is induced by a kink defect [159]. In our case the origin of the asymmetric barrier could be attributed to the asymmetric defect structure (e.g. pentagon-heptagon pair) which serves as an anchor group for linkage.

The mechanism(s) governing the gap opening observed in Figure 6.4 and Figure 6.5 is (are) presently unsettled. Different scenarios can be speculatively proposed to explain this effect. Being capacitively coupled to the channel, the carbon gate applies a local perturbation to the charge distribution in the vicinity of the junction by "field effect". At low field strength ($<< 3 \times 10^8$ V/cm), the field-induced polarization in metallic tubes is negligible but the electric field could cause the redistribution of the charge density in the valence and conduction band
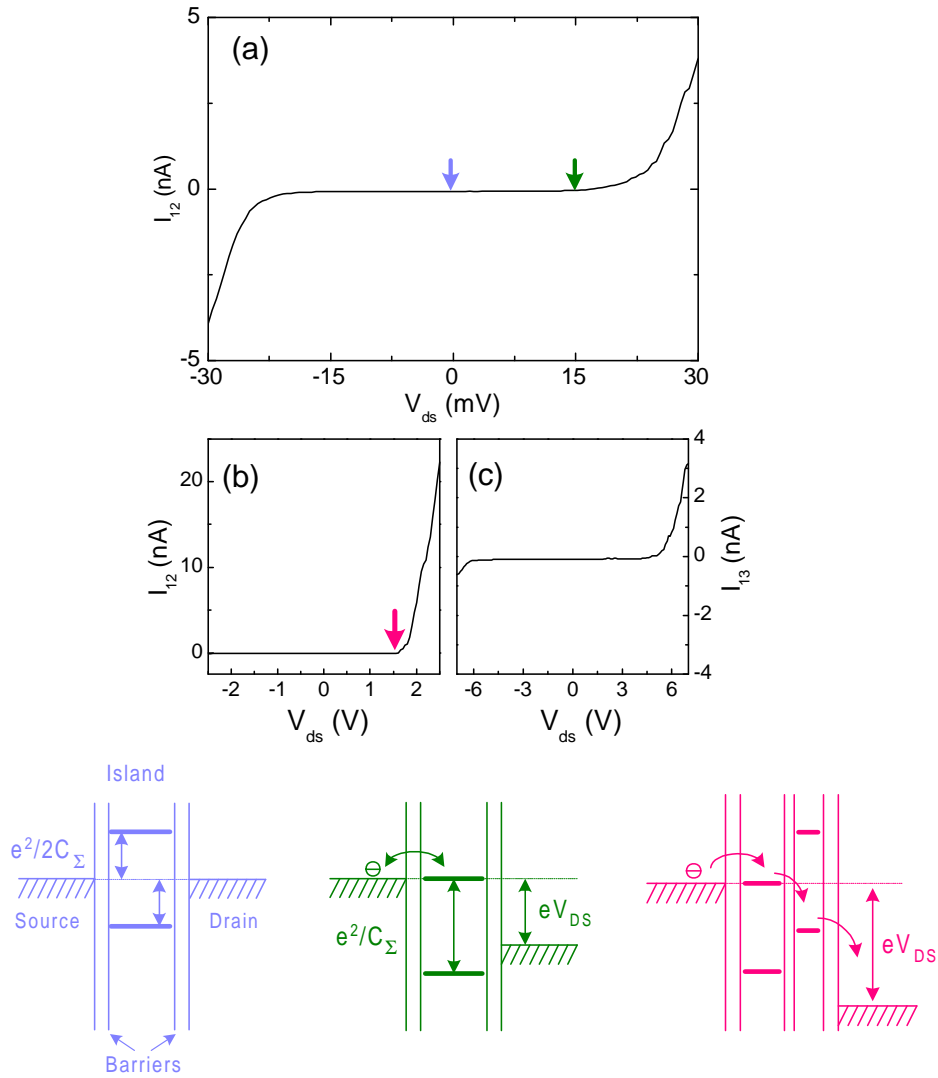
Figure 6.5: Output characteristics at $V_{bg} = 0$. (a) $I_{12} - V_{ds}$ curves at $E_{cg} = 0$. (b) $I_{12} - V_{ds}$ curves at $E_{cg} = 10^4$ V/cm. (c) $I_{13} - V_{ds}$ curves at $E_{cg} = 10^4$ V/cm. Energy level schemes corresponding to the state indicated by the arrows in (a) $\sim$ (c).

edges [56]. It was suggested for metallic nanotubes that a non-zero transmission barrier appears as the local electric field reaches the order of 10^7 V/cm and eventually results in a gap opening of tens of meV in the local density of electronic states for a higher electric field ($> 2 \times 10^7$ V/cm) [84]. However, this predicted electrical perturbation to the band structure is much higher than our experimental findings.

For a nanotube contacted only at one end by a metal lead, the application of the voltage on the tube will result in charge injection from the source. The extra charges accumulate considerably at the very end (within 3 Å) instead of being uniformly distributed along the tube [82]. This gives rise to substantial charge density at the tube end. Additionally, accumulating charges will enhance the local electric field, and are delicately influenced by the aspect ratio and the edge geometries [62]. The field enhancement factor can be simply estimated by using $\eta \sim m^2/\ln(2m) - 1$, where m is the aspect ratio of the tube, yielding a typical η value ranging from 10^2 to 10^3 in our carbon gates. If we take $\eta \sim 10^3$ into account, the field-effect induced band structure modulation will be in reasonable agreement with the experimental results. However, in accumulating the experimental statistics of CNTJ-I so far (~ 15 devices) we found two additional issues which remain uncertain: jerky-like conductance changes in most of the devices upon application of a similar order of E_{cg}; rather poor reversibility of the conductance changes in both metallic and semiconducting channels (i.e., the gating occurs only in one way, either $E_{cg} > 0$ or $E_{cg} < 0$).

We, therefore, come up with another mechanism which could contribute to the band structure modulation in CNTJ-I. The changes in the band structure can be understood from a consideration of the Fermi points in the reciprocal space of the graphitic lattice. In the 2D graphite layer, the first Brillouin zone is depicted by a hexagon with six Fermi points $\mathbf{k}_F$ lying on vertices $\mathbf{k}_v$. The electrical properties of nanotubes depend critically on the location of the graphitic Fermi points relative to the allowed 1D $\mathbf{k}$ lines (subbands). The value of $|\mathbf{k}_A - \mathbf{k}_F|$ characterizes the first van Hove singularities and energy gap [154], with $\mathbf{k}_A$ being the point of closest approach to $\mathbf{k}_F$ in any allowed lines. If one of these allowed lines passes through the $\mathbf{k}_v$ point of the 2D graphene Brillouin zone, the nanotubes are metallic and otherwise semiconducting. The mechanical forces of lattice expansion in the leg can exert on the circumference of the bar via the single molecular linkage. The sidewall of the bar could thus be twisted, giving rise to the change of local helicity near the junction. Prior to the twisting deformation, $\mathbf{k}_F$ of a metallic tube sits

on the allowed subband. Upon twisting, the wrapped graphite structure rotates, shifting $\mathbf{k}_F$ away from the original state. This gives rise to a nonzero shortest distance $|\mathbf{k}_A - \mathbf{k}_F|$, which is proportional to the induced energy gap at the Fermi surface of a metallic tube (see Appendix A for detailed analysis). In fact, similar actuation in V_2O_5 nanowires [54] and in individual nanotubes under visible light illumination [162] were also demonstrated. Thus, in our experiments the charged leg might pull against the bar and mechanically deform the bar in such a way that locally a gap is opened in the density of states and the metallic tube turns into a semiconductor.

To compare quantitatively the experimental results with theories based on the "electromechanical effect", we consider the model suggested by Yang *et al.* [161], in which the band gap under strain varies as

$$\frac{dE_g}{d\gamma} = \texttt{sign}(2q + 1)3\gamma_0 \sin 3\theta, \tag{6.1}$$

where $\gamma_0 \approx 2.7$ eV is the tight-binding overlap integral, θ is the chiral angle, $q = 0, \pm 1$ is the remainder in $n - m = 3p + q$ with (n, m) being nanotube indices and p being an integer. The strain transferred from the contraction of the carbon gate to the channel stems from the hole injection in the carbon gate and can be obtained from

$$\gamma \equiv \delta L/L = (\xi \pm 0.2q \cos 3\theta)f, \tag{6.2}$$

where $\xi = 0.07$ is a chirality-independent lattice displacement factor and upper/lower signs correspond to hole/electron doping [22]. The doping level in the tube can be written as

$$f = \frac{C_{cg}V_{cg}}{n_{cg}} \approx \frac{2\pi\epsilon L_{cg}V_{cg}}{n_{cg}\ln(2L_{cg}/d_t)}, \tag{6.3}$$

where ϵ is the dielectric constant, d_t is the tube diameter, L_{cg} is the length of carbon gate, n_{cg} is the number of carbon atoms within 3 Å [82]. It leads to $f \approx 2.4 \times 10^{-3}$ and corresponds to strain at the end of carbon gate, depending on the tube chiral angle. A gap ranging from 1.4 meV to 5.2 meV is then expected under such strain in the circumferential direction of the channel. This value is somewhat too small to be fully consistent with the experimental results, but it is sufficient to address the jerky-like conductance changes observed in most of the CNTJs with linker molecules.
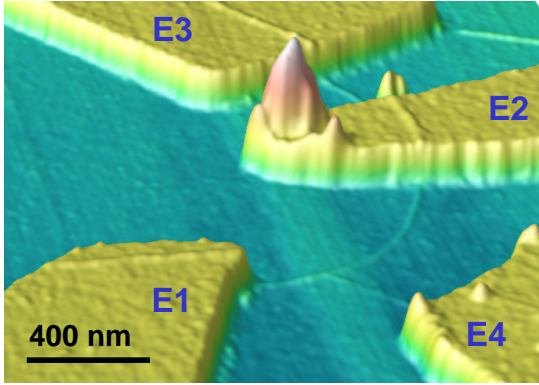
Figure 6.6: Three-dimensional AFM image of the CNTJ-II with electrodes applied on top. The diameter of the channel and the carbon gate are 1.6 nm and 1.3 nm, respectively.

To clearly separate the possible electromechanical effect from the field effect in CNTJ-I, we have produced a second type of T-junctions (CNTJ-II). In Figure 6.6 we show this type of nanotube T-junction with a metallic tube as bar. It is formed by using the same procedure of chemical functionalization shown in the previous chapter. The main difference is that the device is heat treated at 150 °C in air for 2 ∼ 3 minutes after contacting the T-junction with metal leads. The molecular linker, tripropylentetramin, can be effectively broken under this condition of heat treatment. This type of T-junction is useful in comparing the transistor behavior triggered by the speculated electromechanical actuation effect and the pure field effect. It can also be used to probe the local electrical properties of nanotubes by means of electrical field effects.

Figure 6.7 depicts the channel current versus back gate voltage at different field strength applied through carbon gate. We can see the current oscillation due to the CB effect at 4 K. It shows that the tube has stronger electrical coupling with leads when the negative back gate voltage is applied. As a E_{cg} is imposed on the metallic bar and the same back gate voltage is swept, a qualitatively similar CB structure (Figure 6.7 (a)) can be observed. In some regions of back gate voltage, we can clearly see the influence of a local carbon gate on the charge transport through the long quantum wire. This is magnified in Figure 6.7 (b) and (c). In Figure 6.7 (b), the peak at $E_{cg} = 0$ has Lorentzian shape, indicating the charge transport in linear regime. As a positive E_{cg} is applied, the peak downshifts and the peak amplitude decreases. On the other hand, the peak upshifts and a broadened peak shape develops when an opposite sign of E_{cg} is applied. In Figure 6.7 (c), we see that the E_{cg} only homogeneously shifts the potential of the right peak but significantly modifies the left peak in an unexpected way. These spectra are fully reproducible in trace and retrace measurements.

A more pronounced modification is depicted in Figure 6.8, where a carbon gate voltage up to ± 4000 mV is applied[1] and the V_{ds} is kept at the same value (60 mV). Sitting on a back gate voltage of $V_{bg} = -251$ mV (single electron tunnelling regime) the channel conductance first oscillates as a function of E_{cg}, and then drops to an immeasurable state ($<$ picoamp). This behavior is fully reversible in repeated measurement cycles. The conductance fluctuation could be due to the interference effect [78, 88, 96], in which the transmission coefficients for the two conducting subbands is additionally modified by the applied carbon gate. The transmission coefficients of the two electron waves in each subband can be approximately expressed as [78]

$$T_1 = 3/[(\varsigma/\gamma_0 + \sqrt{3}i)^2 - (\varsigma/\gamma_0)^2 e^{i2k_1 L}], \tag{6.4}$$

$$T_2 = 3/[(\varsigma/\gamma_0 + \sqrt{3}i)^2 - (\varsigma/\gamma_0)^2 e^{i2k_2 L}], \tag{6.5}$$

where ς is the energy barrier, and L is the channel length. Near the Fermi level, both wave vectors can be written as $k_1 = \Delta k_1 + 2\pi/3$ and $k_2 = \Delta k_2 - 2\pi/3$, where the $\Delta k_{1,2}$ can be obtained from the energy dispersion relation and be written as $\Delta k_1 = \Delta k_2 = (\alpha_{bg} V_{bg} + \alpha_{cg} V_{cg})/\hbar v_F$ with $v_F = \sqrt{3}\gamma_0/\hbar$ in the first-order approximation. α_{bg} and α_{cg} correspond to the gate efficiency factor for back gate and carbon gate, respectively. The phase term in the transmission coefficients are then rewritten as

$$e^{i2k_1 L} = e^{i[(2L/\hbar v_F)(\alpha_{bg} V_{bg} + \alpha_{cg} V_{cg}) + 4\pi L/3]}, \tag{6.6}$$

$$e^{i2k_2 L} = e^{i[(2L/\hbar v_F)(\alpha_{bg} V_{bg} + \alpha_{cg} V_{cg}) - 4\pi L/3]}. \tag{6.7}$$

As V_{bg} and V_{cg} vary, both T_1 and T_2 will oscillate and consequently the channel conductance will also fluctuate.

Beyond a field of $E_{cg} > 2 \times 10^7$ V/cm the metallic channel in the vicinity of the junction turns into an insulating state, in excellent agreement with the predicted value discussed above [84]. Interesting to note is that upon application of negative E_{cg} the field-effect modulation in the channel conductance is not symmetric to positive E_{cg}, a step-like conductance is observed instead (not shown).

---

[1]The leakage current between E2-E5 becomes sensible when the voltage across the junction is larger than $\pm$ 4.5 V.

Disregarding the edge geometry of the carbon gate and the induced enhancement of the electric field, a local field of over 10^7 V/cm is required for opening a gap in metallic tubes. In sharp contrast to CNTJ-I, we found that the conduction of metallic tubes in CNTJ-II can be reversibly switched by applied E_{cg} (pure field effect) and suggest that in addition to the "field effect" modulation the "electromechanical effect" could be attributed to the different switching mechanism observed in CNTJ-I.

In conclusion, we want to remark that the observed effects in CNTJ-I are reproducible from sample to sample, but the gate-induced changes are not very reversible (The lack of reversibility is consistent with the assumption of a jerky motion of the tubes as a compromise between actuator effect and attachment to the silanized substrate). In further experiments the samples have to be improved and theoretical modelling has to be extended. Due to the one-dimensional nature of carbon nanotubes, structural deformation on the perfectly curved honeycomb lattice shows remarkable influence on the charge transport. This plays an important role in designing the nanotube-based electronics [44, 57]. These geometrical changes are not restricted to carbon nanotubes but are a general feature of nanosize objects and have to be considered in designing any kind of nanoelectronics.
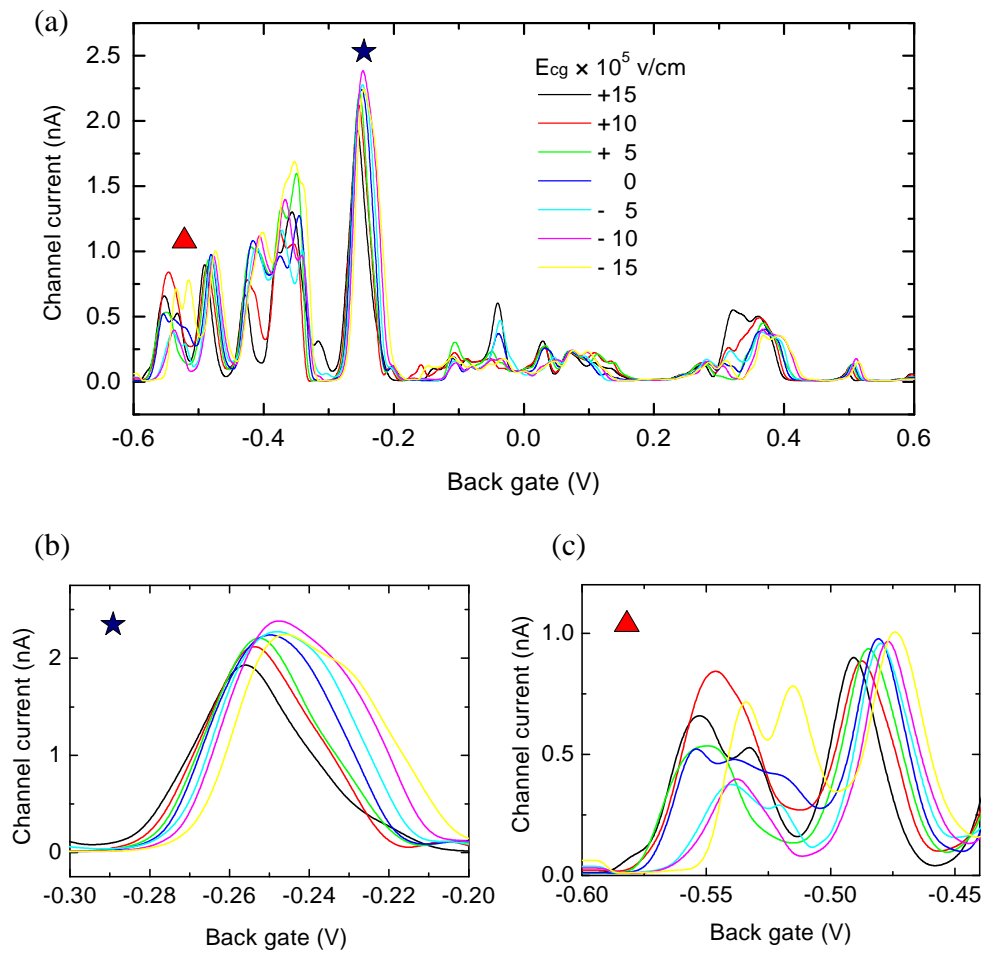
Figure 6.7: (a) Current (between E1−E2) versus back gate voltage of a metallic bar at different local electric field. (b) and (c) show the zoomed data in the marked regions.
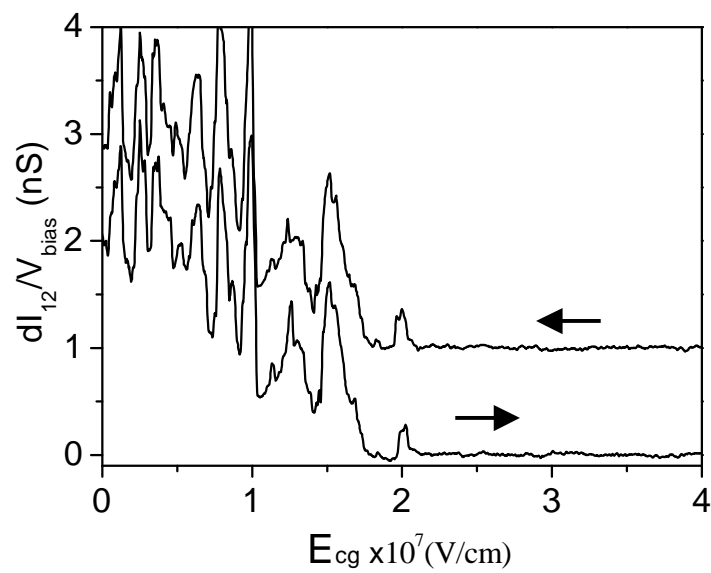
Figure 6.8: Conductance vs electrostatic field of CNTJ-II under V_{bg} = -251 mV. The data were recorded at 4 K. Two curves are shown: one with increasing field and another one with decreasing field. The latter case is offset by 1 nS for clarity.

Chapter 7

Summary and outlook

The extraordinary advances in silicon-based electronic technology has created smaller and smaller integrated circuits. This has led to higher operating speed and packing density. However, miniaturization is reaching its fundamental limits. One proposed and promising system is "molecular electronics" in which the active part of the device is composed of a single or a few molecules. One of the extensively studied materials is the carbon nanotube, a macromolecule with high aspect ratio in its geometry. They can be either metallic or semiconducting, depending on how they are rolled up. They are mechanically strong, chemically stable, and have well defined one-dimensional electronic structures (Chapter 1).

We have taken carbon nanotubes grown by laser-ablation and arc-discharge techniques for device processing, including suspension of nanotubes in an aqueous solution, dispersion of nanotubes on silicon substrate, and electron-beam lithography for fabricating electrical contacts. Two different contact methods have been involved in our device preparation: adsorbing an individual tube on top of the predefined electrodes; covering metal contact on top of selected tubes. The transport measurements are done in transistor configuration typically with three terminals, a special carbon gate is used as second gate in some transistors for locally tuning the electronic structures of the conducting channel. The experimental setup enables a consecutive change in temperature from room temperature down to liquid helium temperature (Chapter 2).

The unique electrical properties of SWNTs arise from the confinement of the electrons in the circumferential direction, which allows electron motion only along the tube axis. If the two contact resistances exceed the resistance quantum, a nanotube quantum dot is formed. Charge quantization or energy quantization

can then be observed at low temperatures (Chapter 3).

A carbon peapod structure is fabricated by encapsulating Dy@C$_{82}$ molecules in SWNTs. The metallofullerenes are nested inside a nanotube one by one, forming a one-dimensional chain. The packing of metallofullerenes crucially depends on the inner diameter of the host nanotubes. Devices consisting of fully or partially encapsulated Dy@C$_{82}$ metallofullerenes in individual nanotubes have been performed. The charge transport through such a sophisticated structure has been investigated for the first time. The fullerene molecules are found to act as donors but surprisingly transfer electrons to nanotubes by lowering the temperature. The transport results reveal that the electronic structure of the nanotube is modified by encapsulated fullerene molecules. In partially filled nanotubes, an intrajunction is formed at the filled/unfilled interface and charge transport is dominated at this interface (Chapter 4). A more convincing experiment in the future will be the combination of transport with electron microscopes. We are fabricating individual suspending peapods, capable of being imaged by HRTEM after performing transport measurements. Another interesting aspect of the nanotube peapods is their magnetic properties. Investigation of the magnetotransport and the Kondo physics in one-dimensional magnetic peapods will be a new and intriguing field.

Chemical functionalization on carbon nanotubes presents a new opportunity for altering structural properties or for constructing desired structures. A good example is the formation of single wall carbon nanotube interjunctions used in probing the local electronic properties of side-connected nanotubes, in making conductive interconnection, or in creating new transistor functionalities. We demonstrate for the first time that the nanotube interjunctions can be stably formed by a single molecule linkage bridging two nanotubes (Chapter 5). The geometrical structure of these junctions is studied by AFM, the chemical reaction and functionalization induced changes in the electronic structure of nanotubes are monitored by XPS and Raman spectroscopy. More importantly, we show that this protocol presents a nondestructive, low-temperature method of introducing diamine linkage onto the SWNTs and consequently the formation of junction structures. A more controllable linkage reaction at specific point will be the next goal.

Quite soon after the discovery of the nanotubes several groups started to build transistors based on semiconducting nanotubes. The conventional way of preparing such transistors is to deposit the gold leads onto the oxide layer of silicon chips (by electron beam lithography), which serve as source and drain

contacts, to deposit carbon nanotubes over these leads, and to use the doped silicon substrate as a gate contact. By applying a voltage between the silicon gate and a nanotube the conductivity of the nanotube can be modulated by up to 5 orders of magnitude. The on-off ratio of these transistors is very large, but the gain is very small, because of the large distance between the gate and the nanotube (thickness of the oxide layer up to 1 μm). Recently, the group of Cees Dekker in Delft prepared carbon nanotube transistors with a gain of about 10. In this case the gate was a lithographic aluminum strip, the dielectric was an aluminum oxide layer, and the nanotube was placed on the top of this oxidized Al strip. Although these devices are based on carbon nanotubes the structure is not really nanoscale and is determined by lithographic leads. This has prompted us to prepare carbon nanotube transistors, which are really nanosized, and where both the conducting channel and the gate are made of nanotubes.

Following the chemical functionalization procedures, we have fabricated nanotube T-junctions by wet chemical methods and adsorbed these T-junctions on silicon chips, and afterwards painted metal leads by electron beam lithography. The end-connected nanotube serves as a local in-plane gate in addition to the back gate. The analysis shows that gain values of above 100 can be obtained. In addition to all-carbon transistors, we have also explored the modulation mechanisms in metallic nanotubes by using this sophisticated junction structures. We find that the behavior of this transistor cannot be fully explained in terms of conventional field-effect transistors, but that electromechanical effects also have to be taken into account. Applying a gate voltage not only changes the potential at the active channel, it also leads to deformation of the nanotube and changes the electronic structure. This is evident from the gap opening in metallic nanotubes under low carbon gate voltages (Chapter 6).

Appendix A

Band structure of carbon nanotube under deformation

For a structurally perfect nanotube, the Brillouin zone is hexagonal with $\mathbf{k}_F$ locating at the vertices $\mathbf{k}_v$. The electronic structure is determined by the boundary condition discussed in chapter 1. The allowed electronic states lie on parallel lines with spacing $2/d_t$. Upon applying uniaxial or torsional strains, real space vectors become $\mathrm{r} = (\mathrm{I} + \varepsilon)\mathrm{r}_0$, where $\mathrm{I} = (\delta_{ij})_{2\times2}$, $\varepsilon = (\varepsilon_{ij})_{2\times2}$ is a uniform 2D strain tensor applied to a graphite sheet, and the subscript denotes the original state. It can be transferred to $\mathbf{k}$ space as $\mathbf{k} = (\mathrm{I} + \varepsilon)^T \mathbf{k_0}$. Neglecting the trigonal warping effect around the $\mathbf{k}_v$ points (see Figure 1.7 in chapter 1), we can characterize the allowed electronic states in the deformed nanotube by considering only the change in $\mathbf{k}_F$ relative to invariant $\mathbf{k}$ lines $|\mathbf{k} - \mathbf{k}_F|$ with $\mathbf{k}_F = \mathbf{k}_v + \Delta\mathbf{k}_F$. $\mathbf{k}_F$ is determined by solving the Hückel tight-binding Hamiltonian:

$$E(\mathbf{k}_F) = \mid H(\mathbf{k}_F) \mid = \mid \sum t_j exp(i\mathbf{k} \cdot r_{j0}) \mid = 0 \qquad (7.1)$$

where $t_j = t_0 (r_0/r_j)^2$ is the Harrison hopping parameter [63].

We can obtain the $\Delta\mathbf{k}_F$ [161]:

$$\Delta k_F^c r_0 = (1+\nu)\sigma_t \cos3\theta + \gamma\sin3\theta \qquad (7.2)$$

$$\Delta k_F^t r_0 = (1+\nu)\sigma_t \sin3\theta + \gamma\cos3\theta \qquad (7.3)$$

where superscript t and c denote components along the tube axis and circumference, σ_t and γ are strains along t and c, corresponding to uniaxial and torsional strains on nanotubes, ν is the Poisson's ratio, and θ is the tube chiral angle.

Following the approach of Ref. [160, 161] and applying the boundary condition $\mathbf{k} \cdot \mathbf{C} = 2\pi\ell$ to the tube circumference, we can obtain the van Hove singularity.

$$\mid E_\ell \mid = \frac{3}{2} t_0 r_0 \Delta k_\ell^c \qquad (7.4)$$

$$\Delta k_\ell^c = \mid \frac{2}{3d_t}[3\ell - (3p + q)] - \Delta k_F^c \mid \qquad (7.5)$$

where d_t is the tube diameter, p and q are defined from the tube index (n, m) as $n - m = 3p + q$ with $q = 0$ (metallic) and ± 1 (semiconducting). Δk_ℓ^c measures the shortest distance between $\mathbf{k}_F$ and $\mathbf{k}$ lines of quantum number ℓ and determines the position of van Hove singularities which equal half of the energy gap. At zero strain, $\mathbf{k}_F$ sits at $\mathbf{k}_v$. Setting $\mathbf{k}_v$ as the origin, the nearest allowed $\mathbf{k}$ are at $2/3d_t$, 0, and $-2/3d_t$ on the c axis for tubes $q = -1$, 0, and 1, respectively. Therefore, for semiconducting tubes ($q = \pm 1$), the nearest van Hove singularity is at $\mid E_\ell \mid$ $= t_0 r_0 / d_t$ with a band gap of $2\mid E_\ell \mid$, and the second nearest one is at $\ell = p \pm 1$. For metallic tubes $q = 0$, the first nearest distance and the band gap are zero at $\ell = p$, and the second nearest distance is $\mathbf{k}$ line spacing of $\Delta k_{p\pm 1}^c = 2/d_t$, leading to the first van Hove singularity at $\mid E_{p\pm 1} \mid = 3t_0 r_0 / d_t$.

When strain drives $\mathbf{k}_F$ to shift away from $\mathbf{k}_v$ by $\Delta \mathbf{k}_F$, the positions of van Hove singularities and band gap change accordingly. The band gap can be enlarged or shrunk, depending on the shift of $\Delta \mathbf{k}_F$. The nearest distance Δk_p^c and band gap decrease for $q = -1$ but increase for $q = 1$. For metallic tube $q = 0$, an energy gap is induced. The changes of the band gap under strain can be derived from equation 7.2, 7.3, 7.4, and 7.5:

$$\Delta E_g = \mathrm{sgn}(2q + 1)3t_0[(1 + \nu)\sigma\cos 3\theta + \gamma_t \sin 3\theta] \qquad (7.6)$$

From this result, it is clearly seen that the electronic structure of armchair nanotubes ($\theta = \pi/6$) is very insensitive to the uniaxial strain but not to the torsional strain. In contrast, the electronic structure of zigzag nanotubes ($\theta = 0$) is inert to torsion, but sensitive to uniaxial strain. Other nanotubes fall in between.

Bibliography

[1] Averin, D. V. and Likharev, K. K. Coulomb blockade of single-electron tunneling, and coherent oscillations in small tunnel-junctions. *J. low temperature Phys.* **62**, 345-373 (1986).

[2] Alvarez, L. *et al.* Resonant Raman study of the structure and electronic properties of single-wall carbon nanotubes. *Chem. Phys. Lett.* **316**, 186-190 (2000).

[3] Anantram, M. P. Current-carrying capacity of carbon nanotubes. *Phys. Rev. B* **62**, R4837-R4840 (2000).

[4] Ando, T., Matsumura, H. and Nakanishi, T. Theory of ballistic transport in carbon nanotubes. *Physica B* **323**, 44-50 (2002).

[5] Antonov, R. D. and Johnson, A. T. Subband population in a single-wall carbon nanotube diode. *Phys. Rev. Lett.* **83**, 3274-3276 (1999).

[6] Avouris, Ph. Carbon nanotube electronics. *Chem. Phys.* **281**, 429-445 (2002).

[7] Avouris, Ph. Molecular electronics with carbon nanotubes. *Acc. Chem. Res.* **35**, 1026-1034 (2002).

[8] Bachtold, A. *et al.* Scanned probe microscopy of electronic transport in carbon nanotubes. *Phys. Rev. Lett.* **84**, 6082-6085 (2000).

[9] Bachtold, A., Hadley, P., Nakanishi, T. and Dekker, C. Logic circuits with carbon nanotube transistors. *Science* **294**, 1317-1320 (2001).

[10] Bahr, J. L. *et al.* Functionalization of carbon nanotubes by electrochemical reduction of aryl diazonium salts: A bucky paper electrode. *J. Am. Chem. Soc.* **123**, 6536-6542 (2001).

[11] Balavine, F. *et al.* Helical crystallization of proteins on carbon nanotubes: A first step towards the development of new biosensors. *Angew. Chem., Int. Ed.* **38**, 1912-1915 (1999).

[12] Bandow, S. *et al.* Effect of the growth temperature on the diameter distribution and chirality of single-wall carbon nanotubes. *Phys. Rev. Lett.* **80**, 3779-3782 (1998).

[13] Barnes, J. B. and Ruggiero, S. T. Observation of the incremental charging of Ag particles by single electrons. *Phys. Rev. Lett.* **59**, 807-810 (1987).

[14] Barwich, V. *et al.* Carbon nanotubes as tips in non-contact SFM. *Appl. Surf. Sci.* **157**, 269-273 (2000).

[15] Baughman, R. H. *et al.* Carbon nanotube actuators. *Science* **284**, 1340-1344 (1999).

[16] Baughman, R. H., Zakhidov, A. A. and de Heer, W. A. Carbon nanotubes-the route toward applications. *Science* **297**, 787-792 (2002).

[17] Bendiab, N. *et al.* Combined in situ conductivity and Raman studies of rubidium doping of single-wall carbon nanotubes. *Phys. Rev. B* **63**, 153407-153410 (2001).

[18] Bezryadin, A., Verschueren, A. M. R., Tans, S. J. and Dekker C. Multi-probe transport experiments on individual single-wall carbon nanotubes. *Phys. Rev. Lett.* **80**, 4036-4039 (1998).

[19] Bockrath, M. *et al.* Single-electron transport in ropes of carbon nanotubes. *Science* **275**, 1922-1925 (1997).

[20] Boul, P. J. *et al.* Reversible sidewall functionalization of buckytubes. *Chem. Phys Lett.* **310**, 367-372 (1999).

[21] Brandt, N. B., Chudinov, S. M. and Ponomarev, Ya. G. Semimetals, 1. Graphite and its Compounds. (North-Holland, Amsterdam, 1988).

[22] Brown, S. D. M. *et al.* Anti-stokes raman spectra of single-walled carbon nanotubes. *Phys. Rev. B* **61**, R5137-R5140 (2000).

[23] Brown, S. D. M., Jorio, A., Dresselhaus, M. S. and Dresselhaus, G. Observations of the D-band feature in the Raman spectra of carbon nanotubes. *Phys. Rev. B* **64**, 073403 (2001).

[24] Burghard, M., Duesberg, G., Philipp, G., Muster, J. and Roth, S. Controlled adsorption of carbon nanotubes on chemically modified electrode arrays. *Adv. Mater.* **10**, 584-588 (1998).

[25] Burroughes, J. H., Jones, C. A. and Friend, R. H. New semiconductor device physics in ploymer diodes and transistors. *Nature* **335**, 137-141 (1988).

[26] Cao, J., Wang, Q. and Dai, H. Electromechanical properties of metallic, quasimetallic, and semiconducting carbon nanotubes under stretching. *Phys. Rev. Lett.* **90**, 157601 (2003).

[27] Chen, J. *et al.* Solution properties of single-walled carbon nanotubes. *Science* **282**, 95-98 (1998).

[28] Chen, Y. *et al.* Chemical attachment of organic functional groups to single-walled carbon nanotube material. *J. Mater. Res.* **13**, 2423-2431 (1998).

[29] Chen, R. J., Zhan, Y. G., Wang, D. W. and Dai, H. J. Noncovalent sidewall functionalization of single-walled carbon nanotubes for protein immobilization. *J. Am. Chem. Soc.* **123**, 3838-3839 (2001).

[30] Chiang, I. W., Brinson, B. E., Smalley, R. E., Margrave, J. L. and Hauge R. H. Purification and characterization of single-wall carbon nanotubes. *J. Phys. Chem. B* **105**, 1157-1161 (2001).

[31] Chiu, P. W. *et al.* Temperature-induced change from p to n conduction in metallofullerene nanotube peapods. *Appl. Phys. Lett.* **79**, 3845-3847 (2001).

[32] Chiu, P. W., Guesberg, G. S., Dettlaff-Weglikowska and Roth, S. Interconnection of carbon nanotubes by chemical functionalization. *Appl. Phys. Lett.* **80**, 3811-3813 (2002).

[33] Chiu, P. W., Yang, S. F., Yang, S. H., Gu, G. and Roth, S. Temperature Dependence of Conductance Character in Nanotube Peapods. *Appl. Phys. A* **76**, 463-467 (2003).

[34] Claye, A. *et al.* In situ Raman scattering studies of alkali-doped single wall carbon nanotubes. *Chem. Phys. Lett.* **333**, 16-22 (2001).

[35] Collins, P. G., Bradley, K., Ishigami, M. and Zettl, A. Extreme oxygen sensitivity of electronic properties of carbon nanotubes. *Science* **287**, 1801-1804 (2000).

[36] Dai, H. J., Hafner, J. H., Rinzler, A. G., Colbert, D. T. and Smalley, R. E. Nanotubes as nanoprobes in scanning probe microscopy. *Nature* **384**, 147-150 (1996).

[37] Dekker, C. Carbon nanotubes as molecular quantum wires. *phys. today* **52**, 22-28 (1999).

[38] Derycke, V., Martel, R., Appenzeller, J. and Avouris, Ph. Carbon nanotube inter- and intramolecular logic gates. *Nano Letters* **1**, 453-456 (2001).

[39] Dimitrakopoulos, C. D., Brown, A. R. and Pomp, A. Molecular beam deposited thin films of pentacene for organic thin film transistor application. *J. Appl. phys.* **80**, 2501-2508 (1996).

[40] Dimitrakopoulos, C. D. and Mascaro, D. J. Organic thin-film transistors: A review of recent advances. *IBM J. Res. & Dev.* **45**, 11-27 (2001).

[41] Dresselhaus, M. S. and Eklund, P. C. Phonons in carbon nanotubes. *Adv. Phys.* **49**, 705-814 (2000).

[42] Dresselhaus, M. S., Dresselhaus, G. and Avouris, Ph. Carbon nanotubes: Synthesis, Structure Properties and Applications. (Springer-Verlag, Berlin, 2001).

[43] Fagan, S. B. *et al.* Functionalization of carbon nanotubes through the chemical binding of atoms and molecules. *Phys. Rev. B* **67**, 033405 (2003).

[44] Fagas, G., Cuniberti, G. and Richter, K. Electron transport in nanotube-molecular-wire hybrids. *Phys. Rev. B* **63**, 045416 (2001).

[45] Falvo, M. R. Bending and buckling of carbon nanotubes under large strain. *Nature* **389**, 582-584 (1997).

[46] Farajian, A. A. and Mikami, M. Electronic and mechanical properties of C_{60}-doped nanotubes. *J. Phys. - Condens Mat.* **13**, 8049-8059 (2001).

[47] Frank, S., Poncharal, P., Wang, Z. L. and de Heer, W. A. Carbon nanotube quantum resistors. *Science* **280**, 1744-1746 (1998).

[48] Freitag, M., Radosavljevic, M., Clauss, W. and Johnson, A. T. Local electronic properties of single-wall nanotube circuits measured by conducting-tip AFM. *Phys. Rev. B* **62**, R2307-R2310 (2000).

[49] Gartstein, Y. N., Zakhidov, A. A. and Baughman, R. H. Charge-induced anisotropic distortions of semiconducting and metallic carbon nanotubes. *Phys. Rev. Lett* **89**, 45503 (2002).

[50] Gerogakilas, V. *et al.* Purification of HiPCO carbon nanotubes via organic functionalization. *J. Am. Chem. Soc.* **124**, 14318-14319 (2002).

[51] Gorter, I. and Zeller, H. R. Superconductivity of small tin particles measured by tunneling. *Phys. Rev. Lett.* **20**, 1504-1507 (1968).

[52] Grabert, H. and Devoret, M. H. Single Charge Tunneling. (Plenum, New York 1991).

[53] Grigorian, L. *et al.* Transport properties of alkali-metal-doped single-wall carbon nanotubes. *Phys. Rev. B* **58**, R4195-R4198 (1998).

[54] Gu, G. *et al.* V_2O_5 nanofibre sheet actuators. *Nature Materials* **2**, 316-319 (2003).

[55] Guo, Y. and Guo, W. Mechanical and electrostatic properties of carbon nanotubes under tensile loading and electric field. *J. Phys. D* **36**, 805-811 (2003).

[56] Guo, W. and Guo, Y. Giant axial electrostrictive deformation in carbon nanotubes. *Phys. Rev. Lett.* **91**, 115501 (2003).

[57] Gutierrez, R. *et al.* Theory of an all-carbon molecular switch. *Phys. Rev. B* **65**, 113410 (2002).

[58] Haddon, R. C. Chemistry of the fullerenes: The manifestation of strain in a class of continuous aromatic molecules. *Science* **261**, 1545-1550 (1993).

[59] Haddon, R. C. *et al.* C_{60} thin film transistors. *Appl. Phys. Lett.* **67**, 121-123 (1995).

[60] Hafner, J. H., Cheung, C. L. and Lieber, C. M. Growth of nanotubes for probe microscopy tips. *Nature* **398**, 761-762 (1999).

[61] Hamon, M. A. *et al.* End-group and defect analysis of soluble single-walled carbon nanotubes. *Chem. Phys. Lett.* **347**, 8-12 (2001).

[62] Han, S. and Ihm, J. Role of the localized states in field emission of carbon nanotubes. *Phys. Rev. B* **61**, 9986-9989 (2000).

[63] Harrison, W. A. Electronic structure and the properties of solids: The physics of the chemical bond. (Freeman, San Francisco, 1990).

[64] Hassanien, A. *et al.* Atomic structure and electronic properties of single-wall carbon nanotubes probed by scanning tunneling microscope at room temperature. *Appl. Phys. Lett.* **73**, 3839-3841 (1998).

[65] de Heer, W. A., Châtelain, A. and Ugarte, D. A carbon nanotube field-emission electron source. *Science* **270**, 1179-1180 (1995).

[66] Heinze, S. *et al.* Carbon nanotubes as Schottky barrier transistors. *Phys. Rev. Lett.* **89**, 106801 (2002).

[67] Heyd, R., Charlier, A. and McRae E. Uniaxial-stress effects on the electronic properties of carbon nanotubes. *Phys. Rev. B* **55**, 68206824 (1997).

[68] Hirahara, K. *et al.* One-dimensional metallofullerene crystal generated inside single-walled carbon nanotubes. *Phys. Rev. Lett.* **85**, 5384-5387 (2000).

[69] Hirsch, A. Functionalization of single-walled carbon nanotubes. *Angew. Chem. Int. Ed.* **41**, 1853-1859 (1999).

[70] Hodak, M. and Girifalco, L. A. Ordered phases of fullerene molecules formed inside carbon nanotubes. *Phys. Rev. B* **67**, 075419 (2003).

[71] Hornbaker, D. J. *et al.* Mapping the one-dimensional electronic states of nanotube peapod structures. *Science* **295**, 828-831 (2002).

[72] Huang, H. J., Yang, S. H. and Zhang, X. X. Magnetic properties of heavy rare-earth metallofullerenes $M@C_{82}$ (M = Gd, Tb, Dy, Ho, and Er). *J. Phys Chem. B* **104**, 1473-1482 (2000).

[73] Iijima, S. Helical microtubules of graphite carbon. *Nature* **354**, 56-58 (1991).

[74] Image gallery of R. E. Smalley: http://cnst.rice.edu/pics.html

[75] Javey, A. *et al.* High κ dielectrics for advanced carbon-nanotube transistors and logic gates. *Nature Materials* **1**, 241-246 (2002).

[76] Javey, A., Wang, Q., Ural, A., Li, Y. M. and Dai, H. J. Carbon nanotube transistor arrays for multistage complementary logic and ring oscillators. *Nano Letters* **2**, 929-932 (2002).

[77] Javey, A., Shim, M. and Dai, H. J. Electrical properties and devices of large-diameter single-walled carbon nanotubes. *Appl. Phys. Lett.* **80**, 1064-1066 (2002).

[78] Jiang, J., Dong, J. and Xing, D. Y. Quantum interference in carbon-nanotube electron resonators. *Phys. Rev. Lett.* **91**, 56802 (2003).

[79] Jishi, R. A. Venkataraman, L., Dresselhaus, M. S. and Dresselhaus, G. Phonon modes in carbon nanotubules. *Chem. Phys. Lett.* **209**, 77-82 (1993).

[80] Kane, C. L. and Mele, E. J. Size, shape, and low energy electronic structure of carbon nanotubes. *Phys. Rev. Lett.* **78**, 19321935 (1997).

[81] Kazaoui, S., Minami, N., Jacquemin, R., Kataura, H. and Achiba, Y. Amphoteric doping of single-wall carbon-nanotube thin films as probed by optical absorption spectroscopy. *Phys. Rev. B* **60**, 13339-13342 (1999).

[82] Keblinski, P., Nayak, S. K., Zapol, P. and Ajayan P. M. Charge distribution and stability of charged carbon nanotubes. *Phys. Rev. Lett.* **89**, 255503 (2002).

[83] Kim, P. and Lieber, C. M. Nanotube nanotweezers. *Science* **286**, 2148-2150 (1999).

[84] Kim, Y. -H. and Chang, K. J. Subband mixing rules in circumferentially perturbed carbon nanotubes: Effects of transverse electric fields. *Phys. Rev. B* **64**, 153404 (2001).

[85] Klein, E. L. *et al.* An approach to electrical studies of single nanocrystals. *Appl. Phys. Lett.* **68**, 2574-2576 (1996).

[86] Kong, L. and Chou, S. Y. Quantification of magnetic force microscopy using a micronscale current ring. *Appl. Phys. Lett.* **70**, 2043-2045 (1997).

[87] Kong, J., Zhou, C., Yenilmez, E. and Dai, H. Alkaline metal-doped n-type semiconducting nanotubes as quantum dots. *Appl. Phys. Lett.* **77**, 3977- (2000).

[88] Kong, J. *et al.* Quantum interference and ballistic transmission in nanotube waveguides. *Phys. Rev. Lett.* **87**, 106801 (2001).

[89] Kroto, H. W., Heath, J. R., O'Brien, S. C., Curl, R. F. and Smalley, R. E. C_{60}: Buckminsterfullerene. *Nature* **318**, 162- (1985).

[90] Krüger, M. PhD Thesis in university of Basel.

[91] Kukovecz, A. *et al.* On the stacking behavior of functionalized single-wall carbon nanotubes. *J. Phsy. Chem. B* **106**, 6374-6380 (2002).

[92] Kürti, J., Kresse, G. and Kuzmany, H. First-principles calculations of the radial breathing mode of single-wall carbon nanotubes. *Phsy. Rev. B* **58**, R8869-R8872 (1998).

[93] Lammert, P. E., Zhang, P. and Crespi, V. H. Gapping by squashing: metal-insulator and insulator-metal transitions in collapsed carbon nanotubes. *Phys. Rev. Lett.* **84**, 2453-2456 (2000).

[94] Lau, K. T. and Hui, D. Effectiveness of using carbon nanotubes as nano-reinforcements for advanced composite structures. *Carbon* **40**, 1605-1606 (2002).

[95] Lee, J. *et al.* Bandgap modulation of carbon nanotubes by encapsulated metallofullerenes. *Nature* **415**, 1005-1008 (2002).

[96] Liang, W. *et al.* Fabry - Perot interference in a nanotube electron waveguide. *Nature* **411**, 665-669 (2001).

[97] Lin, Y. Y., Gundlach, D. J., Nelson, S. and Jackson, T. N. Stacked pentacene layer organic thin-film transistors with improved characteristics. *IEEE Electron Device Lett.* **18**, 606-608 (1997).

[98] Liu, J. *et al.* Fullerene Pipes. *Science* **280**, 1253-1256 (1998).

[99] Liu, X., Lee, C. and Zhou, C. Carbon nanotube field-effect inverters. *Appl. Phys. Lett.* **79**, 3329-3331 (2001).

[100] Lu, J. -Q. *et al.* Metal-to-semiconductor transition in squashed armchair carbon nanotubes. *Phys. Rev. Lett.* **90**, 156601 (2003).

[101] Martel, R., Schmidt, T., Shea, H. R., Hertel, T. and Avouris, Ph. Single- and multi-wall carbon nanotube field-effect transistors. *Appl. Phys. Lett.* **73**, 2447-2449 (1998).

[102] Martel, R. *et al.* Ambipolar electrical transport in semiconducting single-wall carbon nanotubes. *Phys. Rev. Lett.* **87**, 256805 (2001).

[103] Mawhinney, D. B. *et al.* Surface defect site density on single walled carbon nanotubes by titration. *Chem. Phys. Lett.* **324**, 213-216 (2000).

[104] Mayer, J. W. and Lau, S. S. Electronic materials science: For integrated circuits in Si and GaAs. (Macmillan, New York, 1990).

[105] McEuen, P. L., Bockrath, M., Cobden, D. H., Yoon, Y. G. and Louie S. G. Disorder, Pseudospins, and Backscattering in Carbon Nanotubes. *Phys. Rev. Lett.* **83**, 5098-5101 (1999).

[106] McEuen, P. L. Single-wall carbon nanotubes. *Phys. World* **13**, 31-36 (2000).

[107] Menon, M. and Srivastava, D. Carbon nanotube "T Junctions": nanoscale metal-semiconductor-metal contact devices. *Phys. Rev. Lett.* **79**, 44534456 (1997).

[108] Menon, M., Andriotis, A. N., Srivastava, D., Ponomareva, I. and Srivastava, D. Carbon nanotube "T Junctions": formation pathways and conductivity. *Phys. Rev. Lett.* **91**, 145501 (2003).

[109] Mickelson, E. T. *et al.* Fluorination of single-wall carbon nanotubes. *Chem. Phys. Lett.* **296**, 188-194 (1998).

[110] Minot, E. D. *et al.* Tuning carbon nanotube band gaps with strain. *Phys. Rev. Lett.* **90**, 156401 (2003).

[111] Müller-pherffer, S., Schneider, M. and Zinn, W. Imaging of magnetic domain walls in iron with magnetic force microscope: A nemerical study. *Phys. Rev. B* **49**, 15745-15752 (1994).

[112] Niyogi, S. *et al.* Chemistry of single-walled carbon nanotubes. *Acc. Chem. Res.* **35**, 1105-1113 (2002).

[113] Odom, T. W., Huang, J. -L., Kim, P. and Lieber, C. M. Atomic structure and electronic properties of single-walled carbon nanotubes. *Nature* **391**, 62-64 (1998).

[114] Odom, T. W., Huang, J. -L., Kim, P. and Lieber, C. M. Structure and electronic properties of carbon nanotubes. *J. Phsy. Chem. B* **104**, 2794-2809 (2000).

[115] Okada, S., Saito, S. and Oshiyama, A. Energetics and electronic structures of encapsulated C_{60} in a carbon nanotube. *Phys. Rev. Lett.* **86**, 3835-3838 (2001).

[116] Ouyang, M., Huang, J. -L., Cheung, C. L. and Lieber, C. M. Energy gaps in "Metallic" single-walled carbon nanotubes. *Science* **292**, 702-705 (2001).

[117] Poirier, D. M. *et al.* Electronic and geometric structure of $La@xaC_{82}$ and C_{82}: Theory and experiment. *Phys. Rev. B* **49**, 17403-17412 (1994).

[118] Poncharal, P., Wang, Z. L., Ugarte, D. and de Heer, W. A. Electrostatic deflections and electromechanical resonances of carbon nanotubes. *Science* **283**, 1513-1516 (1999).

[119] Porksch, R. *et al.* Quantitative magnetic field measurements with the magnetic force microscope. *Appl. Phys. Lett.* **69**, 2599-2601 (1996).

[120] Postma, H. W. C., Teepen, T., Yao, Z., Grifoni, M. and Dekker, C. Carbon nanotube single-electron transistors at room temperature. *Science* **293**, 76-79 (2001).

[121] Rols, S. *et al.* Diameter distribution of single wall carbon nanotubes in nanobundles. *Eur. Phys. J B* **18**, 201-205 (2000).

[122] Rao, A. M. *et al.* Diameter-selective Raman scattering from vibrational modes in carbon nanotubes. *Science* **275**, 187-191 (1997).

[123] Rao, A. M., Eklund, P. C., Bandow, S., Thess, A. and Smalley, R. E. Evidence for charge transfer in doped carbon nanotube bundles from Raman scattering. *Nature* **388**, 257-259 (1997).

[124] Rao, A. M., Bandow, S., Richter, E. and Eklund, P. C. Raman spectroscopy of pristine and doped single wall carbon nanotubes. *Thin Solid Films* **331**, 141-147 (1998).

[125] Reed, M. A., Zhou, C., Muller, C. J., Burgin, T. P. and Tour, J. M. Conductance of a molecular junction. *Science* **278**, 252-254 (1997).

[126] Rhoderick, E. H. Metal-semiconductor contacts. (Clarendon, Oxford, 1978).

[127] Riordan, M., Hoddeson, L. and Herring, C., The invention of the transistor. *Rev. Mod. Phys.* **71**, S336-S345 (1999).

[128] Rocheford, A., Avouris, Ph., Lesage, F. and Salahub, D. R. Electrical and mechanical properties of distorted carbon nanotubes. *Phys. Rev. B* **60**, 1382413830 (1999).

[129] Rocheford, A. Electronic and transport properties of carbon nanotube peapods. *Phys. Rev. B* **67**, 15401-115407 (2003).

[130] Ruzin, I. M., Chandrasekhar, V., Levin, E. I. and Glazman, L. I. Stochastic coulomb blockade in a double-dot system. *Phys. Rev. B* **45**, 13469-13478 (1992).

[131] Saito, R., Fujita, M., Dresselhaus, G. and Dresselhaus, M. S. Electronic structure of graphene tubules based on C_{60}. *Phsy. Rev. B* **46**, 1804-1811 (1992).

[132] Saito, R., Takeya, T., Kimura, T., Dresselhaus, G. and Dresselhaus, M. S. Raman intensity of single-wall carbon nanotubes. *Phsy. Rev. B* **57**, 4145-4153 (1998).

[133] Saito, R., Dresselhaus, G. and Dresselhaus, M. S. Trigonal warping effect of carbon nanotubes. *Phsy. Rev. B* **61**, 2981-2990 (2000).

[134] Salvetat, J. -P. *et al.* Elastic and shear moduli of single-walled carbon nanotube ropes. *Phsy. Rev. Lett.* **82**, 944-947 (1999).

[135] Samsonidze, G. G. *et al.* Phonon Trigonal Warping Effect in Graphite and Carbon Nanotubes. *Phsy. Rev. Lett.* **90**, 904031-904034 (2003).

[136] Sano, M., Kamino, A., Okamura, J. and Shinkai, S. Ring closure of carbon nanotubes. *Science* **293**, 1299-1301 (2001).

[137] Sharma, B. L. and Purohit, R. K. Semiconductor Heterojunctions. (Pergamon, Oxford, 1974).

[138] Shinohara, H. Endohedral metallofullerenes. *Rep. Prog. Phys.* **63**, 843-892 (2000).

[139] Smith, B. W., Monthioux, M. and Luzzi, D. E. Encapsulated C60 in carbon nanotubes. *Nature* **396**, 323-324 (1998).

[140] Smith, B. W., Monthioux, M. and Luzzi, D. E. Carbon nanotube encapsulated fullerenes: a unique class of hybrid materials. *Chem. Phys. Lett.* **315**, 31-36 (1999).

[141] Srivastava, D. *et al.* Predictions of enhanced chemical reactivity to regions of local conformational strain on carbon nanotubes: kinky chemistry. *J. Phys. Chem. B* **103**, 4330-4337 (1999).

[142] Stowe, T. D. *et al.* Attonewton force detection using ultrathin silicon cantilevers. *Appl. Phys. Lett.* **71**, 288-290 (1997).

[143] Suenaga, K. *et al.* Element-Selective Single Atom Imaging. *Science* **290**, 2280-2282 (2000).

[144] Suenaga, K. *et al.* Direct imaging of $Sc_2@C_{84}$ molecules encapsulated inside single-wall carbon nanotubes by high resolution electron microscopy with atomic sensitivity. *Phys. Rev. Lett.* **90**, 055506 (2003).

[145] Sumanasekera, G. U., Adu, C. K. W., Fang, S. and Eklund, P. C. Effects of gas adsorption and collisions on electrical transport in single-walled carbon nanotubes. *Phys. Rev. Lett.* **85**, 1096-1099 (2000).

[146] Sze, S. M. Physics of semiconductor devices. (John Wiley & Sons, New York, 1969).

[147] Tans, S. J. *et al.* Individual single-wall carbon nanotubes as quantum wires. *Nature* **386**, 474-477 (1997).

[148] Tans, S. J., Verschueren, A. R. M. and Dekker, C. Room-temperature transistor based on a single carbon nanotube. *Nature* **393**, 49-52 (1998).

[149] Tombler, T. W. *et al.* Reversible electromechanical characteristics of carbon nanotubes under local-probe manipulation. *Nature* **405**, 769-772 (2000).

[150] Venkateswaran, U. D. *et al.* Probing the single-wall carbon nanotube bundle: Raman scattering under high pressure. *Phsy. Rev. B* **59**, 10928-10934 (1999).

[151] Venkateswaran, U. D. *et al.* Pressure dependence of the Raman modes in iodine-doped single-walled carbon nanotube bundles. *Phsy. Rev. B* **65**, 054102 (2002).

[152] Weedon, B. R., Haddon, R. C., Spielmann, H. P. and Meier, M. S. Fulleroid addition regiochemistry is driven by pi-orbital misalignment. *J. Am. Chem. Soc.* **121**, 335-340 (1999).

[153] White, C. T., Robertson, D. H. and Mintmire, J. W. Helical and rotational symmetry of nanoscale graphitic tubules. *Phys. Rev. B* **47**, 5485-5488 (1993).

[154] White, C. T. and Mintmire, J. W. Density of states reflects diameter in nanotubes. *Nature* **394**, 29-30 (1998).

[155] Wildöer, J. W. G., Venema, L. C., Rinzler, A. G., Smalley, R. E. and Dekker, C. Electronic structure of atomically resolved carbon nanotubes. *Nature* **391**, 59-62 (1998).

[156] Wind, S. J., Appenzeller, J., Martel, R., Derycke, V. and Avouris, Ph. Vertical scaling of carbon nanotube field-effect transistors using top gate electrodes. *Appl. Phsy. Lett.* **80**, 3817-3819 (2002).

[157] Wong, S. S., Joselevich, E., Woolley, A. T., Cheung, C. L. and Lieber, C. M. Covalently functionalized nanotubes as nanometre- sized probes in chemistry and biology. *Nature* **394**, 52-55 (1998).

[158] Yao, Z., Kane, C. L., and Dekker, C. High-field electrical transport in single-wall carbon nanotubes. *Phsy. Rev. Lett.* **84**, 29412944 (2000).

[159] Yao, Z., Postma, H. W. Ch., Balents, L. and Dekker, C. Carbon nanotube intramolecular junctions. *Nature* **402**, 273276 (1999).

[160] Yang, L., Anantram, M. P., Han, J. and Lu, J. P. Band-gap change of carbon nanotubes: Effect of small uniaxial and torsional strain. *Phsy. Rev. B* **60**, 1387413878 (1999).

[161] Yang, L. and Han, J. Electronic structure of deformed carbon nanotubes. *Phsy. Rev. Lett.* **85**, 154-157 (2000).

[162] Zhang, Y. and Iijima, S. Elastic response of carbon nanotube bundles to visible light. *Phsy. Rev. Lett.* **82**, 34723475 (1999).

[163] Zhou, C., Kong, J. and Dai, H. Intrinsic electrical properties of individual single-walled carbon nanotubes with small band gaps. *Phsy. Rev. Lett.* **84**, 5604-5607 (2000).

[164] Zhou, C., Kong, J., Yenilmez, E. and Dai, H. Modulated chemical doping of individual carbon nanotubes. *Science* **290**, 1552-1555 (2000).

[165] Zhu, X., Grütter, P., Metlushko, V. and Ilic, B. Magnetic force microscopy study of electron-beam-patterned soft permalloy particles: Technique and magnetization behavior. *Phys. Rev. B* **66**, 024423 (2002).

Curriculum Vitae

26.06.1973   Born in Kaohsiung (Taiwan)

1992 - 1997   Undergraduate study in the department of materials science and engineering at Tsing Hua University (Taiwan)

1994 - 1995   German language courses at the Universität des Saarlandes (Germany)

1997 - 1998   Graduate study in the department of materials science and engineering at Tsing Hua University (Taiwan);
Master Thesis: Preparation of Palladium-Silver Alloy Membrane for Hydrogen Separation and Hydrogen Permeation Properties in the Membrane

1999 - 2003   „DAAD" awards by German Academic Exchange Service

1999 - 2000   PhD study in the department of physics at the Technical University Munich (Germany)

2000 - 2003   Switch PhD study to the group of „Prof. Klaus von Klitzing" at Max-Planck Institute for solid state research, Stuttgart (Germany)
PhD Thesis: Towards Carbon Nanotube-based Molecular Electronics

Publication list

Journal:

1. P. W. Chiu, G. Gu, G. T. Kim, G. Philipp, S. Roth, S. F. Yang, and S. Yang, "Temperature-induced Change from p to n Conduction in Metallofullerene Nanotube Peapods", Appl. Phys. Lett. **79**, 3845 (2001).

2. G. Gu, M. Burghard, G. T. Kim, G. S. Duesberg, **P. W. Chiu**, V. Krstic, S. Roth, and W. Han, "Growth and Electrical Transport of Germanium Nanowires", J. Appl. Phys. **90**, 5747 (2001).

3. P. W. Chiu, G. S. Guesberg, U. Dettlaff-Weglikowska, and S. Roth, "Interconnection of Single-walled Carbon Nanotubes by Chemical Functionalization", Appl. Phys. Lett. **80**, 3811 (2002).

4. U. Dettlaff-Weglikowska, J.-M. Benoit, **P. W. Chiu**, R. Graupner, S. Lebedkin, and S. Roth, "Chemical Functionalization of Single Walled Carbon Nanotubes", Current Appl. Phys. **2**, 497 (2002).

5. R. Czerw, **P. W. Chiu**, Y. M. Choi, D. S. Lee, D. L. Carroll, S. Roth, and Y. W. Park, "Substitutional Boron-doping of Carbon Nanotubes", Current Appl. Phys. **2**, 473 (2002).

6. P. W. Chiu, S. F. Yang, S. H. Yang, G. Gu, and S. Roth, "Temperature Dependence of Conductance Character in Nanotube Peapods", Appl. Phys. A **76**, 463 (2003).

7. G. Gu, M. Schmid, **P. W. Chiu**, A. Minett, J. Fraysse, G. T. Kim, S. Roth, M. Kozlov, E. Muňoz, and R. H. Baughman, "V_2O_5 Nanofibre Sheet Actuators", Nature Materials **2**, 316-319 (2003).

8. Y.-M. Choi, D.-S. Lee, R. Czerw, **P. W. Chiu** N. Grobert, M. Terrones, M. Reyes-Reyes, H. Terrones, J.-C. Charlier, P. M. Ajayan, S. Roth, D. L. Carroll, and Y.-W. Park, "Nonlinear Behavior in the Thermopower of Doped Carbon Nanotubes Due to Strong, Localized States", Nano Lett. **3**, 839-842 (2003).

9. P. W. Chiu, M. Kaempgen, and S. Roth, "Band Structure Modulation in Carbon Nanotube T-Junctions", Phys. Rev. Lett. (submitted).

10. P. W. Chiu, J. -M. Benoit, R. Graupner, U. Dettlaff, and S. Roth, "Carbon Nanotube T-Junctions: Formation and characteristics", Angew. Chem. Int. Ed. (in preparation).

Proceeding:

1. P. W. Chiu, G. T. Kim, G. Gu, G. Philipp, and S. Roth, "Electrical Transport through Carbon Nanotube Junction", Electronic Properties of Molecular Nanostructures, eds. H. Kuzmany, J. Fink, M, Mehring, S. Roth, AIP 591, New York 2001, p 368-371.

2. P. W. Chiu, G. S. Duesberg, U. Dettlaff-Weglikowska, and S. Roth, "Towards Carbon Nanotube In-plane Transistors", Structural and Electronic Properties of Molecular Nanostructures, eds. H. Kuzmany, J. Fink, M, Mehring, S. Roth, AIP 633, New York 2002, p 517-521.

3. P. W. Chiu, M. Kaemgen, U. Dettlaff, and S. Roth, "Formation and Transistor Behavior of Carbon Nanotube T-junctions", MRS Meeting Proceeding, San Francisco, April 21 - 25, 2003.

Invited talks:

1. "Electrical Transport in Carbon Nanotube in-plane Transistors", XVIth Internaotinal Winterschool on Electronic Properties of Novel Materials, Kirschberg, Austria, March 2 - 9, 2002.

2. "Electrical Transport in Metallofullerene Nanotube Peapods", 201st ECS (The Electrochemical Society) Centennial Meeting, Philadelphia Marriott, Pennsylvania, May 12 - 17, 2002.

3. "Formation and Characterization of Carbon Nanotube intermolecular Junctions", International Conference on Science and Technology of Synthetic metals, Shanghai, China, June 29 - July 5, 2002.

4. "All-Carbon Transistors", MRS (The Materials Research Society) Spring Meeting, San Francisco, April 21 - 25, 2003.

5. "Magnetic Force Microscopy of Carbon Nanotube Peapods", ECS (The Electrochemical Society) Spring Meeting, Paris, April 27 - May 2, 2003.

6. "All-carbon Transistors", E-MRS (The European Materials Research Society) Spring Meeting, Strasbourg, France, June 10 - June 13, 2003.

Acknowledgements